Air Film Dampers and Their Optimisation

By:

Boyang GAO

A thesis submitted in partial fulfilment of the requirements for the degree of

Doctor of Philosophy

University of Sheffield

Department of Mechanical Engineering

Supervisors:

Dr. Jem RONGONG & Prof. Kirill HOROSHENKOV

February, 2019

Declaration of Authorship

I hereby declare that except where specific reference is made to the work of others, the contents of this thesis are original and have not been submitted in whole or in part for consideration for any other degree or qualification in this, or any other university. This thesis is my own work and contains nothing which is the outcome of work done in collaboration with others, except as specified in the text and Acknowledgements.

Boyang Gao
February 2019

To my parents and wife:

Appreciate for all financial support from my parents, and for all love from you.

I can not have done this without you.

.

Abstract

Vibration control is an important consideration in the design of weight-critical machinery and components operating at high speed in harsh environments. Increasing damping levels is often the easiest way to reduce the vibration of the system without sacrificing performance. The air film damper is interesting because its damping performance cannot be significantly influenced by ambient temperature. However, it is difficult to develop an air film damper with satisfactory performance, because the damping efficiency of the air gap is very sensitive to some factors, such as the gap thickness, the air viscosity and the ambient pressure. For all but the simplest of geometries, the effects of such factors are not easy to identify using analytical methods. This makes the task of designing an air film damper challenging, particularly in practical applications where other factors such as manufacturability must be accounted for.

The rapid development of computer technology now presents an opportunity to solve much more complex tasks and consequently, the design of components is now frequently supported by appropriate finite element (FE) analysis. This thesis, therefore, sets out to use the structural-acoustic coupling routines, now available in commercial finite element software, to improve the practical understanding of the air film damper and to demonstrate a design methodology for their optimisation. For this purpose, an FE model is developed to deal with more complex geometries of the plate/air gap system.

Numerical methods are used to predict the damping ratio of a vibrating plate separated from a solid wall by a narrow air gap. Validation of the numerical approach is achieved by comparison with physical experiments and an existing theoretical model for a range of air gap thicknesses and air pressures. The numerical approach is then used to investigate air gap designs that have previously not been considered because of their complex geometry. These studies show that by partially restricting the ability of the air to flow, through the use of channels, the requirement for a very narrow gap can be relaxed. For practical designs, this is important as manufacturing large, thin gaps are very expensive. The limiting factor in the length of such channels is shown to be the compressibility of the air as particularly high restriction to flow can result in local pressure changes.

List of Figures

List of Tables

Contents

Nomenclature

A	Surface area of fluid-solid interface in the pore	m^2
C_p	Specific heat at constant pressure	J/K
C_v	Specific heat at constant volume	J/K
$I(\omega)$	Inertance function	
L_b	Length of baffle in baffle geometries	
N_b	Number of baffles in baffle geometries	
P_0	Pressure	Pa
V	Homogenization volume of fluid in the porous material or air slit	
$Y(\omega)$	Mobility function	
$\overline{h}(t)$	Distance between top to bottom plate	
$\widetilde{K}$	Dynamic bulk modulus	
h	Amplitude of oscillation for the top plate	m
h_0	Half thickness of the air film	m
k_0	Constant for pore shapes	

k_x	Normalised wave number vector components along x-axis	
k_y	Normalised wave number vector components along y-axis	
$n(s\sigma)$	Polytropic constant	
r_h	Hydraulic radius for circular pores	
t	Time	s
u_1, u_2	Velocities in the x-direction of the top plate and the bottom plate	
v	Velocity of particle within porous material or air slit	
v_1, v_2	Velocities in the y-direction of the top plate and the bottom plate	
v_{inv}	Velocity of inviscid fluid	
$2l_x$	Length of the vibrating plate	
$2l_y$	Width of the vibrating plate	
E_{Spring}	Young's modulus of springs	Pa
F_{ex}	Excitation force acting to the top plate	N
F_{gap}	Acoustic force from the air in the gap	N
$H(\omega)$	Receptance function	
L_v	Viscous Characteristic Length	

L_{th}	Thermal Characteristic Length	
R_f	Flow Resistivity	
κ	Sitffness of the spring	N/m
c_0	Speed of sound in the air	m/s
p_t	Total acoustic pressure	Pa
$B(s)$	Function for the viscous and thermal effects	
D	Function the temperature profile	
E	Young's Modulus	Pa
R	Specific gas constant of air	
T	Ambient temperature	^oC
c	Damping ratio	Ns/m
k	Reduced frequency	
m	Mass of the top plate	kg
p	Pressure in the air gap	Pa
q	Iterator number	
s	Shear wave number	
ϵ_p	Porosity	
ν_{spring}	Poisson's ratio of springs	
ω	Angular frequency	

$\widetilde{\rho}$	Complex density of the poro-acoustic material	
Γ	Sound propagation constant	
Λ	The viscous characteristic length	
Λ'	The thermal characteristic length	
α_∞	The high frequency limit of the tortuosity	
δ_v	The fluid boundary layer thickness	m
γ	Ratio of specific heats	
λ	The thermal conductivity	$W/(mK)$
μ	The dynamic viscosity of the fluid	$Pa\ s$
ω_n	Resonant Frequency	Hz
ϕ	The open porosity	
ρ_0	Fluid density	kg/m^3
ρ_{spring}	Density of springs	kg/m^3
σ	Square root of Prandtl number	
σ_0	The static air flow resistivity	$Pa\ s/m^2$
τ_∞	Tortuosity factor	
ζ	Damping ratio	

Chapter 1

Introduction

1.1 Vibration control using air film damper

1.1.1 Brief introduction of damping

Currently, most vibration control in industry is accomplished by designing and adjusting the properties of elements such as dampers, springs and occasionally reaction masses. Increasing damping levels is often the easiest way to reduce the vibration of the system without sacrificing performance. Damping is commonly defined as the mechanism that decreases the amplitude of electronic, mechanical, aerodynamic or acoustical oscillations [1]. Damping in a vibrating system involves the loss of energy. It is either radiated away from the system in the form of waves or dissipated within the system. Energy dissipation is most commonly associated with three types of damping. These are viscous, sliding friction (or Coulomb damping) and hysteretic damping (also called structural or material damping) [2, 3].

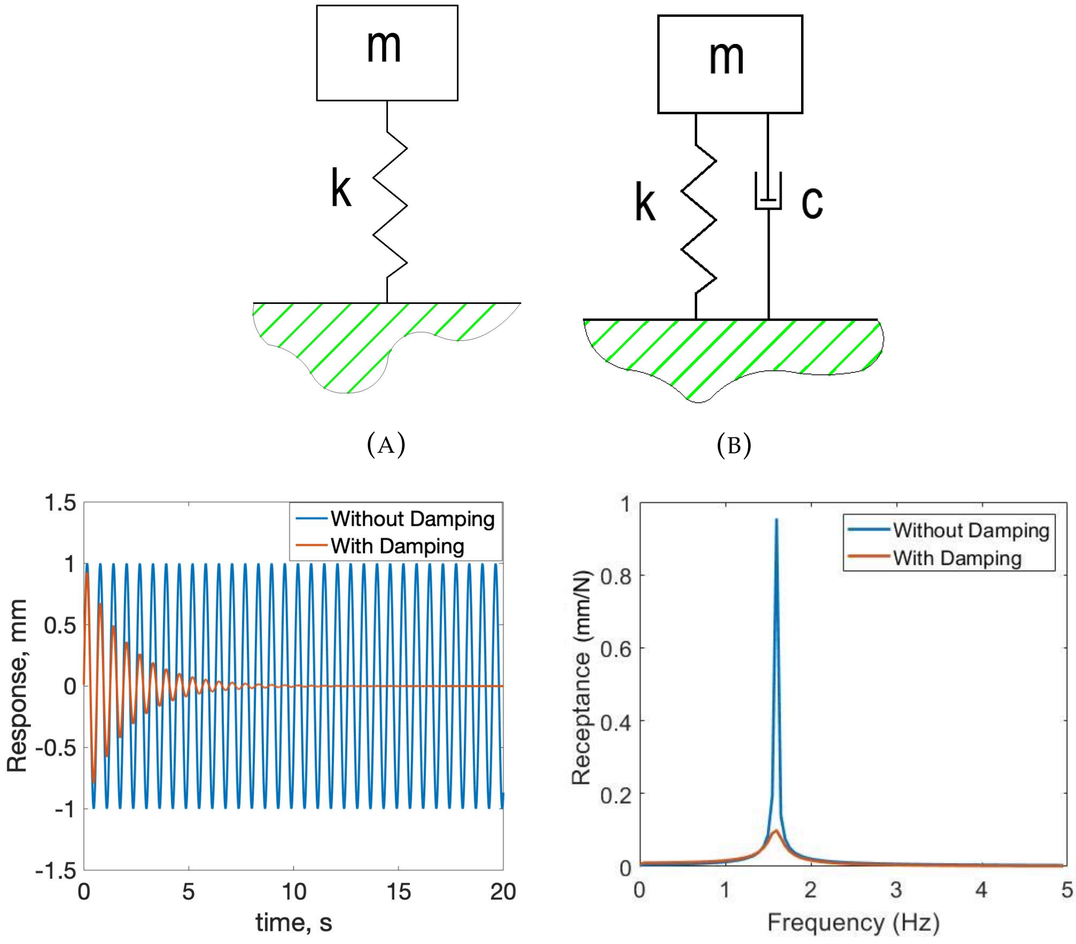

(A) (B)

(C) (D)

FIGURE 1.1: Single degree of freedom system, A: without damper, B: with damper, C and D: impulse time/frequency response

An example that illustrates the effects of damping is briefly discussed here. Figure 1.1a shows a single degree of freedom system with a 0.1 kg mass, spring stiffness ($\kappa = 10$ N/m), and Figure 1.1b shows an same system but with damper ($c = 0.1$ Ns/m). A vertical impulse force is applied to the mass, and the response of the system for both cases are shown in Figure 1.1c. It can be observed that the system without damping would oscillate endlessly. Figure 1.1d shows the frequency response function (FRF) of the system. It also can be seen that the amplitude of resonant frequency has been reduced by the damper. Hence damping is an indispensable factor in machine design. Without sufficient damping, for example, passengers in automobiles or aircraft will experience an uncomfortable, and even dangerous, ride with shock excitation and noise caused by external disturbances, such as rough road condition or aeroelastic effects [4].

1.1.2 Vibration control methods

Vibration control can be both passive and active. Active vibration control has been developed significantly since 1960s [5, 6]. Active vibration control strategies can significantly outperform passive ones as they directly generate opposite forces to cancel the unwanted forces that cause vibration. However, their application is constrained by the size, cost, durability and power requirements of the sensors and actuators [7]. The increasing availability of compact transducers and microprocessor chips has resulted in greater use of active systems in some areas: for example, acoustic noise control, which has been available since the late 1980s [8].

Passive vibration control is a vast subject since there are many different types and strategies for different applications. It mainly reduces vibrations by adding damping materials to the system [9]. Viscoelastic dampers are widely used in vibration control in mechanical and civil engineering especially for dealing with flexural vibration [10–12]. For example, they have been adopted to reduce vibration in tall buildings that experience wind-induced vibration [13]. The typical viscoelastic dampers are usually layers of polymeric material bonded to the vibrating structure. This is also known as "sandwich structure" where energy dissipation occurs through shear deformation in the layer of viscoelastic material.

[14, 15]. The major drawback, however, is that the mechanical properties of the viscoelastic dampers depend strongly on temperature and frequency [16]. Additionally, evaluation of the force-displacement relation is sufficiently challenging to dissuade widespread use in commercial design analyses

In civil engineering, viscous dampers, such as the one shown in Figure 1.2, are widely used in tall buildings to protect from wind loading and seismic events [17]. In mechanical engineering, viscous dampers of a similar structure are most commonly used as shock absorbers. In these dampers, the central piston slides through a fluid chamber filled with highly viscous liquid. The fluid flows through orifices in the piston head as it moves, thus the kinetic energy converts to upstream pressure energy. Compared with typical viscoelastic dampers, viscous dampers can absorb more vibration energy. However, they need to be regularly maintained to prevent leakage and failure.

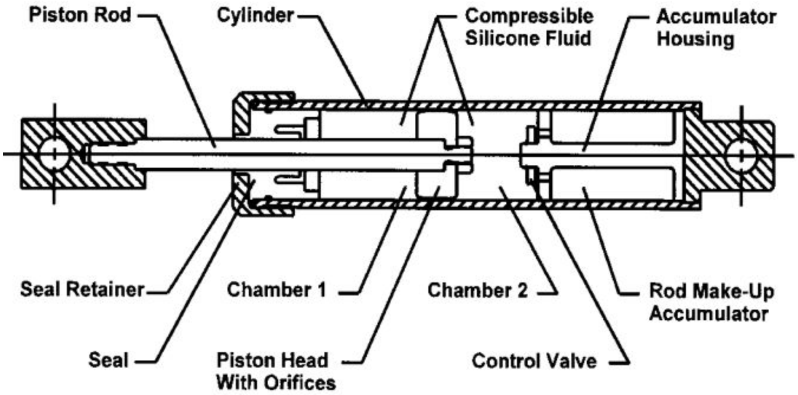

FIGURE 1.2: Typical viscous damper [17]

1.1.3 Air film dampers

This project is focused on a particular type of damper, called an air film damper. A typical air film damper involves a thin layer of air between flexible walls. When subjected to vibration, the walls flex and move relative to one another, causing deformation and displacement of the air layer - as shown in Figure 1.3. An air film damper is in some way similar to classical viscoelastic sandwich damper but the inside layer is a fluid instead of a viscoelastic material. However, for simplicity, most of the relevant research assumes that both walls are rigid with one degree of freedom, as Figure 1.4 shows.

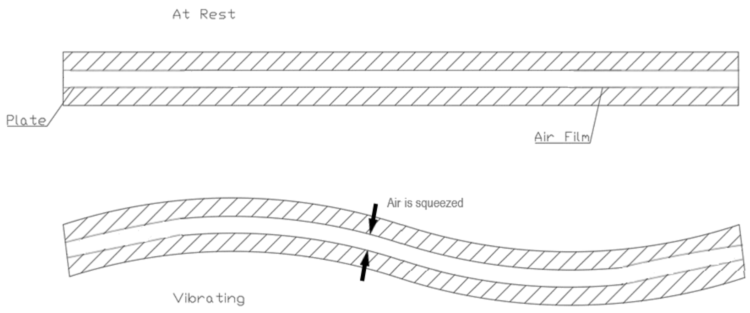

FIGURE 1.3: The typical air film damper

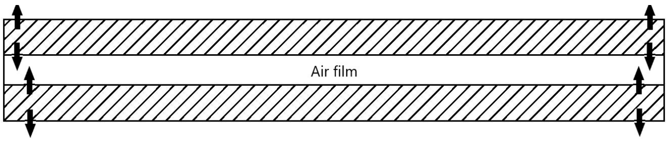

FIGURE 1.4: Simplified air film damper

The effectiveness of an air film damper was first observed and reported by Ungar and Carbonell [18, 19] in the 1960s, when studying vibration energy dissipation in plates with rivets or bolted fastenings. Subsequently, Maidanik [20] provided a theoretical explanation in terms of viscous losses as the gas pumped back and forth within the thin gap between the plate and beam during vibration of the structure. In 1979, Fox and Whitton [21] made some experiments on the cantilever panel plates and investigated the effectiveness of gap thickness and the pressure of the gas. It was found that the thickness of the gap is the main factor that impacts the loss factors. For example, the resonance of the system was reasonably reduced by 0.1 mm air gap thickness.

An air film damper can provide useful levels of damping when the air film is thin. The "thin" is defined as the condition when the air gap thickness is much less than the other dimensions and much smaller than the wavelength of sound in the gas at the frequency of interest [21]. During vibration of the plate, the air inside the thin gap between the plates is pumped back and forth. Therefore, compared with the viscoelastic layers based on hysteretic damping, air film dampers make use of the viscosity of the air within the gap, a property that is significantly less sensitive to temperature. Hence, the air film dampers could be potentially useful, particularly for the scenarios with large temperature differences and wide frequency range. However, to date there is no convenient method or model that precisely predicts the damping effect of an air film damper that has a complex air layer shape.

1.2 Research motivations

The main aims of this research are to develop a suitable numerical model for air film dampers, which accounts for the relevant underlying physics and to use this model to study the design of air film dampers in plate-like structures and further optimise the design for more complex air film geometry. To achieve this aim specific objectives were set. These objectives are listed below:

- To understand existing theoretical models to quantify the significance of design parameters that govern performance.
- To carry out a series of experiments to validate with the theoretical model by measuring the vibration of a plate as it interacts with an air film.
- To establish a numerical visco-acoustic model for air film dampers and validate its effectiveness through comparison with experimental results and existing theory.
- To investigate the validated FE model to design and optimize novel air film dampers.

1.3 Thesis outline

In Chapter 2, a literature review is carried out. A further discussion of viscous damping is presented. Following this, the air film damper is introduced with a discussion of what has been done from previous researches.

In Chapter 3, the low reduced frequency model from Beltman [22–26], which describes acoustical-elastic behaviour of air film damper and includes assumptions that would be applied for further chapters, is introduced. By using this model, the thickness and pressure effect of the air film is discussed and the results are validated with the experiment.

In Chapter 4, an experiment based on the analytical model in the previous chapter is presented. The effectiveness of air gap thickness and pressure are discussed. The objective of this experiment is to validate the low reduced frequency model and the FE model in Chapter 5.

In Chapter 5, an FE model is set up in COMSOL to simulate the air film damper. Besides showing the capability of this model by validating with experiment, this chapter aims to present how the mass and viscous effect can influence the air film dampers with various thickness. Additionally, according to the results of this chapter, the direction of further air film optimization is established.

In Chapter 6, further optimization of the air film damper is discussed in this chapter by introducing some particular geometries. In this chapter, all simulation was made using the JCA model in COMSOL. And by replacing the rigid plate by flexible plate, the optimized geometries have been simulated in more practical condition.

The conclusion of novelty work and some further suggestions are presented in Chapter 7.

Chapter 2

Literature Review

2.1 Fluid viscous effect

Air film damping is generally based on the viscous effects for sound wave propagation. The viscous effect of the air film has been investigated in several disciplines. In fluid mechanics [27–29], the main aim is to calculate the steady-state flow emanating from vibrating plate. In tribology, the viscous effect of air film has been widely applied in the study of journal bearings, which is sometimes known as squeeze film damping [30–33].

The viscous effect in acoustics was first calculated by Stokes [34] in 1868. This theory was extended by Kirchhoff [35] who applied the visco-thermal wave to the sound propagation in a narrow tube. In his theory, the viscous force and the thermal conductivity are taken into account at the same time. Lord Rayleigh [36] developed this theory into sound absorption. Kirchhoff's theory was also extended and simplified by Zwikker and Kosten [37] to fit into intermedia range of frequency, where the shear wave number is much smaller than 1, and the solution for reduced frequency has been established. In this simplified model, the viscous effect and the thermal effect are treated separately.

Lambert [38] practically identified the acoustic damping caused by the fluid viscous effect for the acoustic cavity resonator. Fluid boundary layer thickness is defined as:

$$\delta_v = \sqrt{\frac{\mu}{\rho_0 \omega}} \tag{2.1}$$

where, μ is the dynamic viscosity of the fluid, ρ_0 is the density of the fluid and ω is the angular frequency. As shown on Figure 2.1, a steady flow along the direction of x has a high shear viscous effect close to the wall surface, the thickness of this region is the boundary thickness. Only in this region the fluid viscous effect domains the energy dissipation. This could explain why the air film thickness needs to be 'thin'.

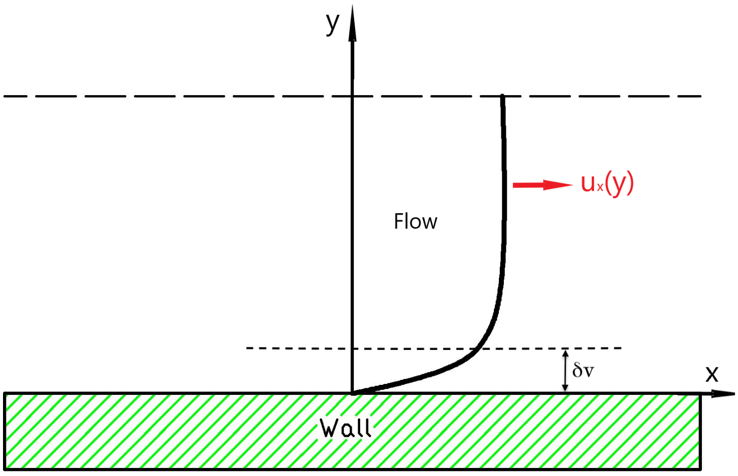

FIGURE 2.1: Calculation of Boundary layer

2.2 Previous studies of the air film damper

Ungar and Carbonell [18, 19, 39] first presented the damping of air film. They riveted two plates together, leaving a particular spacing between them to demonstrate that the air in the gap can work as a damper. Maidanik [20] is another pioneer that introduced the thin gas film into acoustics in the 1960s. A semi-phenomenological theory was developed to predict the loss factor and the gap pressure of the air trapped in slits. He reproduced the experiment made by Ungar and Carbonell to show that a considerable amount of energy is dissipated through the air-pumping effect from the air gap between the beam and plate. Both of the experiments showed that the loss factor is determined by a dimensionless constant relating to the velocity of air and gap thickness. A method that used to estimate the energy dissipation of the joint system was also summarised in their paper, however, the energy dissipation includes all other loss factors besides the visco-thermal loss of the air slit, for instance, the frictional loss of the rivets.

A squeezed air film in a double-wall panel was first investigated by Stefan in 1874 [40]. The Reynolds theory was then extended for arbitrary surface geometry. Based on Stefan's work, in 1886 Reynolds [41] improved this work for two paralleled discs immersed in the viscous fluid. By formulating the equations derived from the Naiver-Stokes equations, the Reynolds' theory was established which is capable to solve the air film cases. However, as the inertial effect is neglected in Reynolds equation, for those situations where the inertial effect must be taken into account, for instance at high frequency or high density of the fluid, the assumption of Reynolds equation breaks down. Therefore, several researchers emphasis the importance of the inertial term of the air layers.

Fox and Whitton [21] developed a model, with taking into account of the inertial effect, compressibility of air and the thermal effects to explore the energy dissipation performance of the air film damper. Based on Reynolds' equation in classical lubrication theory, including an extension for inertia and compressibility effects, they developed a thin-film theory, for panel vibration with lower modes. As mentioned in the previous chapter, the air film can be considered as a thin gas layer as shown in Figure 2.2, which means that the thickness $2h_0$ is much smaller than both other dimensions ($2l_x$ and $2l_y$) and the wavelength of sound in the gas at the frequency of interest. When the top surface vibrates, the air inside the gap is pumped in and out of the through the edges. The pressure distribution across the layer, in the thickness direction, is assumed as constant, while the gas flow in other directions will have a strong shear force. Therefore, the main energy dissipation mechanism within the air film is viscous damping.

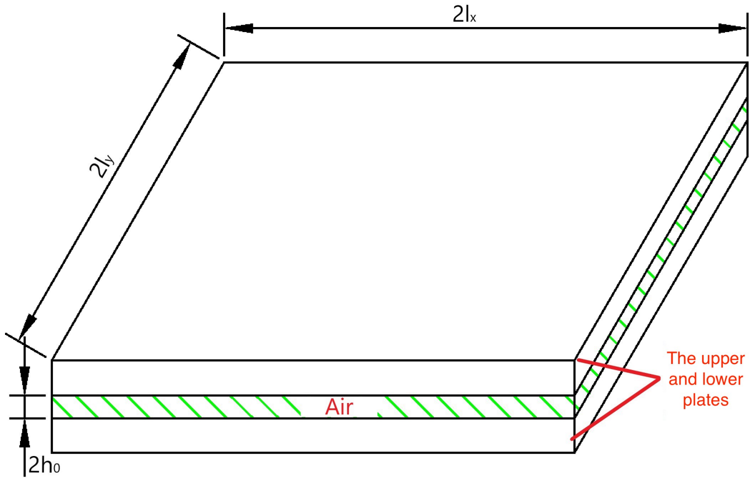

FIGURE 2.2: Air film sketch

A set of experiments was also carried out, aiming to understand the effects of pressure and gap thickness on energy dissipation from an air film incorporated in a plate assembly. In their paper, the "Pumping effect" and "Piston-like effect" were first identified. When the air in the gap displays under the pumping effect, the air flows along with certain directions, the viscosity of air is the main factor of energy dissipation for the system. However, under some conditions, such as high frequency and large viscosity of air, the air in the gap can be directly compressed. This was the so-called "Piston-like effect". In this condition, the velocity of the air is dramatically reduced, hence viscous effects are much lower. In their results, the loss factor for the plate incorporating and air gap showed a rapid rise as the gap was reduced towards 0.07 mm. However, below 0.07 mm, loss factor decreased dramatically. They showed that the energy dissipation from the air film was considerable, and was dominated by the viscous effect. That means the heat conduction during the vibration of two plates separated by a thin air gap is negligible.

Similar to the work done by Fox and Whitton, Onsay [42, 43] investigated the thickness of the fluid layer within a system with including the compressibility and inertial effect. In his experiment, a backing block was used as a base plate which was assumed stable during vibration of the flexible plate which was clamped firmly on both ends. The air was inside the gap between the flexible plate and the base plate with the thickness range from 0.1 mm to 0.5 mm. The results showed that the thickness of layers can change the plate response significantly and at small gap thickness the damping was increased due to the viscous shear force from the air layer. Both Fox and Whitton, and Onsay have used the fully coupled method to investigate the interaction between the vibrating plates and the air film layer. However, as assuming a constant pressure across the air gap thickness, their models are limited to simple geometries.

Trochidis and Kalaroutis [44] developed a model without consideration of compressibility of air, to calculate the loss factor with consideration of the fluid viscosity. The model was validated using experimental data. The energy absorption and damping for the air panel were predicted. Moser [45] extended this model taking account the compressibility of air to study the damping by air between two circular plates. However, no additional test data was produced. Based on Trochidis and Kalaroutis, Chow and Pinnington [46, 47] developed a similar theory but with consideration of compressibility of the air. They introduced the squeeze-film damping into the machinery industry. With their theory and related experiment, it was found that only fluid pumping mass effect and viscous effect can be observed at the incompressible condition. With the compressible condition, the air film performs as incompressible fluid at a lower frequency, and if the frequency goes beyond a critical frequency, then the pumping effect was replaced by the compression behaviour. A further study that replaced the air by oil was also conducted. The result showed that the loss factor obtained with the oil film was quite low, as the loss factor is controlled by the ratio of fluid dynamic viscosity and its density.

Different to the experiment made by Fox et al, in which the air film was open to the atmosphere, Jones et al [48] used a fully enclosed air film plate to show the effectiveness of the damping. In this experiment, the air film was made by a cover platelet on the base plate and the thickness of the gap was varied from 0.025 to 0.05 mm which was below the optimum gap thickness found by Fox et al [49]. The gas inside the air film was assumed to be able to flow within the gap while the cantilever plate was vibrating. The experiment showed a considerable amount of added passive modal damping from the enclosed air film.

A similar experiment was made by Mathison and Dunn [50], in which an open-air film was on the top of a cantilever plate with the gap thickness of approximately 0.127mm. The plate was excited by a piezoelectric crystal in the frequency range of 65 Hz to 6500 Hz under various environmental pressures (vacuum, one atmosphere, two atmospheres and four atmospheres) and the response was measured by 8 strain gauges. They concluded that the air film could change the resonant frequencies of modes significantly, and with the tested thickness of gap, the pressure beyond one atmosphere has little influence on the system damping.

Zwikker and Kosten's approach was used by Tijdeman [51] in the 1990s when considering the viscous effect in cylindrical tubes with a circular cross-section. From his theory, generally, for a given gas, two important parameters, the shear wavenumber and the reduced frequency, can indicate the energy dissipation of the thin fluid layer system. The shear wavenumber ($s = h_0\sqrt{\frac{\rho_0\omega}{\mu}}$) is a measurement for the ratio between inertial effects and viscous effects, where h_0 is half thickness of the air gap thickness, ρ_0 is the density of air and μ is the viscosity of air. Large shear wave numbers mean that viscous effects can be neglected compared with the inertial effects. The reduced frequency ($k = \frac{\omega h_0}{c_0}$) is the ratio of the layer thickness and acoustic wavelength, where c_0 is the speed of sound in the air. The result of the model from Tijdeman shows that for reduced layer thickness, the power is dissipated in the layer and the radiated energy becomes less. The model was extended by Beltman who has made several theoretical and experimental studies aiming to explain the behaviour of air films with vibrating walls [22, 23, 25]. A mathematical model to calculate the pressure distribution in the air gap was developed. This model designated as the "low reduced frequency model", because the solution only depends on the shear wavenumber (s) as the inertial effect is neglected when $k \ll 1$ and $k/s \ll 1$. This model also is simplified to 2-D by assuming the air pressure is constant across the layer thickness. Based on this model a finite element model was also established [26] with the assumption of the rigid plate and no inertial effect. The results from both analytical and numerical model were validated with relevant experiment. In their experiment, a 0.98m by 0.98m plate was suspended by 8 springs and paralleled to the base plate with various distance. The plate was excited and the acceleration was measured by the 4 accelerometers attached on the plate to calculate the resonant frequency. The results show good agreement with the models. However, it seems not possible to maintain the plate with that size as rigid in higher frequency. This analytical model was practically applied to estimate the air load for the satellite solar panels during launch [52].

Basten developed a 2D model for the double-wall air panel based on the Beltman's model [53]. With applied the Kirchhoff plate equation, the damping coefficient corresponding with the plate eigenfrequency for different plates coupling was estimated and compared. A simplified numerical model was established as well based on their analytical model [54]. This analytical model can efficiently predict the dynamic behaviour of the double-wall panel with consideration of the viscothemal effect of the air. However, as the limitation of 2D model, it can only solve the bending modes, and, same as the Beltman's analytical model, the inertial effect and the compressibility of the air lay are not included. The detail of the low reduced frequency model will be used and discussed in Chapter 3 and reproduced to compare with the experimental results produced in Chapter 4.

More recently, Altuğ and Mohan [55] developed an FE model base on the coupling of Reissner-Mindlin plate theory and linearised isothermal Reynolds equation. The effect of parameters, such as gap thickness, pressure and viscosity were investigated. A similar model also presented by Akrout [56] for analysing the fluid viscothermal effect within two laminated glass plates. However, as this model based on the Reynolds equation, the inertial and compressibility of the fluid was neglected, and can only solve simple geometries with low frequency.

2.3 Air film damper in MEMS

The damping effect of the air film is an important consideration for the dynamic behaviour of the microelectromechanical system (MEMS) devices, such as accelerometers, optical switches, resonators, etc. In the MEMS subject, the effect of air film damping can be more significant as in micro-machines which has relatively small volume-to-surface ratio, the effect of surface force which proportional to $(\text{length})^2$, such as the air viscous force, become greater than the volume force which proportional to $(\text{length})^3$, such as mass and inertia [57].

The behaviour of a narrow air gap subjected to vibration is dominated by viscous and inertial properties of the air. However, for very thin air gap thickness with a small displacement of the upper surface, the inertial effect is often negligible [37]. In this case, the Reynolds equation [41] will govern the air film behaviour.

In 1886, Reynolds This theory can be used to solve a large numbers of problems efficiently. The most general form of Reynolds equation is [58]:

$$\begin{aligned} &\frac{\partial}{\partial x}(\rho_0 \frac{(2h_0)^3}{\mu}\frac{\partial p}{\partial x}) + \frac{\partial}{\partial y}(\rho_0 \frac{(2h_0)^3}{\mu}\frac{\partial p}{\partial y}) \\ &\qquad = 6\Big[2\frac{\partial(2h_0\rho_0)}{\partial t} + \frac{\partial}{\partial x}[\rho_0 2h_0(u_1+u_2)] + \frac{\partial}{\partial y}[\rho_0 2h_0(v_1+v_2)]\Big] \end{aligned} \tag{2.2}$$

where p is the pressure in the film, μ is the fluid viscosity, u_1 and u_2 the velocities in the x-direction of the top plate and the bottom plate, respectively, and v_1 and v_2 are the velocities in the y-direction of the top plate and the bottom plate, respectively. As the Reynolds equation assumes that the flow is steady and inertial effect is ignored, it will commonly applied under low frequency and small velocity conditions, for example the squeeze air film in microelectromechanical system (MEMS) [57]. Due to the small dimension of MEMS system, the inertial terms of Reynolds equation can be neglected, the Equation 2.2 can be simplified as:

$$\frac{\partial}{\partial x}(\rho_0 \frac{(2h_0)^3}{\mu}\frac{\partial p}{\partial x}) + \frac{\partial}{\partial y}(\rho_0 \frac{(2h_0)^3}{\mu}\frac{\partial p}{\partial y}) = 12\frac{\partial(2h_0\rho_0)}{\partial t} \tag{2.3}$$

This simplified Reynolds equation is commonly used for the MEMS system to calculate the fluid viscous energy dissipation. For example, Starr [59] has used this equation to estimate the pressure distribution of the air film, which would be applied to design the microstructure of accelerometers.

Andrews et al. [60] experimentally validated the effect of squeeze air film in a silicon microstructure with about 2μm gap thickness in various pressure. The results show that the loss effect of the air layer is higher in atmosphere pressure than in vacuum pressure as the air can be more easily trapped in lower pressure. This result conflicts with the result presented by Fox and Whitton [21].

In MEMS, the plate oscillating displacement amplitude is another concern. Sadd and Stiffer [61] analysed the effect of oscillating amplitude. A non-linearity behaviour has been found in higher frequency, however, from the analytical model in mechanics, for instance, the low reduced frequency model [26] the viscothermal effect is linear to the plate oscillating amplitude.

As the structures of the squeeze air film for the MEMS device are normally too complex that cannot be solved by the analytical model, the numerical simulation is preferred in those cases. In MEMS, the numerical methods based on the Reynolds equation are wildly applied, as it can predict precisely with little computational time [59, 62, 63]. However, as discussed at the beginning of this section, such Reynolds equation-based numerical methods only valid in small displacement. The damping effect of the air film in MEMS can also be solved by the Navier-Stocks equation base CFD tools [64, 65]. Compared with the Reynolds equation-based model, the Navier-Stocks equation-based model can be more accurate, but largely time and performance consuming [57].

2.4 Summary

A review of the literature relating to vibration damping using air films has revealed the following points:

- The viscous effect is the main factor of energy dissipation for the air film damper.
- The Navier-Stokes equation is the fundamental theory to solve the damping effect of air film damper. The Reynolds equation is an alternative method, which is preferred in MEMS, as the inertial term is often neglected.
- When the air damper vibrates at low frequency, the air is normally treated as an incompressible fluid, eg. [44, 46, 47]. However, for the higher frequency, the compressibility of air has to be taken into account [21]. Thus, the critical frequency of the air behaviour transfer from ′pumping′ to the ′piston-like′ can be identified.
- According to the experiment made my Fox and Whitton [21], the ambient pressure will not affect the damping of the air film, but the experiment made by Andrews [60] shows that the damping is lower with lower pressure. Therefore, the ambient pressure effect needs to be valid in the experiment.
- The FE methods so far mainly based on the Reynolds and Naiver-Stokes equation with neglecting of the inertial effect of the fluid. Hence, an alternative numerical method that can precisely predict the damping of the air film with more complex geometries than ever, will improve the design and expand the application of the air film dampers.

Chapter 3

The Low Reduced Frequency Model

3.1 Introduction

In this chapter, a mathematical two-dimensional model for the acoustical-elastic behaviour of air film damper is presented. The model for air is based on the research of low frequency solution mainly developed by Beltman and Tijdeman [22–26, 51, 66].

From this model, the pressure distributions of the air in the gap with various plate size and gap thickness can be predicted. The force from the air in the gap acting on the upper plate was then obtained by integrating the pressure over the air gap area.

In order to describe the effects of air pressure on system damping, as discussed in the literature review, the original model was modified slightly.

3.2 The Low Frequency Model

The low-frequency model is based on the linearised Navier Stokes equations, the equation of continuity, the equation of state for an ideal gas and the energy equation. The following assumptions are made here:

- the heat exchange effect is ignored,
- there is no mean flow,
- medium is homogeneous,
- perturbations are small and sinusoidal,
- flow is laminar.

These assumptions are applicable in engineering conditions, where the air gap thickness is small, the vibration displacement amplitude is small and excitation remains in the low-frequency band. Thus, this mathematical model obtains the air load for the structure by considering the air in between of an oscillating rigid rectangular and paralleled fixed base surface. This assumption will be used throughout this thesis. The distance from the base surface to the top plate during oscillation is given by the real part of the displacement of the upper plate, $\overline{h}(t)$:

$$\overline{h}(t) = h_0[2 + he^{i\omega t}] \tag{3.1}$$

where h_0 is the half thickness of the air film, h is the relative amplitude of oscillation for top plate and ω is the angular frequency. The x and y co-ordinates are in plane and z is normal to the surface as shown on Figure 3.1.

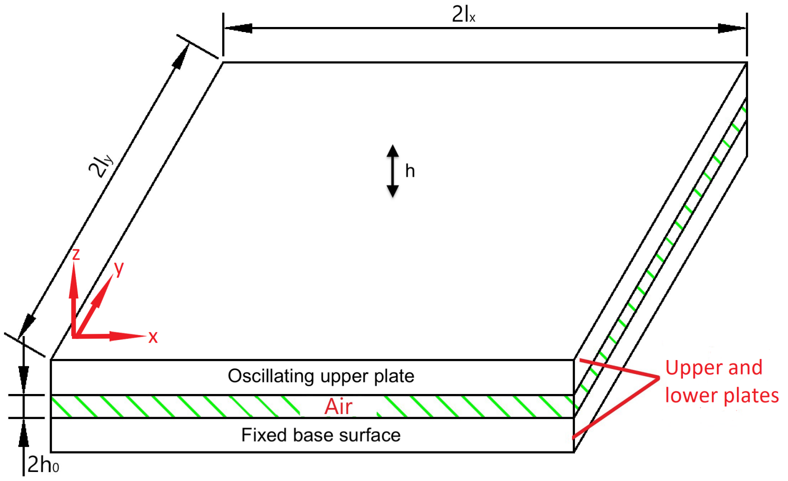

FIGURE 3.1: Coordinates for the analytical model

The dimensionless co-ordinates therefore are:

$$x = \overline{x}/l_x, \quad y = \overline{y}/l_y, \quad z = \overline{z}/h_0, \tag{3.2}$$

where, $\overline{x}$, $\overline{y}$ and $\overline{z}$ are represent x, y and z coordinates, l_x and l_y, as the Figure 3.1 shows, are half length of the plate along x and y directions.

For a thin air gap, in which $g = h_0/l_x \ll 1$ the basic equation for the low frequency model can be simplified to [26]:

$$\frac{\partial^2 p}{\partial x^2} + \frac{\partial^2 p}{\partial y^2} - \Gamma^2 p = n(s\sigma)\Gamma^2 \frac{1}{2} h, \tag{3.3}$$

where Γ is sound propagation constant, B(s) is the function for the viscous effects, $n(s\sigma)$ is polytropic constant which describes the thermal effect, s is the shear wavenumber which is ratio of inertial force and viscous force, σ is square root of Prandtl number, k is the so-called reduced frequency and γ is the ratio of specific heat [66]. Those parameters are respectively given by [26]:

$$\Gamma = \sqrt{\frac{\gamma}{n(s\sigma)B(s)}} \tag{3.4}$$

$$B(s) = \frac{tanh(s\sqrt{i})}{s\sqrt{i}} - 1 \tag{3.5}$$

$$n(s\sigma) = \left[1 + \left[\frac{\gamma - 1}{\gamma}\right] B(s\sigma)\right]^{-1} \tag{3.6}$$

$$\sigma = \sqrt{\frac{\mu C_p}{\lambda}} \tag{3.7}$$

$$s = h_0 \sqrt{\frac{\rho_0 \omega}{\mu}} \tag{3.8}$$

$$k = \frac{\omega h_0}{c_0} \tag{3.9}$$

$$\gamma = \frac{C_p}{C_v}. \tag{3.10}$$

The boundary conditions are:

$$x = \pm k_x \quad \text{and} \quad y = \pm k_y, \quad \text{for} \quad p = 0. \tag{3.11}$$

where k_x and k_y are the normalised wave number vector components along x-axis and y-axis:

$$k_x = \frac{\omega l_x}{c_0} \quad \text{and} \quad k_y = \frac{\omega l_y}{c_0}. \tag{3.12}$$

The solution for the pressure in the air gap is:

$$p(x,y) = \frac{2n(s\sigma)\Gamma^2 k_x k_y h}{\pi} \sum_{q=1,3,5...}^{\infty} \frac{1}{q} \frac{(-1)^{(q-1)/2}}{D^2} \Big[\frac{cosh(\frac{D}{k_x}x)}{cosh(D)} - 1 \Big] cos(\frac{q\pi}{2}\frac{1}{k_y}y), \tag{3.13}$$

where:

$$D = \sqrt{\Big[\frac{q\pi}{2}\frac{l_x}{l_y}\Big]^2 - k_x^2\Gamma^2}. \tag{3.14}$$

If $a = \frac{l_y}{l_x}$ then the force acting on the plate can be obtained by integration over the area:

$$\begin{aligned} F_{gap}(\omega) &= \int_{x=-k_x}^{k_x} \int_{y=-ak_x}^{ak_x} p(x,y)dxdy \\ &= \frac{16n(s\sigma)\Gamma^2 k_x^4 ah}{\pi^2} \sum_{q=1,3,5...} \frac{1}{q^2}\frac{1}{D^2}\Big[\frac{tanh(D)}{D} - 1\Big]. \end{aligned} \tag{3.15}$$

This force is a complex number. The imaginary part of the force can be used to estimate the added damping, whereas, the real part of the force relates to the added mass and added stiffness effect of the air [22, 23].

3.3 Results

In this section, the effect of the air gap thickness and ambient pressure are assessed using the low reduced frequency model. With showing on Figure 3.1, both upper and lower plates are assumed rigid. In order to compare the results from different methodologies, the same size of plate was used for both the numerical and experimental analysis in following chapters, the plate is unified as

250 × 180mm. The table below shows the parameters used in this model.

Parameter	Symbol	Value	Unit
Length of plate	$2l_x$	250	mm
Width of plate	$2l_y$	180	mm
Air gap thickness	$2h_0$	0.1, 0.3, 0.5, 1, 2, 5	mm
Ambient pressure	p_0	1.01×10^5	Pa
Viscosity of air	μ	1.81×10^{-5}	J/(kg K)
Density of air	ρ_0	1.206	kg/m^3

TABLE 3.1: Key parameters for the low reduced frequency model

The pressure of the air in the gap can be calculated using Equation 3.13. Figure 3.2 shows the normalised pressure (p/h_0) of the air for the 0.3 mm gap thickness at 15 Hz. The maximum pressure occurs in the centre of the plate, whereas the pressure tends to ambient about the edges.

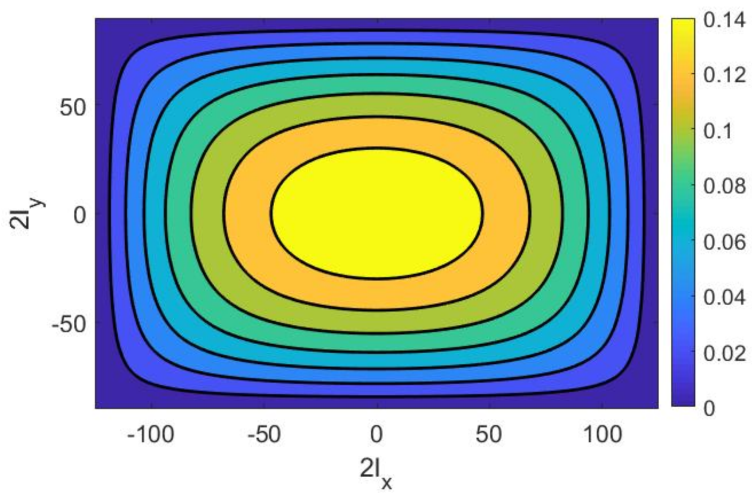

FIGURE 3.2: Normalised pressure distribution of the air in the gap

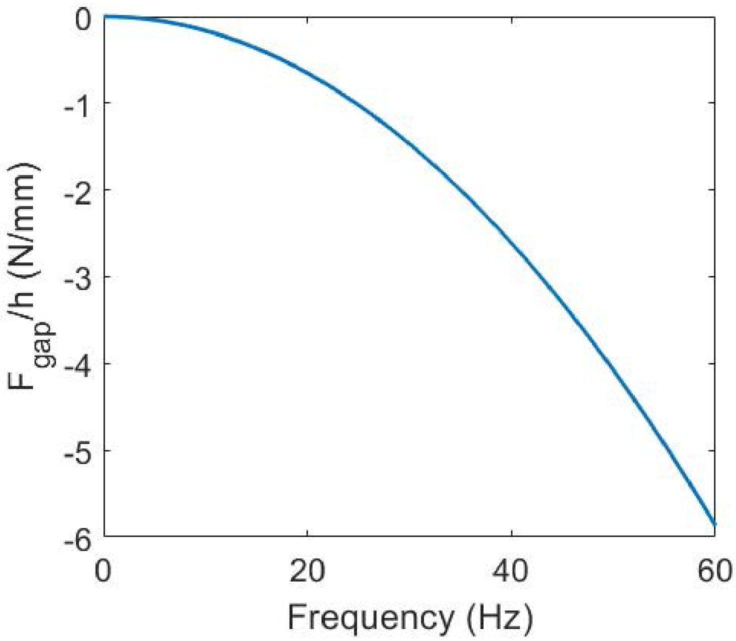

(A) Real Part

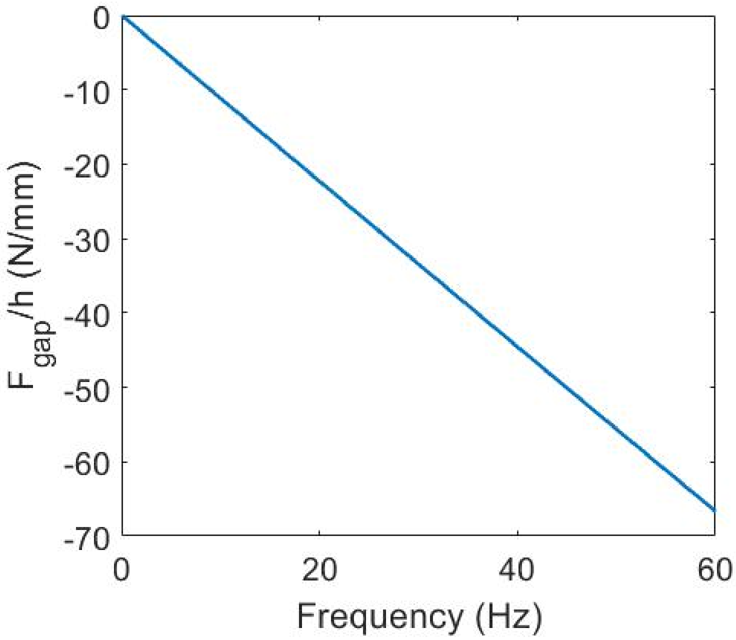

(B) Imaginary Part

FIGURE 3.3: The real (A) and imaginary (B) parts of results (F_{gap}/h) for $h_0 = 0.1$ mm

The force applied by the air to the upper plate can be calculated using Equation 3.15. Results for the 0.1 mm layer are presented in Figure 3.3 while the other gap thicknesses appear in Figure 3.4. The plot for 0.1 mm is shown separately because the real part of the force is negative at this thickness, whereas it is positive for the thicker layers. This difference can be explained by noting that the real part of the force is dominated by the mass effect and the bulk modulus of air. The mass effect depends on the density and displacement of air, while the bulk modulus affects the stiffness of the air layer. In a very small air gap, where the thickness that is smaller than the boundary layer thickness, the air has to travel, by proportion, a greater distance before it reaches the free surface at the edge of the plate. As the mass effect is proportional to the kinetic energy of the air, the importance of this effect increases with the square of the distance the air travels. Hence, for a thin layer, the inertia term (which is negative) dominates the real part of the force.

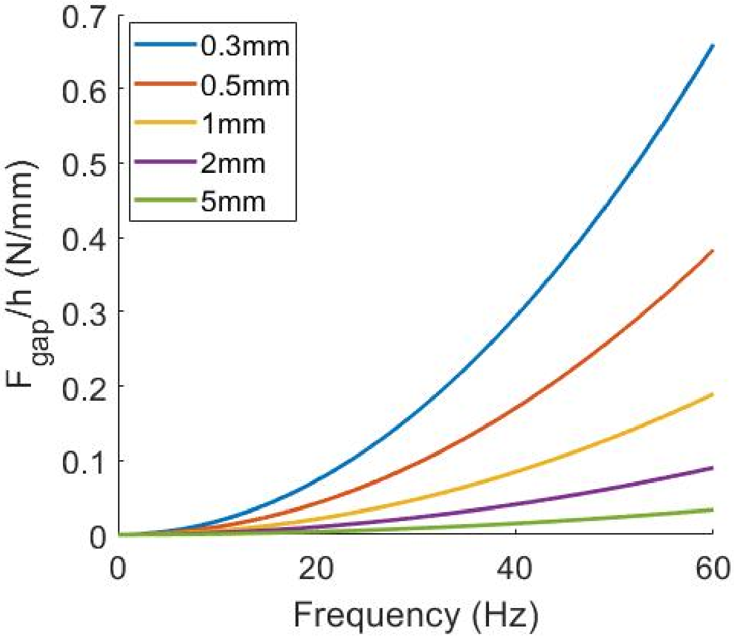

(A) Real Part

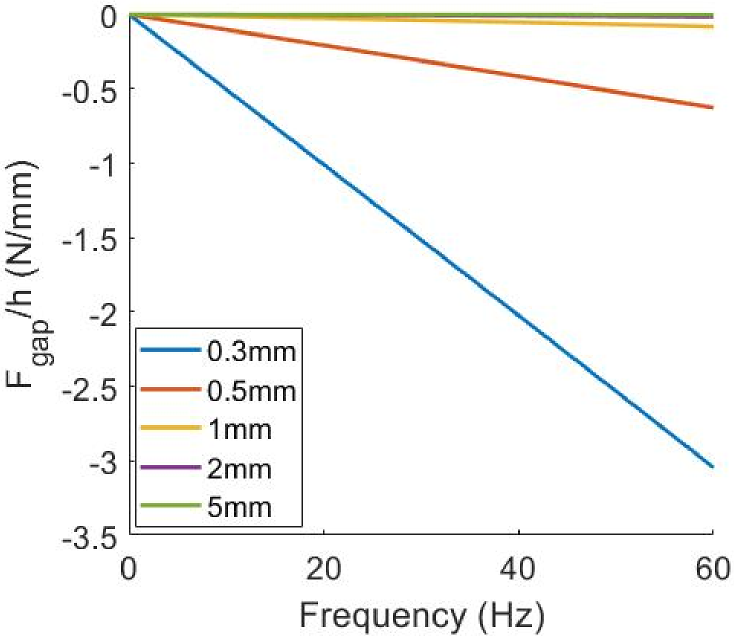

(B) Imaginary Part

FIGURE 3.4: The real (A) and imaginary (B) parts of results (F_{gap}/h) for $h_0 = 0.3, 0.5, 1, 2$ and $5mm$

It can also be seen that the imaginary part of the force is very much higher for thin air layers than for thick ones. The relationship is distinctly non-linear. This can be explained by considering the acoustic boundary layer. Figure 3.5 shows the acoustic boundary layer thickness for air calculated using Equation 2.1 and the parameters in Table 3.1. It can be seen that in the narrowest gaps, all the air is within the acoustic boundary layer whereas for the wider gaps (1 mm and greater) much of the air is beyond the boundary, particularly at higher frequencies.

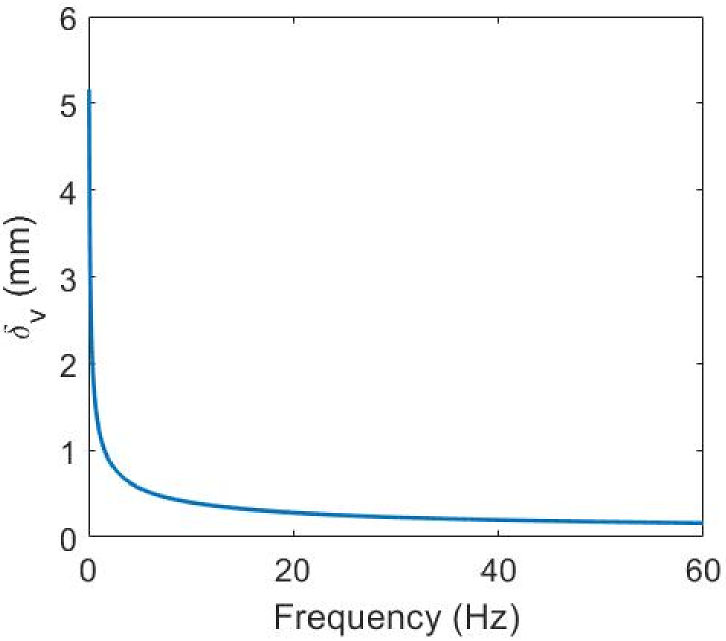

FIGURE 3.5: The boundary layer thickness of the air with corresponding frequency

3.3.1 Pressure influence

The purpose of this section is to compare the model predictions against experimental data on the plate vibration obtained for the reduced air pressure. In order to make this model capable with various pressures, two equations were added [67], which are the pressure-dependent density of the air $\rho_0(p_0)$ and speed of sound in the air $c_0(p_0)$, respectively,

$$\rho_0 = \frac{p_0}{RT} \tag{3.16}$$

$$c_0 = \sqrt{\frac{\gamma p_0}{\rho_0}} \tag{3.17}$$

where $R = 287.06$ is the specific gas constant of air and T$= 298K$ is the ambient temperature. Besides the 'normal pressure', which indicates the standard atmosphere pressure, the response of the plate was modelled for additional gauge pressures of -0.4, -0.6, -0.8 and -0.95 bar.

Figure 3.6 and 3.7 show the normalised real and imaginary parts of the force acting to the upper surface under various pressure for 1mm and 2mm gap thickness, respectively. It can be observed that the pressure impacts on the real part of the force is much more significantly than on the imaginary parts. Therefore, it can be predicted that the air pressure would more affect the resonant frequency of the system with less contribution to the system damping. This will be discussed in the next chapter, once the parameters of the system, such as the mass of the plate and the stiffness of the springs, are experimentally measured.

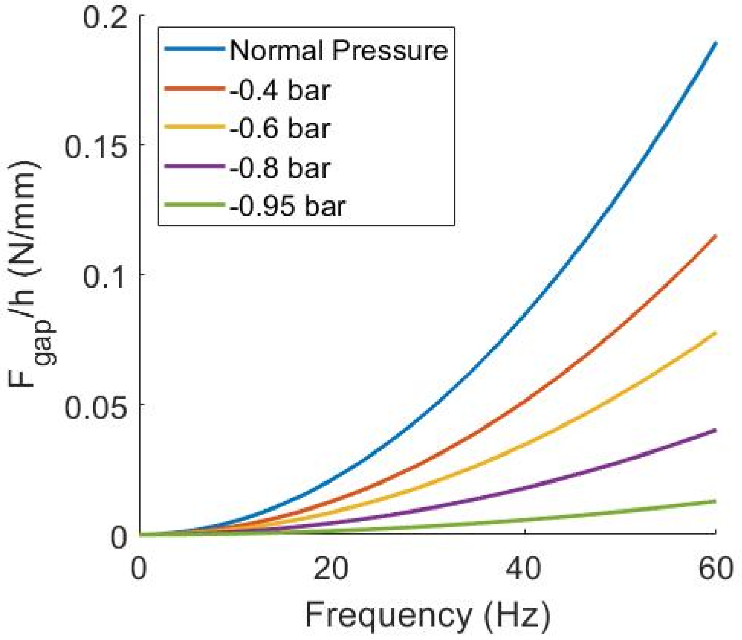

(A) Real Part

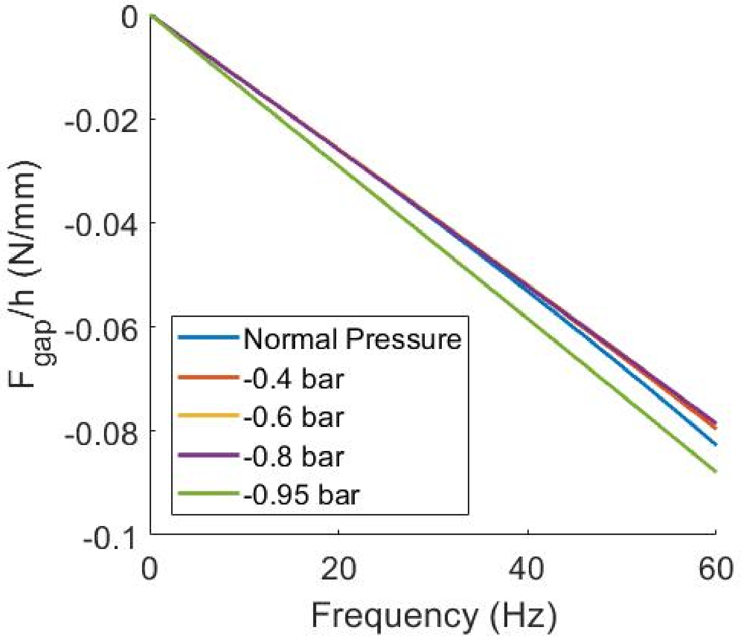

(B) Imaginary Part

FIGURE 3.6: The real (A) and imaginary (B) parts of F_{gap}/h at 1mm slit for different pressures

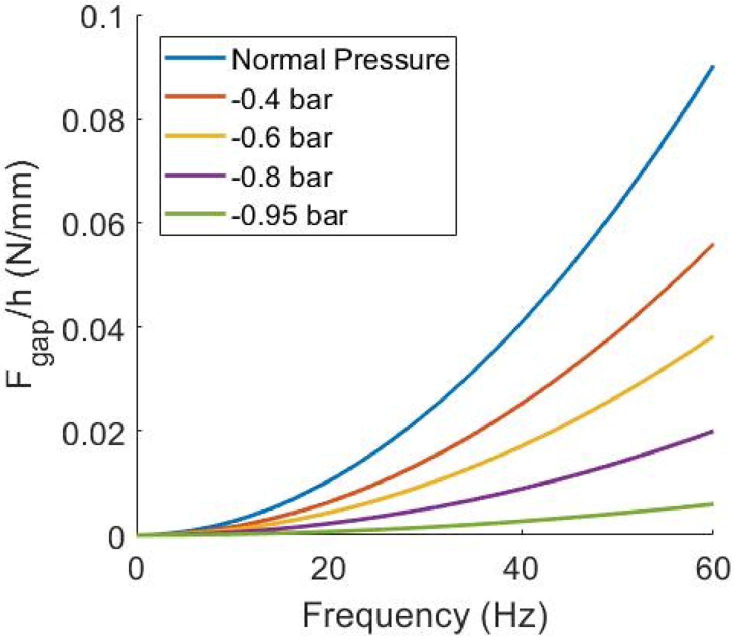

(A) Real Part

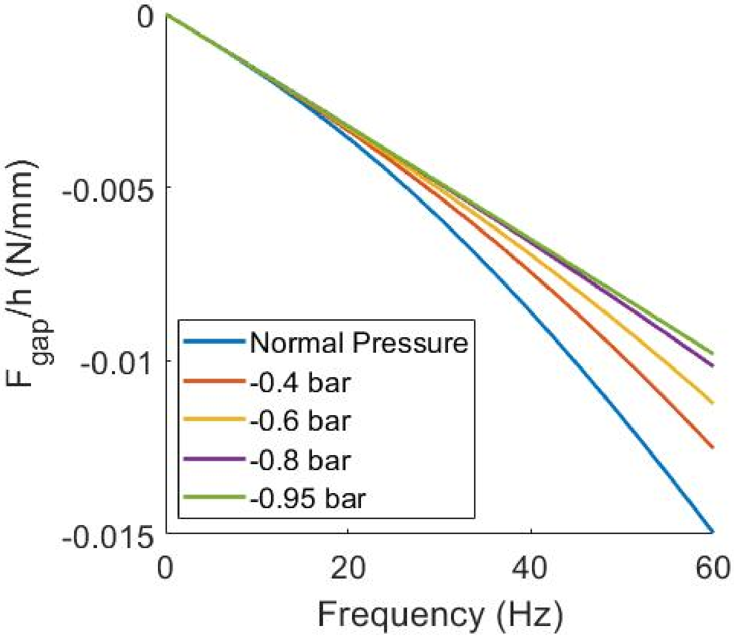

(B) Imaginary Part

FIGURE 3.7: The real (A) and imaginary (B) parts of F_{gap}/h at $2mm$ slit for different pressures

3.4 Summary

From this chapter, the mathematical model developed by Beltman and Tijdeman was reproduced and the force acting to the upper surface from the air was calculated for various air gap thickness. Results will be compared with those from experiments in the next chapter. This model was also allow for changes in various pressure, by additionally introducing the function for air density and speed of sound.

The air pressure can influence the dynamic response of the system, as the results from this model, the reduced pressure can shift the resonant frequency and increase the system damping. In the next chapter, the impact of the air pressure will be discussed under the system level.

Although this mathematical model can calculate the pressure and force acting the top plate, it has some limitations that restrict its wider use. Firstly, it can only be applied for simple geometries. Secondly, the author has noticed that the force acting on the upper plate from this model are almost linear with frequency, even in very small air gap with high viscous fluid in the gap, as Figure 3.8 shows the real and imaginary part of force for $0.1mm$ air gap at normal ambient pressure with increased 10 times of the original air viscosity. It can be observed that both real and imaginary part are almost linear to the frequency. However, in practice, for a 0.1 mm slit with this size of plate, the air would be compressed at higher frequencies. As a consequence of this, it can only be used for pumping behaviour rather than combined with piston-like behaviour. These will be compared with the results from the FE model and discussed in the further chapters.

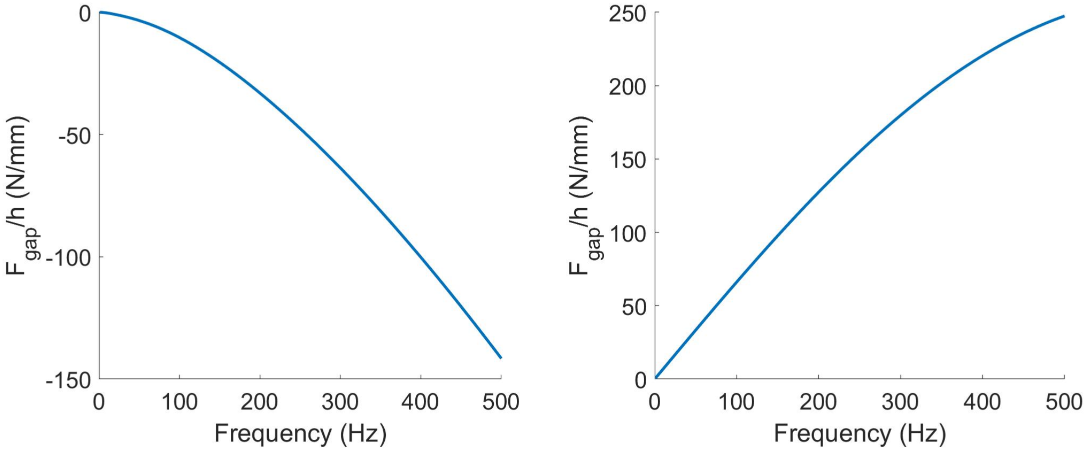

(A) Real Part (B) Imaginary Part

FIGURE 3.8: The real (A) and imaginary (B) parts of F_{gap}/h at normal ambient pressure with ×10 viscosity for 0.1mm thickness

Chapter 4

Air Film Experiment

4.1 Introduction

In this chapter, experiments are described to understand how the air film thickness and its ambient pressure could impact the damping and added mass effect to the system as the density of the air changes with the ambient pressure. These results will be used in the following chapters to validate the proposed mathematical model and FE model simulations.

4.2 Experiment setup

In this experiment, the mobility FRF for different gap thickness and ambient pressure is compared to identify the contribution of the air film in terms of damping and mass effect. The experiment made by Beltman [26] has a good capability to illustrate the damping property of the air in the gap, however, as mentioned in the literature review, the plate was too large to be rigid, especially in higher frequency, and the impact of the ambient pressure is not considered. Fox and Whitton made a relevant experiment [21], however, they used screws to secure the two plates. This will add extra frictional damping to the results. Therefore, a new experiment was designed as presented in this chapter.

To achieve that the experiment rig was set up and details are shown on Figures 4.1 to 4.4.

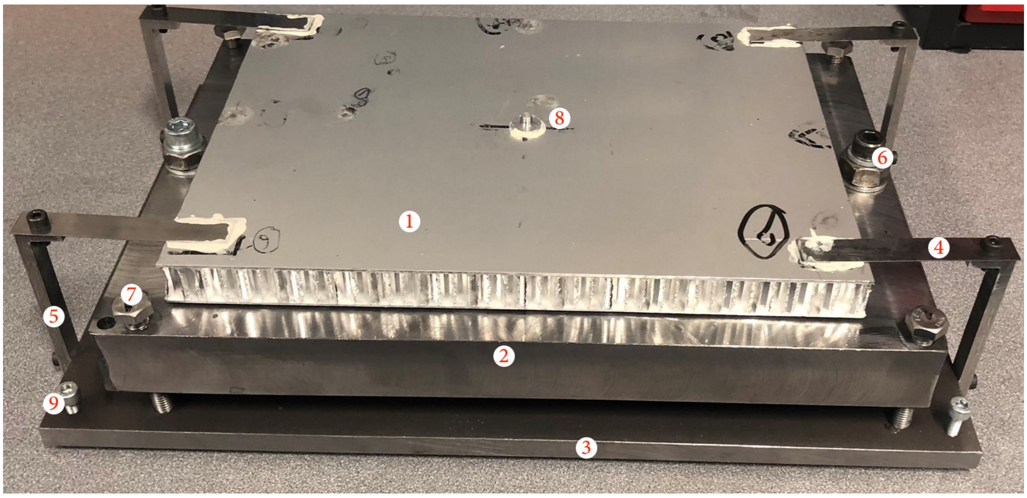

FIGURE 4.1: The rig setup (the air film is in between **1** and **2**)

Figure 4.1 shows:

- **1**: the upper surface made from aluminum honeycomb plate (15 × 180 × 250 mm);
- **2**: the lower surface made from steel;
- **3**: the base plate which connected with four springs supports and hold the lower surface;
- **4**: four springs which are made from carbon tool steel;
- **5**: four supports to fix and hold the springs and top surface as well;

- **6**: two bolts which go through the bottom block and fastened on the base plate. These can fix the lower surface block firmly to the base plate;
- **7**: four bolts with screw thread, which are used to support the lower surface and to adjust the level for each corner of the lower surface in order to get a certain thickness of the air gap;
- **8**: the connector to shaker;
- **9**: three bolts (two on the front and another on the middle of the block) which support the base plate (**3**) and can adjust its level until normal to the shaker.

The air film is located in between the upper surface (**1**) and lower surface (**2**). The upper surface was suspended from four springs made from metal shim. (**4**). The suspension was designed to provide flexibility perpendicular to air film whilst restraining motion parallel to it with minimum energy loss. In addition, the design was compact, enabling the use of the available vacuum chamber. This rig was set in the middle of the vacuum chamber and the top plate was connected with a shaker as Figure 4.2, 4.3 and 4.4 shows.

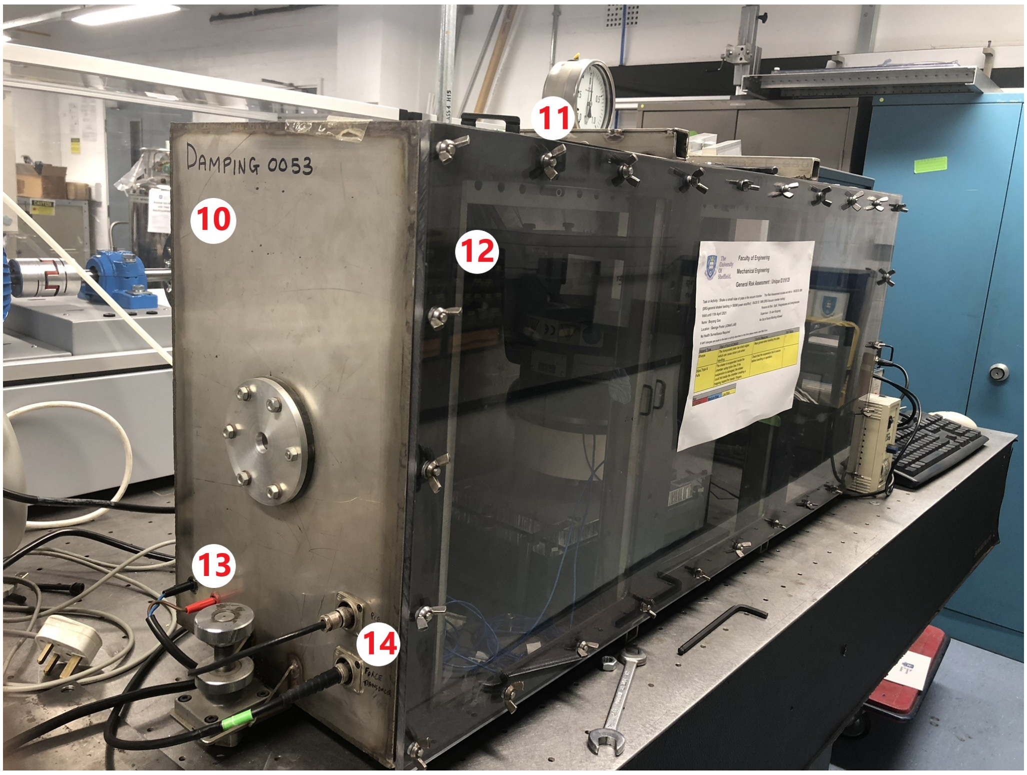

FIGURE 4.2: Side view of the vacuum chamber

In Figure 4.2:

- **10**: the vacuum chamber, made from structure steel with size about 450 × 700 × 1400 mm,
- **11**: the pressure gauge, which indicates the pressure inside of the chamber,
- **12**: the 20 mm thick front cover made from PMMA,
- **13**: power connectors for the shaker with sealing rubber layer inside,
- **14**: sensor signal connectors for the force transducer and accelerometer, with sealing rubber layer inside.

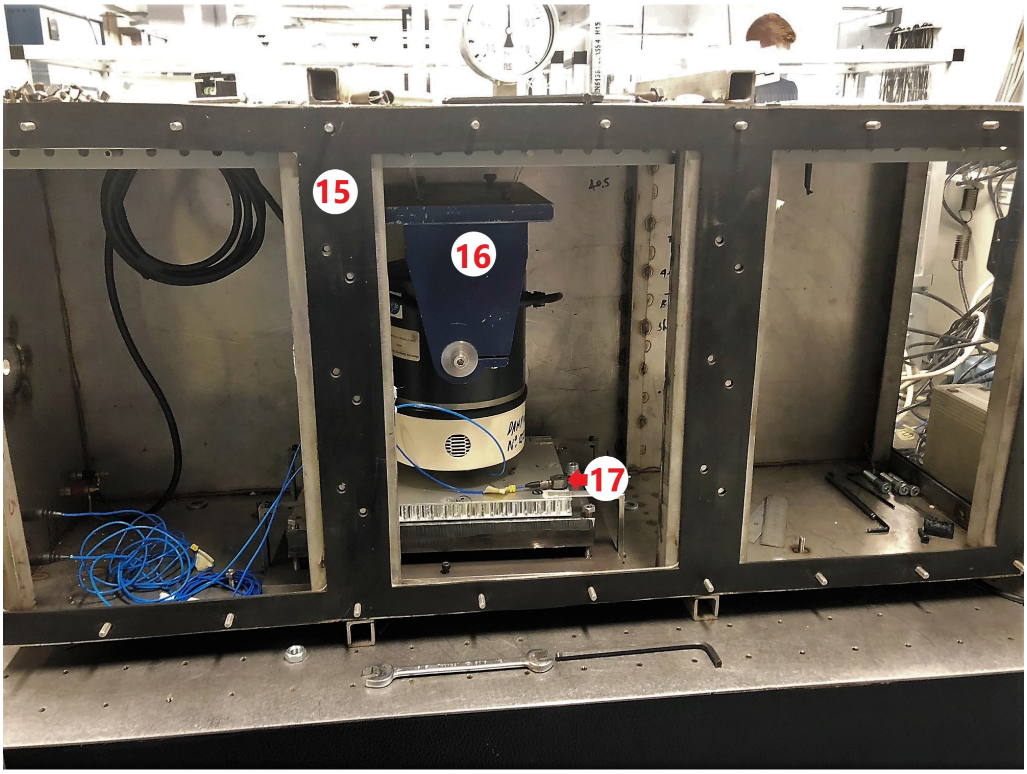

FIGURE 4.3: Front view of the rig sit in the vacuum chamber

In Figure 4.3:

- **15**: the seal rubber for the front cover,
- **16**: the shaker,
- **17**: the accelerometer (12g weight) placed on corner of upper plate.

FIGURE 4.4: Side view of the rig sit in the vacuum chamber

In Figure 4.4:

- **18**: air nozzle connected to the vacuum pump,
- **19**: the force transducer connected between the shaker and (**8**).

The air film is located in between the upper (**1**) and lower surface (**2**). The thickness of the gap can be adjusted by up to 10 mm by this rig and the minimal could achieve 0.3 mm by referencing with feeler gauges. The shaker was suspended by four nylon strings and the level gauge was used to make sure the shaker was suspended vertically. A force transducer was connected between the plate and the shaker.

According to the previous chapter, the top plate was assumed as rigid. Therefore, in order to minimize the influence from the upper plate to the system, the upper plate was chosen as aluminium honeycomb plate, with only 0.32 kg for its 15 × 180 × 250 mm size. It was made from aluminium honeycomb core foil adhered in between two 1.5mm aluminium sheets, as Figure 4.5 shows. Because of the structure, it has very high stiffness and low mass. From an instrumented hammer test, it was found that the first bending mode of the plate was above 1000 Hz. Thus, it can move as a lumped mass at frequencies well-below its first resonance.

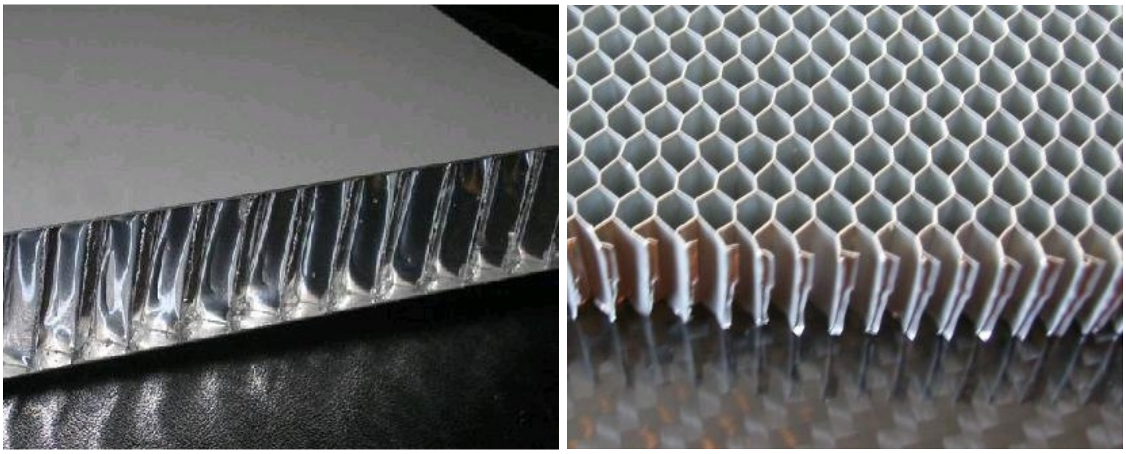

FIGURE 4.5: Aluminium honeycomb plate and its structure

The bottom plate was made of steel so that its high mass (approximately 30 kg) minimised the influence of the structural resonance. By using FE modal analysis, the lowest resonance of this plate was predicted more than 800 Hz, hence it can be fully treated as a stiff surface during the experiment. The surface of the base plate was processed by the milling machine and the surface of the honeycomb plate was made by the 1.5mm aluminium sheet. The flatness of both surfaces are smaller than 0.05 mm, therefore, the influence of the flatness of the surface can be ignored in this experiment.

Both the spring and shaker connector, as Figure 4.6 shows, were mounted on the top of the aluminium honeycomb plate using strain gauge adhesive (X60 methylmetacrylate).

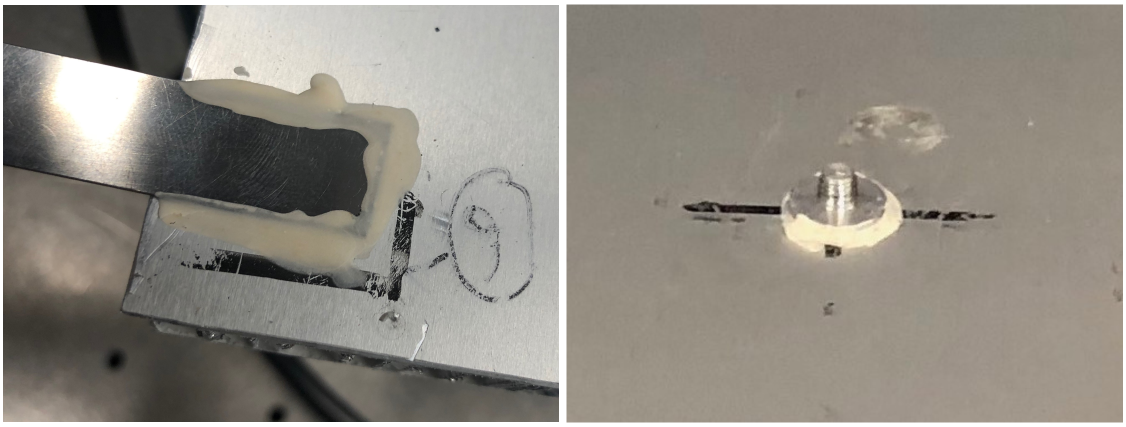

FIGURE 4.6: Spring (left) and shaker connector right) were adhered on the upper plate

The carbon tool steel shim (0.3 mm thick) was selected as the spring instead of normal spring because of the limited space and lack of fixing points inside of the vacuum chamber. They were cut from standard feeler gauges, therefore they were guaranteed have consistent and accurate thickness.

In order to get physical properties for the metal spring, such as density, Young's Modulus, which will be used at further FE modal simulation, an extra test was made and presented in Section 4.3.

4.3 Physical properties of metal springs

An experiment was carried out to estimate Young's modulus of the material from which the supporting springs were made. This was achieved by measuring the frequency of the first mode of the spring. The parameters in FE modal analysis were then adjusted to fit the model with experiment.

4.3.1 Experiment

A feeler gauge strip of the same kind as used for the spring (0.3 x 12.65 mm cross-section) was clamped at one end using two metal blocks, providing a cantilever arrangement with a free length of 70 mm, as shown in Figure 4.7. A laser displacement sensor was used to monitor the deflection of the spring surface. The spring tip was deflected by about 20 mm and then released to record the history of time-domain-displacement. The data was captured by the PicoScope with a sampling rate of 20000 Hz. The captured time-domain data were analysed to determine the frequency of the first resonance.

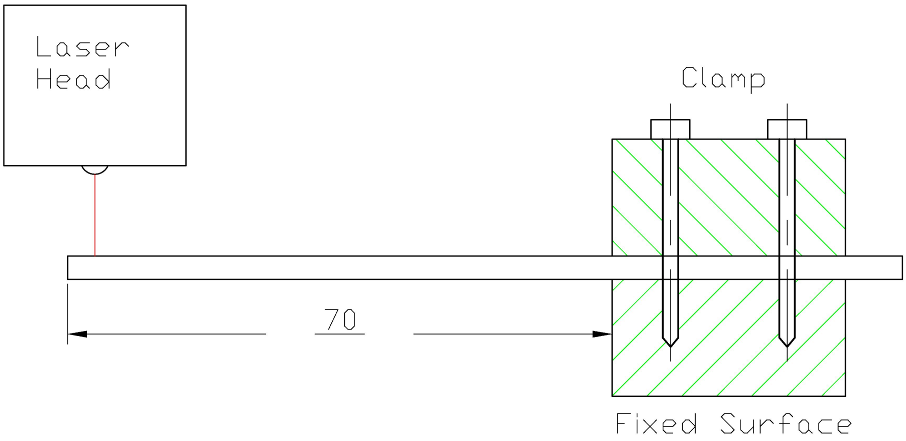

FIGURE 4.7: Experiment setup for dynamic stiffness of springs

The first natural frequency for this 70 mm long cantilevered metal was 52.8 Hz. The mass for the whole feeler gauge (300 mm in length) was 9.00 g giving the density of this material as 8024.5 kg/m^3.

4.3.2 FE fitting

The FE model for the free portion of the cantilever used in the test, was constructed using ANSYS - as shown in Figure 4.8. The Poisson's Ratio was set as 0.28 - midway in the range of values (0.25-0.30) that are quoted in literature. In reality, altering this value of the possible range had little effect as flexural behaviour of a beam is controlled primarily by the Young's modulus, as an increment in the Poisson's ratio by 0.02, the model frequency only raised by 0.25 %.

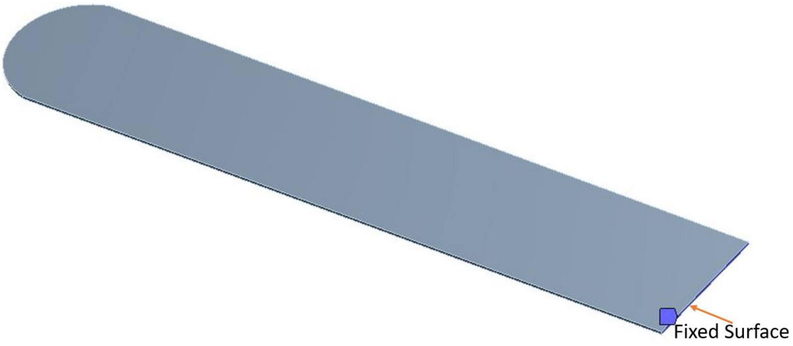

FIGURE 4.8: FE model for the springs

The Young's modulus was then adjusted so that the first natural frequency matched the experimental result of 52.8 Hz. After several iterations, it was found that when the Young's Modulus was 2.07×10^{11} Pa, then the modal frequency was 52.85Hz.

In conclusion, the physical properties of this spring material were:

- $\rho_{spring} = 8024.5$ kg/m^3,
- $E_{spring} = 2.07 \times 10^{11}$ Pa,
- $\nu_{spring} = 0.28$.

These values were used with both the low reduced frequency model and later FE analytical work.

4.4 Hammer test and modal analysis

When the honeycomb panel was attached to the springs, an extra validation test was needed. This was because it was judged that the springs were not aligned perfectly along the x and y axes and the clamping conditions between the panel and spring did not reflect cantilever conditions perfectly. A hammer test was conducted first to measure the natural frequency of the top plate with the metal springs as illustrated in Figure 4.9. The results were then compared with the FE modal analysis which was carried out with ANSYS. The PicoScope with 20000 Hz sampling frequency was used during hammer test to record time-domain data from the accelerometer. The frequencies of first three resonances were then determined with a fast Fourier transform (FFT).

During the hammer test, the accelerometer was placed at a corner of the top plate to maximise the number of modes which could be resolved with such a setup. Due to its symmetry in the plate geometry, only 4 impact points were marked as Figure 4.9 shows.

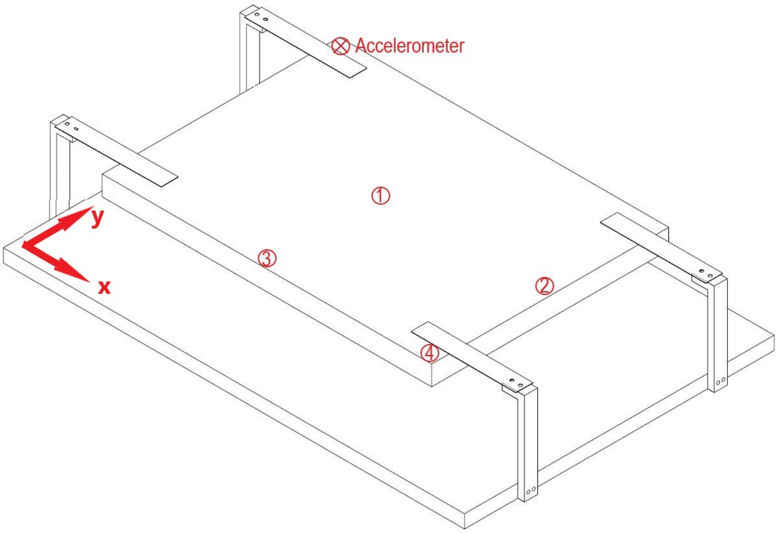

FIGURE 4.9: Hammer test setup and positions of impact points

To minimise the effect of the air in the air gap below the plate, the bottom block was removed in this impact hammer experiment. According to the results of the FE simulation, the whole body mode for the structure is that the top plate moves straightly up and down, as shown in Figure 4.10. From the impact hammer test, the whole body mode with displacement in the vertical direction can be easily excited and observed by knocking point **1** (see Figure 4.11). The resonant frequency of such whole body mode from the experiment was 15.2 Hz, that was in a good agreement with the FE prediction result, which was 15.01 Hz.

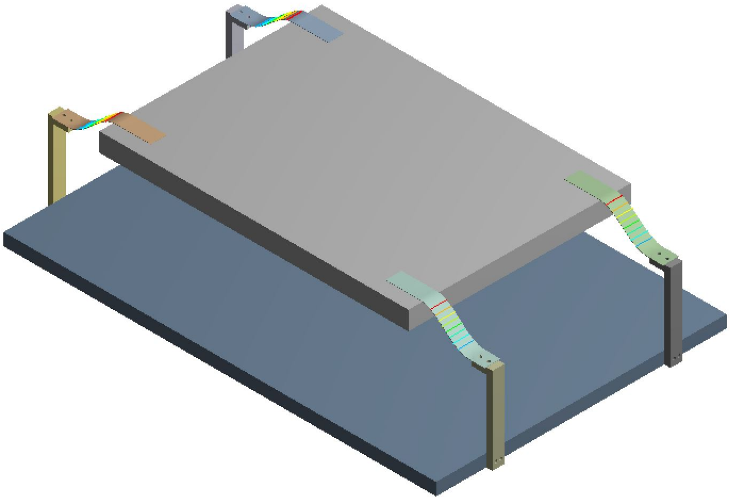

FIGURE 4.10: Whole body mode from FE simulation (15.01Hz)

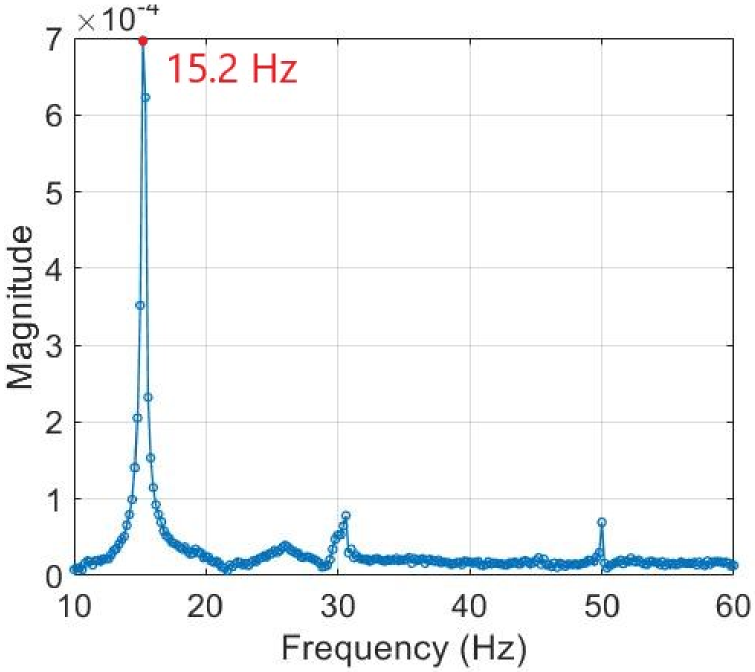

FIGURE 4.11: Frequency spectrum of impulse point **1**

The second and third modes are the x-axial and y-axial rocking modes for the top plate, as illustrated with an FE simulation shown in Figure 4.12. Therefore the impulse points 2 and 3 are the node points for the second and third mode shapes. The resonant frequencies for these modes were predicted at 20.83 Hz and 29.08 Hz, respectively.

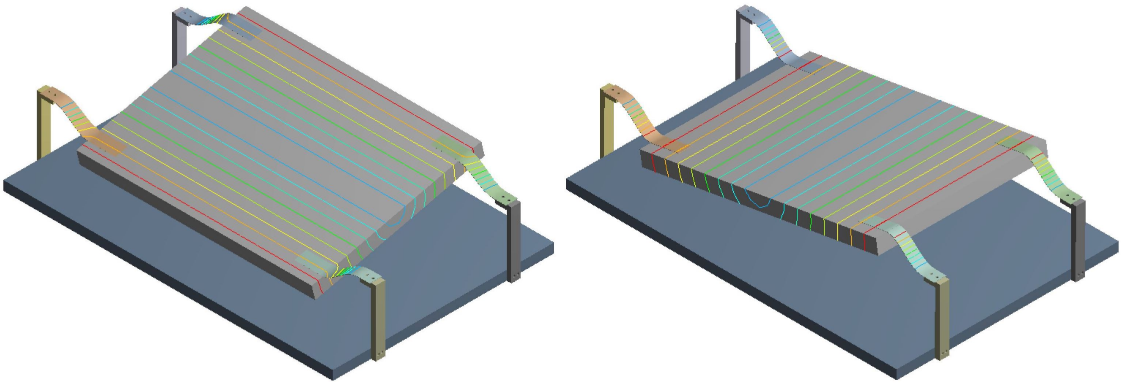
(A) Second Mode (20.83Hz) (B) Third Mode (29.08Hz)

FIGURE 4.12: A: second and B: third modes from FE simulation

According to Figure 4.13, the resonant frequencies for the second and third modes from the impact test were 22 Hz and 29.5 Hz. Compared with the FE results, there was only 5.3% and 1.4% difference for these two resonances, respectively. Therefore, these were in good agreement with each other.

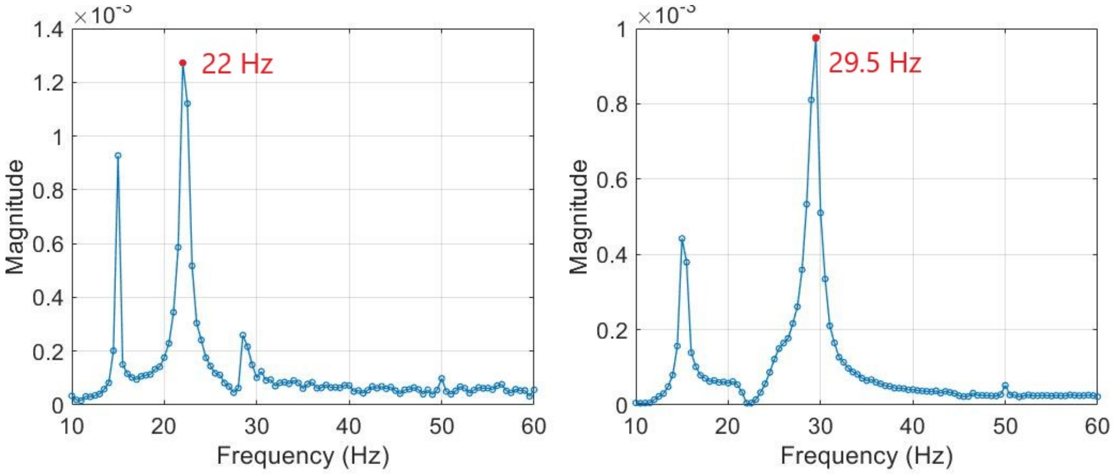

(A) Impact Point **3** (B) Impact Point **2**

FIGURE 4.13: Frequency spectrum of impulse A: point **3** and B: point **2**

Figure 4.14 shows the results of knocking point **4** on the top plate. The first three modes can be observed in this figure and the corresponding resonant frequency can be matched well with those obtained by impact hammer test made at other impact points.

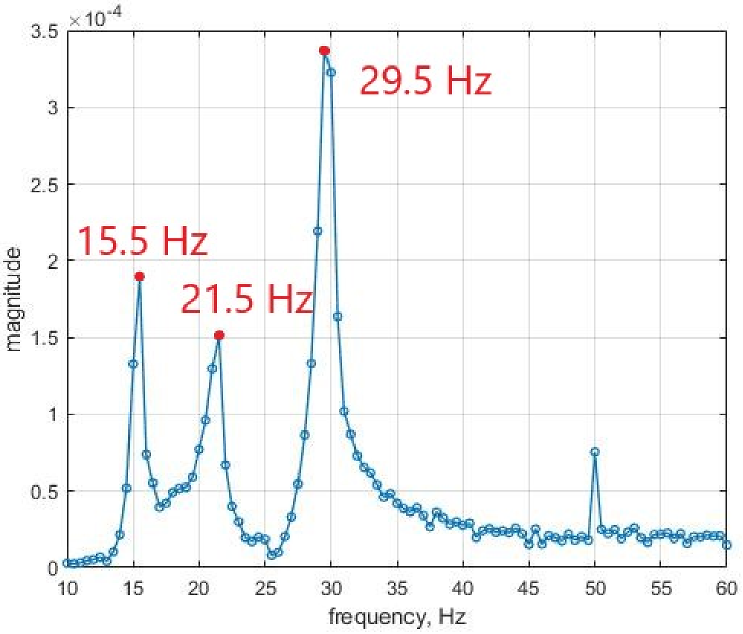

FIGURE 4.14: Frequency spectrum of impulse point **4**

In conclusion, the comparison of the hammer test and modal analysis helped to rule out two uncertainties. One is the physical properties of the supporting springs, which include Young's modulus and Poisson's ratio. The other is the potential influence of the imbalance mounting of the supporting springs. Because when the springs were being glued on the top surface of the aluminium honeycomb plate, it cannot be perfectly balanced and symmetry, as the result, it might affect the natural frequencies and patterns of the plate vibration.

4.5 Stiffness of springs

Since in the following chapter, the data will be compared and validated with this experiment, the stiffness of the supporting springs has to be identified. In this section, an FE static structural analysis was carried out using ANSYS to predict the stiffness of the springs when the upper plate moves up and down.

The geometry was used in ANSYS static structural module is exactly the same as what was applied in the previous section. By fixing the bottom plate, a 10 N force acted normal to the top plate as Figure 4.15 shows. The deformation of the top plate was calculated in ANSYS as 2.3×10^{-3} m. Therefore, combined stiffness of the springs was, therefore, 4.26×10^{3} N/m.

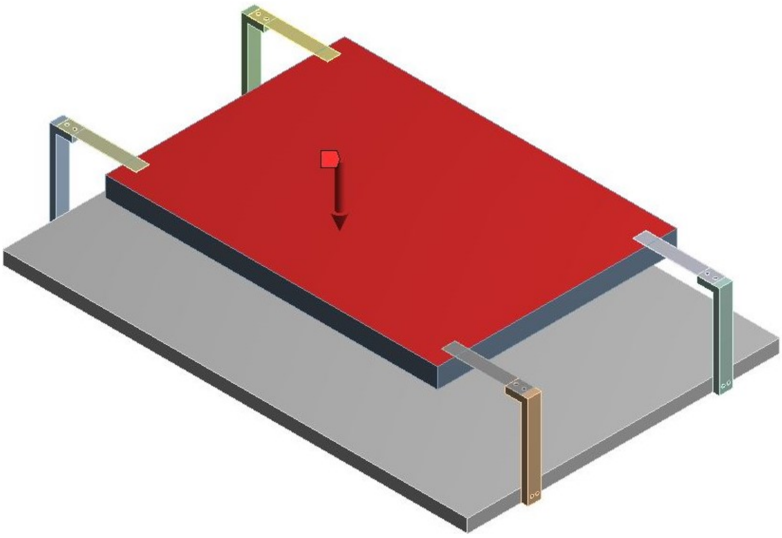

FIGURE 4.15: The geometry applied in ANSYS and the force acting on the top plate

4.6 Operation of the experiment

In this section, the general procedures for the experiment shown in Figures 4.1 to 4.4 is presented. As mentioned in previous sections, the aim of this experiment is to get the FRF data from the rig with various air gap thickness and ambient pressure to identify how the thickness of air gap and pressure could affect on the system damping and resonance. The results of the modal analysis suggest that the whole body mode, for which the top plate moves strictly up and down, is most likely occurs at the frequency around 15 Hz.

4.6.1 Software and control

This experiment was mainly controlled by the SigLab, which is a MATLAB based frequency domain system identification toolbox. The VSS (Virtual Stepped Sine) method has been used, as aiming to get very precise results within a narrow range of frequency.

In order to achieve constant displacement amplitude of the upper plate at a certain frequency, the 'control level channel' on the VSS was set for the accelerometer output. The accelerometer was chosen PCB 355B04 with sensitivity of 103.9 $\mathrm{mV/(m/s^2)}$. The reason to choose this sensitive accelerometer was that since the air gap thickness was thin (0.5 mm minimum), the amplitude of plate vibration had to be very small in order to avoid any contact between two plates. Therefore according to this sensitivity, the 'control level voltage' was set as 0.05V to limit the maximum top plate displacement in 0.1mm at 12 Hz. As the sensor mass was approximately 12g, in order to verify the influence of such weight to the system, at the beginning, the experiment was repeated with the accelerometer in different positions of the top plate (Point 2, 3 and 4 in the Figure 4.9). As the results for different attempts were almost identical, thus the effect of the accelerometer weight was neglected.

4.6.2 Adjustment of the air gap thickness

Three different air gap thickness were studied in this experiment, which were 0.5 mm, 1 mm and 2 mm. Before adjusting the level of the lower plate, two bolts (Component **6** on Figure 4.1) in the middle of the base block had to be released. Then the four bolts (Component **7** on Figure 4.1) at the corners of the base block were adjusted, until the base block was paralleled and has required distance with the upper plate. Then, the two bolts that released at the beginning were fastened firmly. The gap thickness was measured by feeler gauge on every edge to ensure that the two plates are parallel within the required distance.

4.6.3 Adjustment of the pressure in the chamber

The pressure inside of the vacuum chamber can be reduced down to 6 kPa from the ambient atmospheric pressure. The air inside the chamber was sucked by the vacuum pump (Edwards RV8) via a one-way valve. During this experiment, five different pressures were used which were 101 kPa (ambient pressure), 61 kPa, 41 kPa, 21 kPa and 6 kPa. Because the pressure gauge in the experiment is scaled from 0 to -1 bar, from ambient pressure to the vacuum. Therefore, in this thesis, the unit of pressure will be replaced by the unit of "bar" relative to the ambient pressure. Hence the pressures applied in this experiment corresponded to 0 bar(normal pressure), -0.4bar, -0.6bar, -0.8bar and -0.95bar (or Vacuum Pressure).

To minimise the effect of noise from the vacuum pump, it had to be turned off during the test. The chamber was sealed and in a very low pressure, it would take more than 10 minutes for the pressure to increase from -0.95 bar to -0.8 bar. The vacuum reduced more rapidly when the pressure in the chamber was set to a higher value, e.g. -0.4 bar. Therefore, the test would be was occasionally paused and the pump was turned on to maintain the set pressure.

4.7 Results

The results of this experiment are shown in Figure 4.16. The inertance FRF data ($I(\omega)$) that obtained by acceleration/force can be directly output from the rig. In order to make a comparison of the results from both analytical and FE methods, the FRF results are uniformly shown in mobility ($Y(\omega) = I(\omega)/i\omega$). The results show that the gap thickness is the main factor that changes the damping of the plate. It can be observed that there is a peak which represents the whole body mode of this air film system at every pressure for both $1mm$ and $2mm$ gap thickness. However, for the 0.5 mm gap thickness, the peak nearly disappears from the FRF curves. The resonance of the system might still occur but with a very low level due to a large damping ratio of the air layer. There is a peak at about $13Hz$, which was caused by a resonance of the whole system including the chamber and shaker.

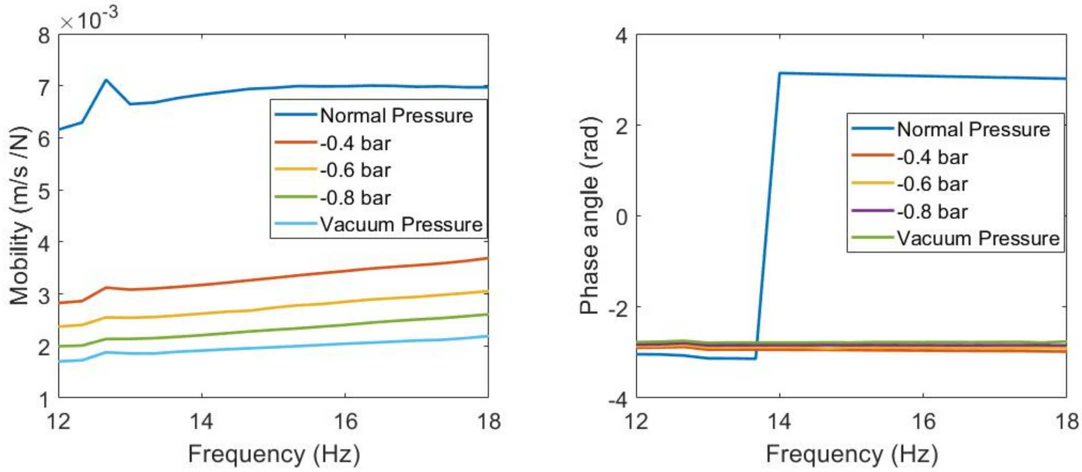

(A) 0.5mm FRF mobility

Phase of 0.5mm FRF mobility

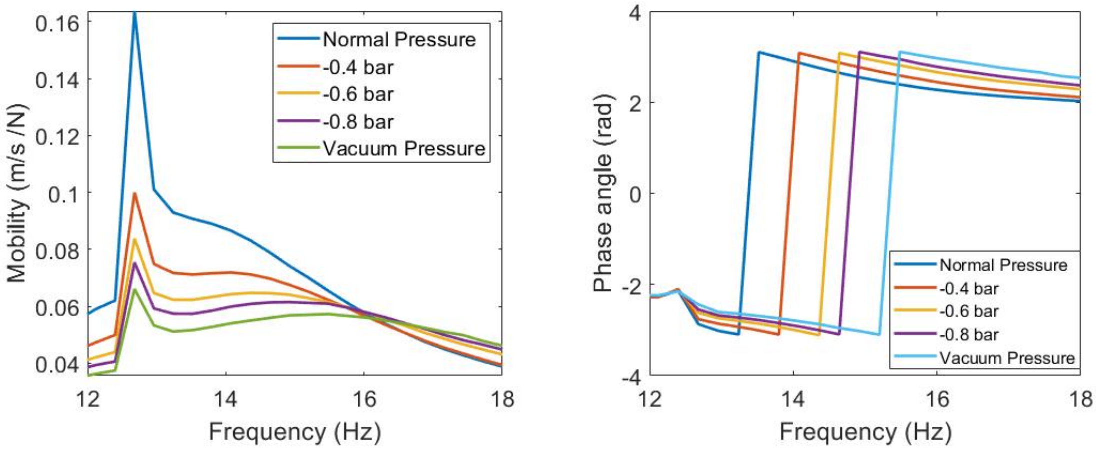

(B) 1mm FRF mobility

Phase of 1mm FRF mobility

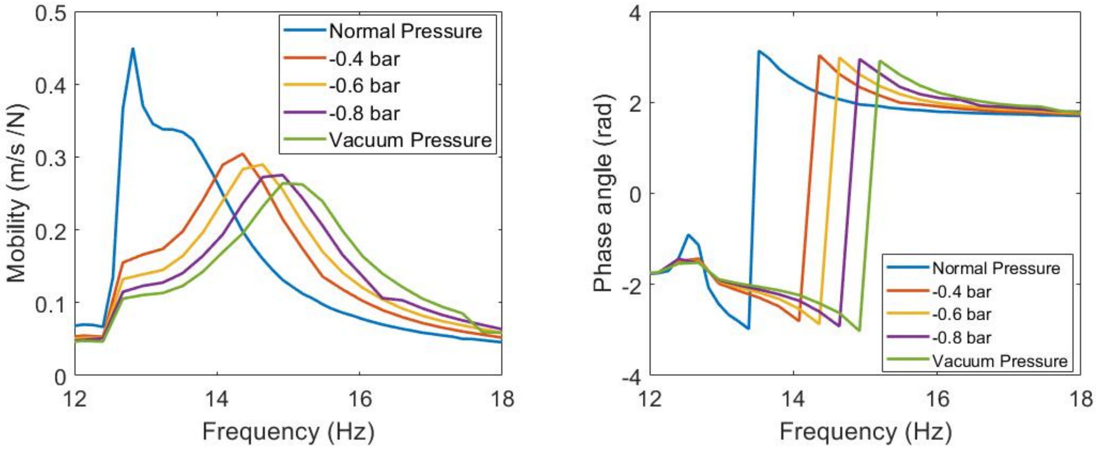

(C) 2mm FRF mobility

Phase of 2mm FRF mobility

FIGURE 4.16: Mobility FRF for various gap thickness A: 0.5mm; B: 1mm and C: 2mm, under different pressures and their corresponding phase angle

Additionally, the 8mm and 10mm thick air gap were tested under the normal pressure, as shown in the figures below.

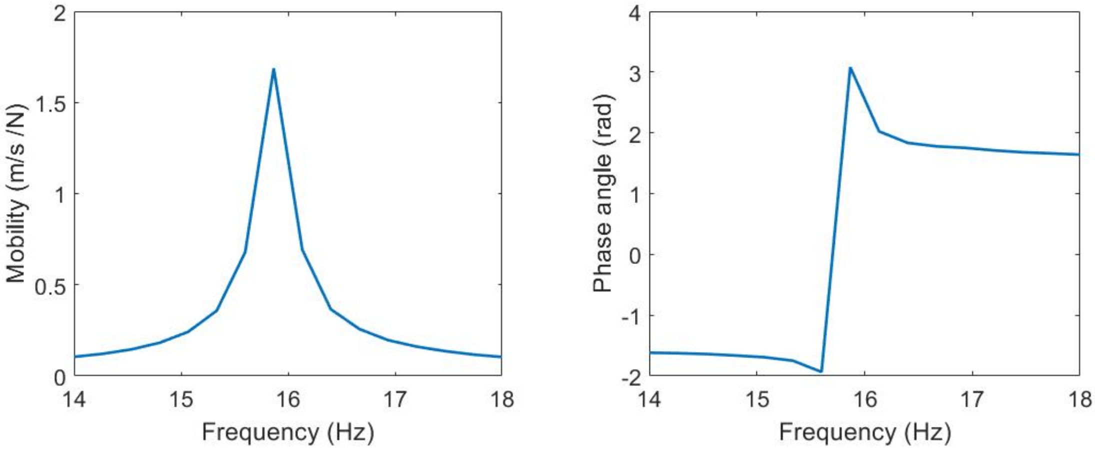

(A) 8mm FRF mobility

Phase of 8mm FRF mobility

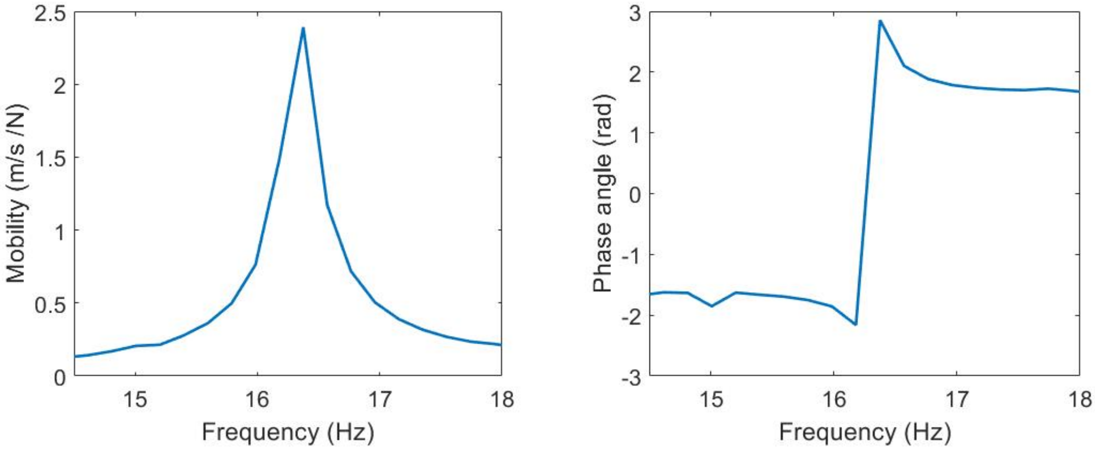

(B) 10mm FRF mobility

Phase of 10mm FRF mobility

FIGURE 4.17: Mobility FRF for gap thickness A: 8mm and B: 10mm under normal pressures and their corresponding phase angle

The resonance frequency increases with the reduced air pressure because the inertia effect of the air in the gap reduces with lower pressure and the bulk modulus of the air decreased. The resonance frequency and damping ratio for each FRF curve were calculated by the Nyquist plot and summarised in the table below. All the Nyquist circle fits for those FRFs are included in the Appendix A.

It can be seen from the Figure A.6 that the circle cannot be fitted for the 1mm-normal-pressure FRF curve, due to the influence of the nearby system resonance, but the resonant frequency that can be estimated from the FRF curve is around 13.24 Hz. For 2mm-normal-pressure FRF curve, according to Figure A.11, the circle is not fitted well, therefore, the damping and the resonant frequency are approx values. According to the Table 4.1, the resonant frequency for $1mm$ and $2mm$ at same pressure are near same. This means that beyond this air gap thickness the effect of mass and stiffness of air in the gap is relatively constant.

Pressure	Resonant Frequency (Hz)	Damping Ratio
	1mm Air gap thickness	
1 atm	13.24 *	-
- 0.4 bar	14.22	0.183
- 0.6 bar	14.76	0.207
- 0.8 bar	15.26	0.202
- 0.95 bar	15.29	0.240
	2mm Air gap thickness	
1 atm	13.52 *	0.0461 *
- 0.4 bar	14.36	0.044
- 0.6 bar	14.64	0.047
- 0.8 bar	14.92	0.048
- 0.95 bar	15.06	0.051
	8mm Air gap thickness	
1 atm	15.85	0.007
	10mm Air gap thickness	
1 atm	16.33	0.007

Note: * - approx value.

TABLE 4.1: Resonant frequency and damping ratio for various gap thickness under various pressures

4.8 Comparison with the low reduced frequency method

Continue with the Equation 3.15, as the forces acting on the system are composed of the force from the air gap, the force from the excitation and the force from the springs, which can be expressed as [26]:

$$\overline{F}_{gap} = l_x l_y p_0 F_{gap} e^{i\omega t}; \quad \overline{F}_{ex} = l_x l_y p_0 F_{ex} e^{i\omega t}; \quad \overline{F}_{springs} = \kappa h_0 h e^{i\omega t}. \tag{4.1}$$

Then the equation of motion of the top plate can be written as:

$$-\omega^2 m h_0 h = l_x l_y p_0 (F_{ex} + F_{gap}) - \kappa h_0 h. \tag{4.2}$$

Therefore the excitation force can be obtained as:

$$F_{ex} = -\frac{\omega^2 m h_0 h}{l_x l_y p_0} - F_{gap} + \frac{\kappa h_0 h}{l_x l_y p_0}. \tag{4.3}$$

The receptance FRF function $H(\omega)$ under harmonic signals is:

$$\begin{aligned} H(\omega) &= \frac{h_0 h}{l_x l_y p_0 F_{ex}} \\ &= \big[-\omega^2 m - \frac{l_x l_y p_0}{h_0} F_{gap} + \kappa \big]^{-1}. \end{aligned} \tag{4.4}$$

Then the mobility FRF function is:

$$\begin{aligned} Y(\omega) &= i\omega H(\omega) \\ &= i\omega \big[-\omega^2 m - \frac{l_x l_y p_0}{h_0} F_{gap} + \kappa \big]^{-1}. \end{aligned} \tag{4.5}$$

We apply the low reduced frequency model to fit the experimental setup, where the mass of top plate: $m = 0.32kg$, stiffness of spring: $\kappa = 4260N/m$ and displacement of top plate: $h = h_0/100$. Then, according to the Equation 4.5, the mobility FRF for various air gap thickness can be plotted as Figure 4.18.

4.8.1 Atmosphere pressure

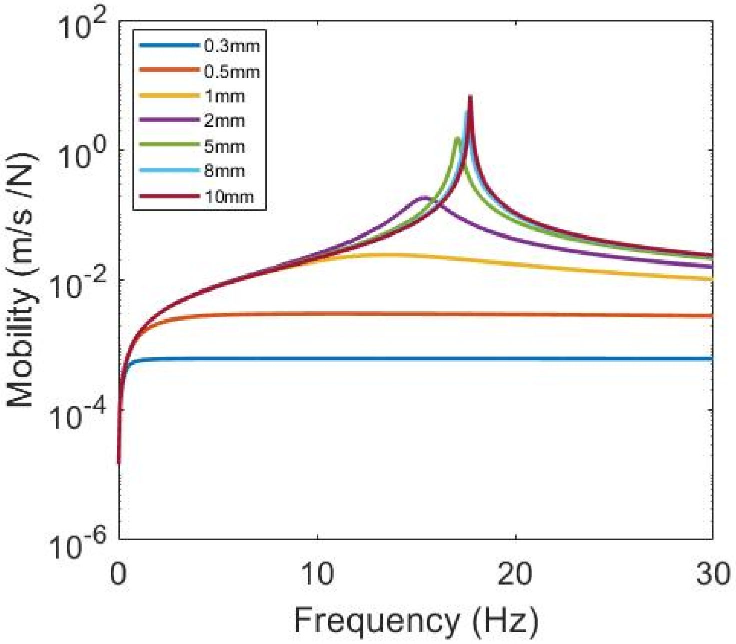

(A) FRF mobility

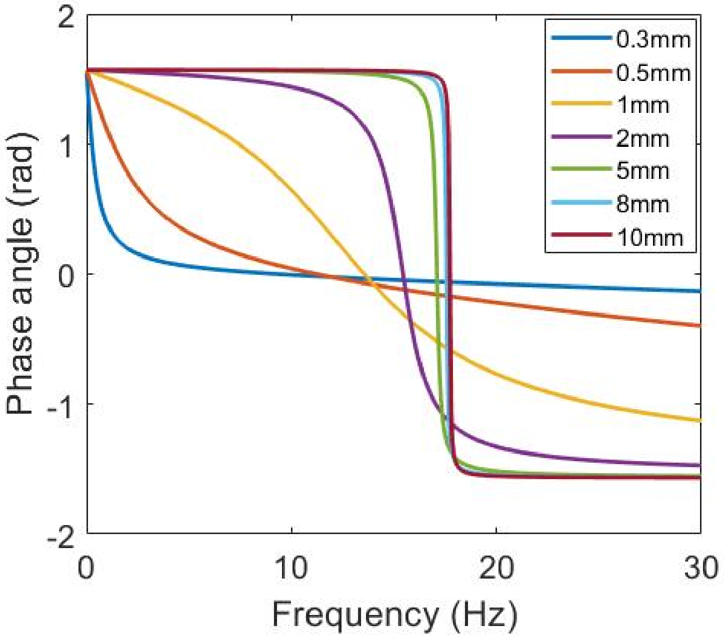

(B) phase

FIGURE 4.18: The plate mobility FRF for various air gap thickness

It can be observed from this figure that the resonance for 0.3mm and 0.5mm air gap disappeared due to the high damping of the system. This can be found from the experimental results as well. The damping ratio and the resonant frequency for the thickness with obvious resonance were fitted with the Nyquist plot, which are shown in Appendix A. The table 4.2 summarises the resonant frequency and the damping ratio of the analytical results.

Gap thickness	Resonant Frequency (Hz)		Damping Ratio	
	Analytical	Experimental	Analytical	Experimental
1mm	13.51	13.24 *	0.410	-
2mm	15.43	13.52 *	0.062	0.046 *
5mm	17.1	-	0.008	-
8mm	17.57	15.85	0.003	0.007
10mm	17.72	16.33	0.002	0.007

Note: * - approx value.

TABLE 4.2: Comparison of Resonant frequency and damping ratio under normal pressures

As shown in this table, due to the error and the coincidence of a system resonance in the experiment, the results from both methods cannot fit well. However, both methods indicate that the resonant frequency increases and the system damping ratio decrease with larger air gap thickness. Figures in Fig 4.19 show the relationships of the gap thickness to the system resonance and the damping ratio respectively, as the air gap thickness increases, both resonant frequency and damping ratio do not change significantly for the air gap thicker than 4 mm.

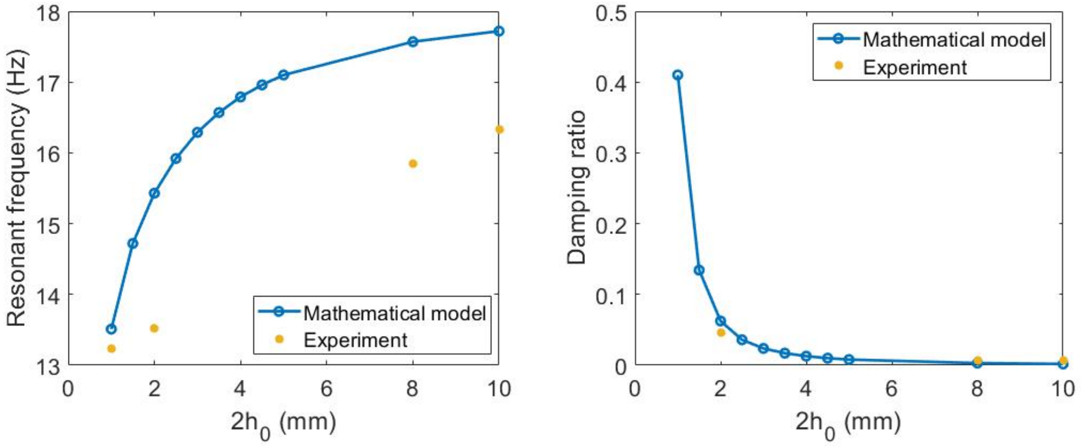

(A) Resonant frequency (B) Damping ratio

FIGURE 4.19: Comparison of mathematical model and experiment

4.8.2 Reduced air pressure

The resonant frequency and damping ratio for the 1mm and 2mm gap are shown in Figure 4.20 and 4.21, respectively. The corresponding resonant frequency and damping ratio were calculated by the Nyquist plot and they are included in Appendix A as well. The numerical values are summarised and compared with the experiment results in Table 4.3.

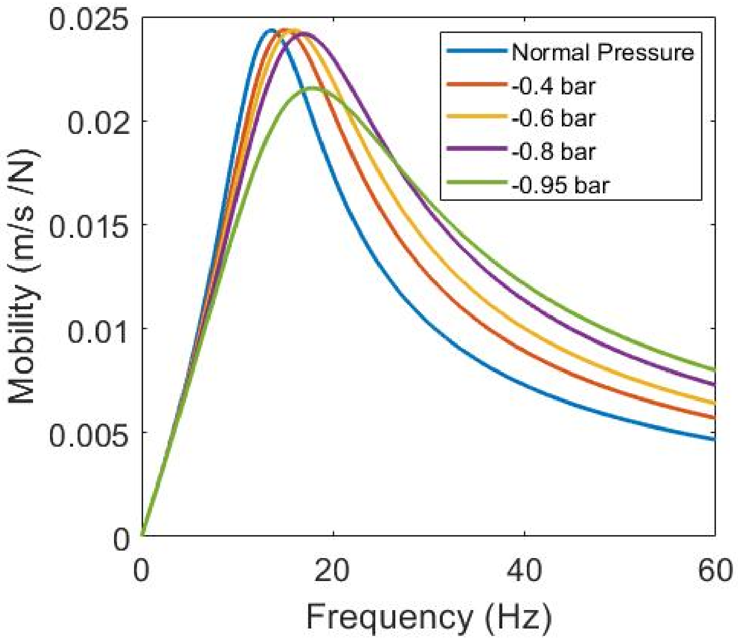

(A) FRF mobility

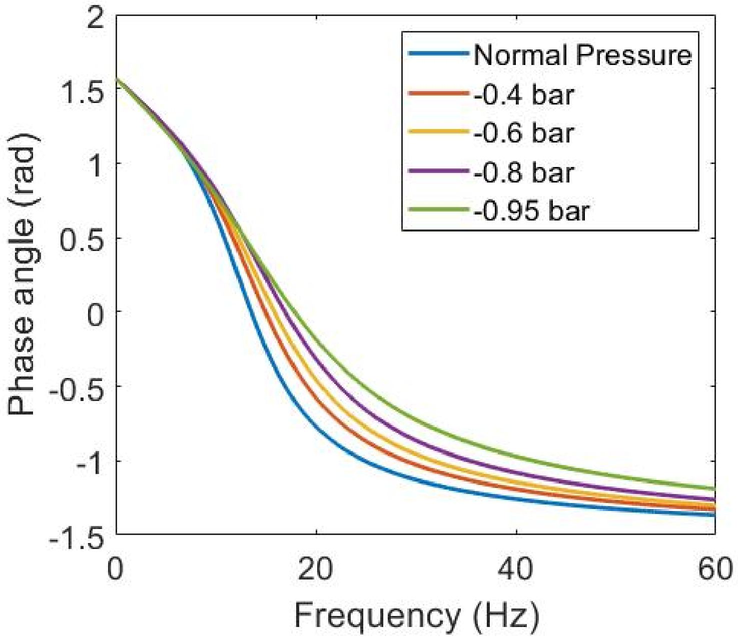

(B) phase

FIGURE 4.20: The plate mobility FRF for 1mm air gap thickness under various pressure

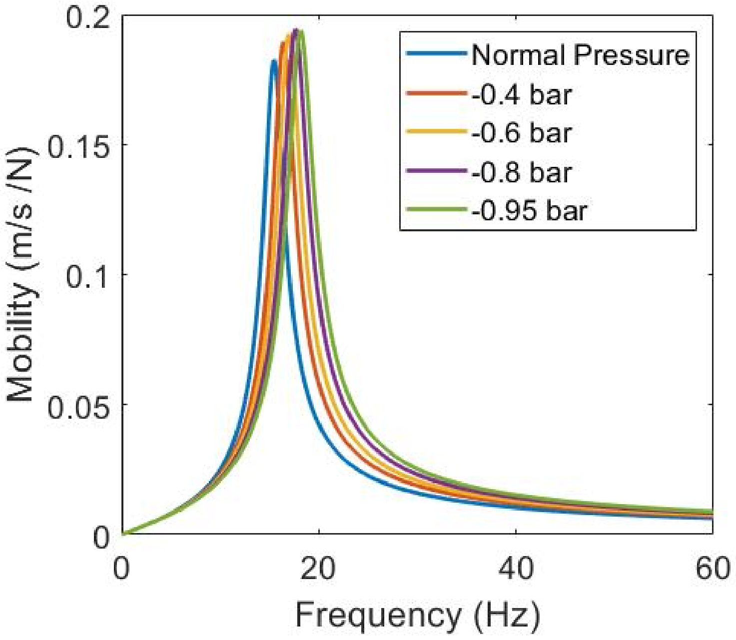

(A) FRF mobility

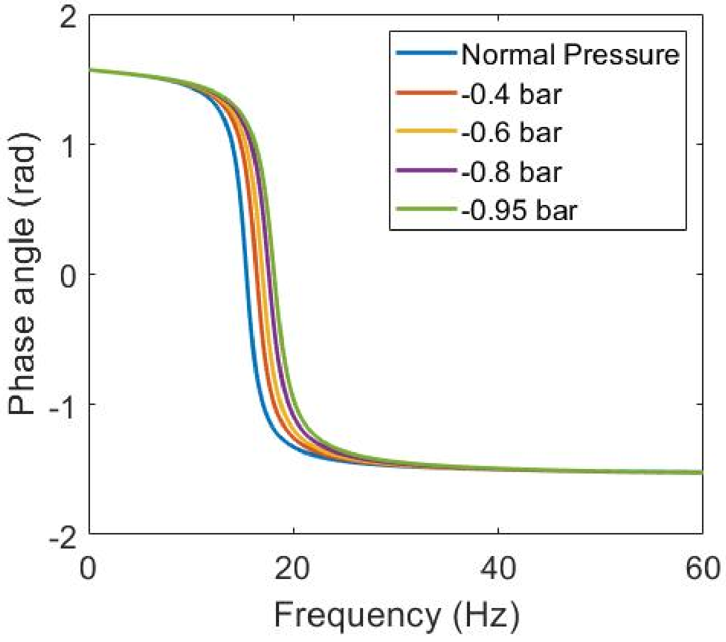

(B) phase

FIGURE 4.21: The plate mobility FRF for 2mm air gap thickness under various pressure

Pressure	Resonant Frequency (Hz)			Damping Ratio		
	Analytical	Experiment	Error(%)	Analytical	Experiment	Error(%)
	1mm Air gap thickness					
1 atm	13.51	13.24*	0.7%	0.410	-	-
- 0.4 bar	14.96	14.22	4.9%	0.452	0.183	59.5%
- 0.6 bar	15.87	14.76	7.0%	0.479	0.207	56.8%
- 0.8 bar	16.95	15.26	10.0%	0.518	0.202	61.0%
- 0.95 bar	17.83	15.29	14.3%	0.613	0.240	60.9%
	2mm Air gap thickness					
1 atm	15.43	13.52*	12.4%	0.062	0.046*	25%
- 0.4 bar	16.41	14.36	12.5%	0.064	0.044	31.2%
- 0.6 bar	16.93	14.64	13.5%	0.065	0.047	27.7%
- 0.8 bar	17.60	14.92	15.2%	0.067	0.048	28.4%
- 0.95 bar	18.13	15.06	16.9%	0.069	0.051	26.1%

Note: * - approx value.

TABLE 4.3: Resonant frequency and damping ratio from the analytical model for 1mm and 2mm gap thickness under various pressures

It can be seen that as the pressure drops, the damping ratio and resonant frequency from both methods have slightly increased. Because the density of the air was decreased in lower pressure, thus the inertial effect was reduced. In a thin gap, where the viscous effect is the main factor of energy dissipation the damping ratio was slightly increased, as the velocity of air caused by the pumping effect in the thin gap is increased with low ambient pressure.

Compared with the experimental data, the resonant frequencies have at most

17% difference. However, the damping ratio predicted from this analytical were much larger than the experimental result. This may be caused by the errors of experiment, which include the extra system damping in the experiment, inaccuracy of the air gap thickness and electrical signal noise. There will be a further comparison and discussion in the next chapter with taking into account the results from the FE model.

4.9 Summary

In this chapter, a series of experiments were carried out to understand the effect of pressure and gap thickness on the resonant frequency and damping ratio of the double-wall-panel system. Experiments were also carried out to understand the effect of supporting springs on the vibration of the tested plate.

It was found that the damping of the vibrating plate is largely influenced by the gap thickness. The pressure can affect damping slightly as the dynamic viscosity does not change by it, which verified with the results from Fox and Whitton [21]. Although the lower plate was made as heavy as possible, the resonance frequency of the structural vibration can still be observed from the FRF data, which coincided with the upper plate resonance with 1 mm air gap thickness. In this experiment, the coincident resonance can be avoided by adding reinforced structure to the chamber or change the mass of the system, however, due to the time constraint, it is not possible to re-run an experiment with a different set-up.

A mathematical model and an FE model will be presented in the next two chapters. The effect of air pressure, viscosity and density will be further discussed in greater detail. The results of these experiments will be used to compared and validated the mathematical model and the FE model.

Chapter 5

Numerical Modelling Work

5.1 Introduction

In this chapter, the Johnson-Champoux-Allard model integrated within COMSOL software is used to predict the influence of the air gap. In order to validate this numerical model, same geometry of air gap with the same pressures in the experiment was used. Additionally, a study is carried out to understand how the dynamic viscosity and density of the fluid in the air gap would influence damping in the plate system with different gap thickness.

The Johnson-Champoux-Allard model (JCA model) is a semi-empirical model with five parameters. it enables to predict the energy dissipations via visco-inertial effect and thermal effects for a large range of porous material with the rigid or limp surface. The JCA model was developed by Champoux and Allard [68], based on the work by Johnson, Koplik and Dashen [69].

In 1987, Johnson, Koplik and Dashen proposed a model to describe the complex density of the poro-acoustic material with a motionless skeleton having arbitrary pore shapes. The expression is:

$$\widetilde{\rho}(\omega) = \frac{\alpha_\infty \rho_0}{\phi}\left[1 + \frac{\sigma_0 \phi}{j\omega\rho_0\alpha_\infty}\sqrt{1 + j\frac{4\alpha_\infty^2 \mu \rho_0 \omega}{\sigma_0^2 \Lambda^2 \phi^2}}\right] \tag{5.1}$$

where: α_∞ the high frequency limit of the tortuosity, ϕ is the open porosity, σ_0 is the static air flow resistivity, μ is the dynamic viscosity of the fluid and Λ is the viscous characteristic length.

In 1991, Champoux and Allard extended the previous work by Johnson et al. by introducing an expression for the dynamic bulk modulus, which is:

$$\widetilde{K}(\omega) = \frac{\gamma P_0/\phi}{\gamma - (\gamma - 1)\left[1 - j\frac{8\lambda}{\Lambda'^2 C_p \rho_0 \omega}\sqrt{1 + j\frac{\Lambda'^2 C_p \rho_0 \omega}{16\lambda}}\right]^{-1}} \tag{5.2}$$

where: γ is ratio of specific heats, P_0 is the ambit pressure, λ is the thermal conductivity, and Λ' is the thermal characteristic length.

5.2 Parametric study

As mentioned in the previous section, the JCA model is a five parameter semi-empirical model, thus those parameters need to be defined before running the simulation.

5.2.1 Porosity

The porosity ϕ (in COMSOL $'\epsilon_p'$ is used to denote this parameter), is the ratio of the fluid volume that occupied by the open pores to the total volume of porous material. As Figure 5.1 shows, the volume of open porosity is only accounting for the network for connected pores. The porosity is normally measured through the pressure difference in an enclosed chamber with enforced volume change [70, 71]. However, the porosity of the air gap studied in this work is 1.

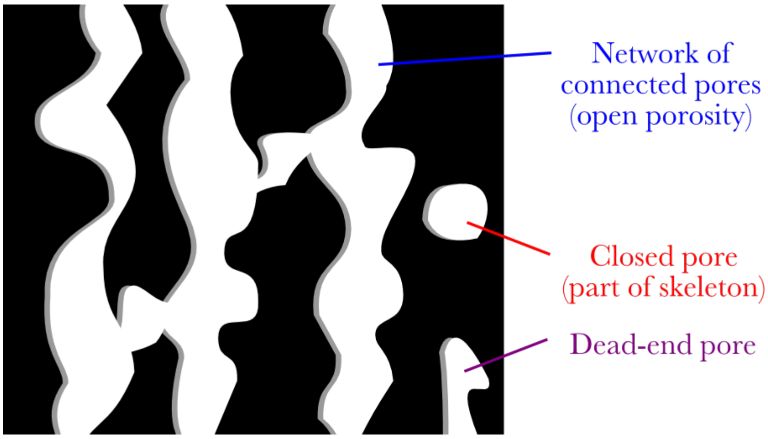

FIGURE 5.1: The open porosity [1]

5.2.2 Static air flow resistivity

The static air flow resistivity σ_0 with the unit of $Pa \cdot s/m^2$, (in COMSOL $'R_f'$ is used to denote is parameter) is to describe the acoustic behaviour of the porous material, and defined as [72]:

$$\sigma_0 = \frac{4\mu k_0}{r_h^2} \tag{5.3}$$

---

[1] Image takes from website: http://apmr.matelys.com/Parameters/OpenPorosity.html

where, k_0 is constant for pore shapes and r_h is the hydraulic radius for circular pores. In terms of the air film slit in this project, $k_0 = 3$ and $r_h = 2h_0$. Hence the resistivity can be re-written as:

$$\sigma_0 = \frac{3\mu}{h_0^2} \tag{5.4}$$

5.2.3 Tortuosity

The high frequency limit of the dynamic tortuosity α_∞ (τ_∞ in COMSOL) is normally simplified as tortuosity. This parameter describes the visco-inertial effect at high frequency, and being defined by Johnson, Koplik and Dashen [69]:

$$\alpha_\infty = \frac{\frac{1}{V}\int_V v^2 dV}{\left(\frac{1}{V}\int_V \vec{v} dV\right)^2} \tag{5.5}$$

where, v is the velocity of the particle at high frequency, and V is the homogenization volume of fluid in the porous material. The value of tortuosity is usually in the between from 1 and 3 [73]. Since there are only two paralleled plates with a small gap in this project, the air inside of the slit will only move along the surface of the plate, therefore $\alpha_\infty = 1$.

5.2.4 Viscous characteristic length

The viscous characteristic length Λ (L_v in COMSOL) is the parameter that describes the characteristic pore scale and it relates to strength of the viscous effect in the porous medium. It is defined as:

$$\Lambda = 2\frac{\int_V v_{inv}^2 dV}{\int_A v_{inv}^2 dA} \tag{5.6}$$

where v_{inv} is the velocity of fluid that is considered as inviscid, and A is the surface area of fluid-solid interface in the pore.

Generally, for most porous materials, the stronger viscous effects occurs at the narrowest part of a pore, as Figure 5.2 shows.

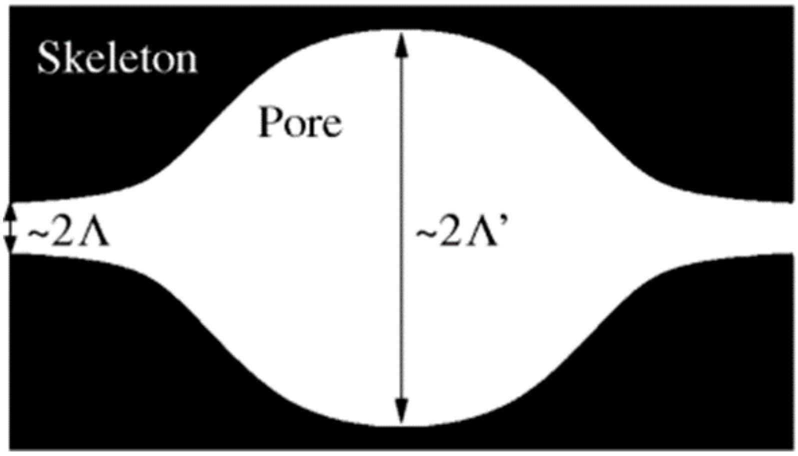

FIGURE 5.2: Figure of showing viscous and thermal characteristic length[2]

5.2.5 Thermal characteristic length

The thermal characteristic length Λ' (L_{th} in COMSOL) is a parameter that describes the pore scales characteristic to thermal effects in the porous medium. On the contrary to the viscous effects, thermal effects normally occur at the widest part of a pore, as Figure 5.2 shows. However, because of the geometry of this project, both the viscous and thermal characteristic lengths should equal to half air gap thickness. The table below lists the parameters set in the JCA model.

---

[2] Image takes from website: http://apmr.matelys.com/Parameters/ViscousCharacteristicLength.html

Symbols	Description	Value
ϵ_p	Porosity	1
R_f	Flow Resistivity	$\frac{3\mu}{h_0^2}$
L_v	Viscous Characteristic Length	$2h_0$
L_{th}	Thermal Characteristic Length	$2h_0$
τ_∞	Tortuosity factor	1
	Porous matrix approximation	Rigid

TABLE 5.1: Parameters setting in JCA model

5.3 COMSOL setting

5.3.1 Geometry

In the JCA model in COMSOL the geometry was set to exactly same as what was set in the low reduced frequency model as described in the previous chapter (Fig 3.1), i.e. the air slit is 250 mm by 180 mm with various thickness. The geometry in COMSOL FE model is consisted by three parts: top plate, base plate and the air film, as Figure 5.3 shows. The prescribed displacement ($h = 2h_0/100$) was applied uniformly to the top plate, thus the top plate will be moved as a rigid surface without any resonance and mass for itself. The material for air film was set as air in COMSOL material library, which includes all parameters needed in the JCA model.

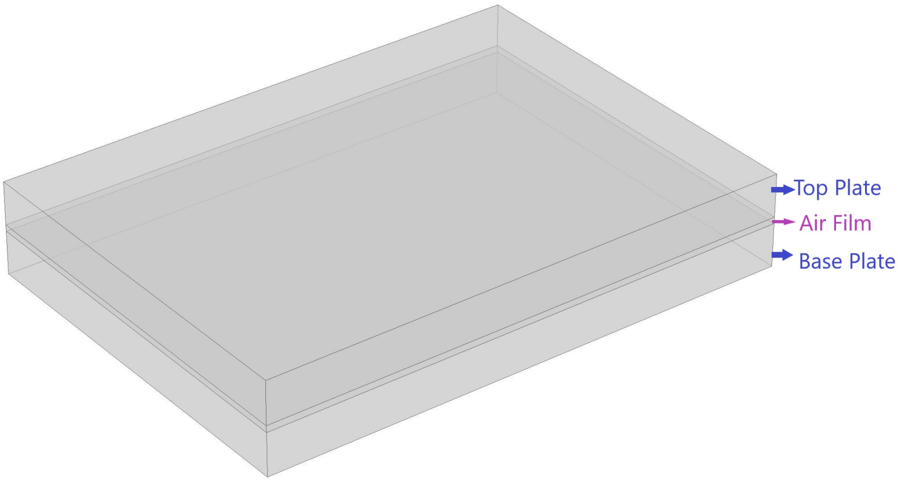

FIGURE 5.3: The geometry of JCA model

5.3.2 Mesh

In order to improve the speed of simulation, a study of the effect of mesh density was carried out to identify whether this model was sensitive to the mesh size. Figure 5.4 and 5.5 demonstrate coarser and fine meshes across the layer thickness, used in the numerical simulation, respectively. The fine mesh had five layers for the air slit along with its thickness with 400 hexahedral elements in total, whereas, the coarser mesh only had one layer with only 80 hexahedral elements. When running the same simulation for these two different sizes of mesh, the coarser one saves about half time of running for the fine mesh. The comparison of simulations for these two meshes suggests that the mesh size has a marginal effect on the accuracy of the acoustic pressure predicted in the air gap and on the associated plate displacement. Therefore, for the further simulations, the coarser mesh is adequate for the JCA model and it will be applied to improve the efficiency.

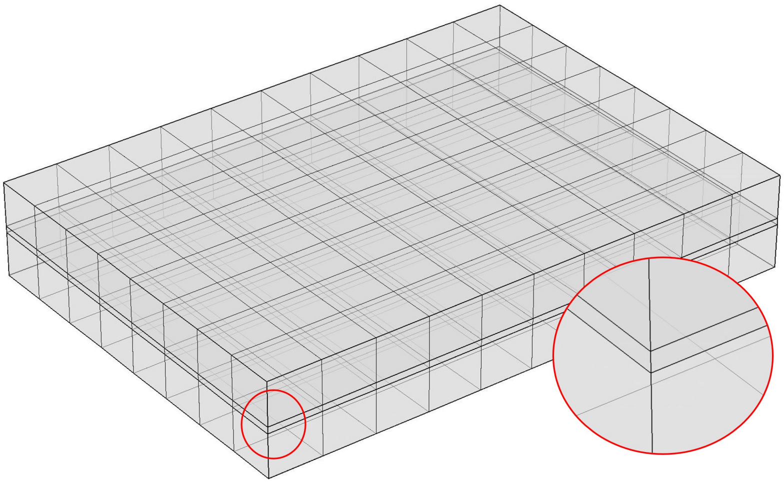

FIGURE 5.4: Coarser meshes

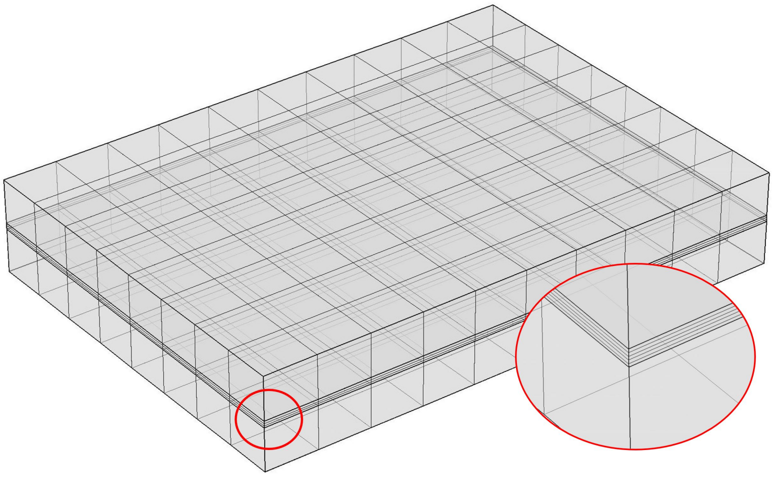

FIGURE 5.5: Fine meshes

5.3.3 Other Settings

The sound soft boundary needs to be set before the JCA model for the four edges of the air film to make the air in the slit connected with outside, as marked green in Figure 5.6. Compared with the other option, 'sound hard boundary', the sound soft boundary makes the sound wave goes through, whereas the other one can only reflect the sound wave.

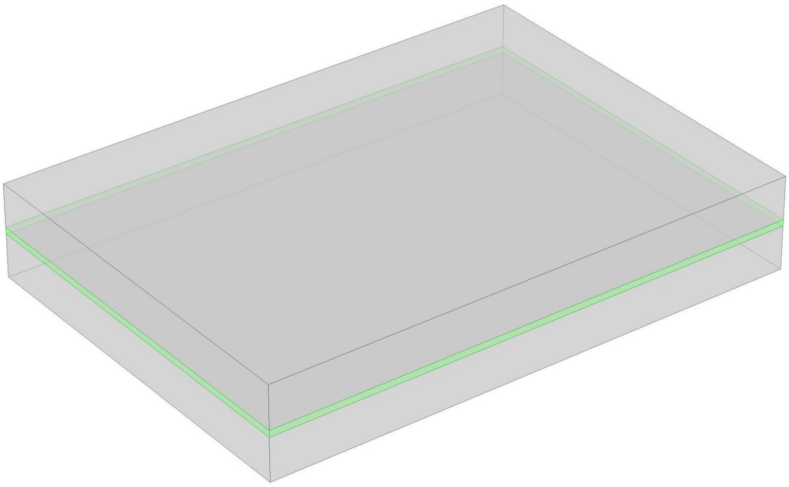

FIGURE 5.6: The soft boundaries

5.4 Results

The effect of six different gap thicknesses from 5 to 60 Hz were predicted using the developed COMSOL model. These were 0.1 mm, 0.3 mm, 0.5 mm, 1 mm, 3 mm and 5 mm air gaps. Figure 5.7 shows an example of acoustic pressure distribution within the air gap at 60Hz. It can be observed that the highest pressure occurs at the centre, and the pressure turns to the ambit pressure at the edge, this can also apply to other frequencies.

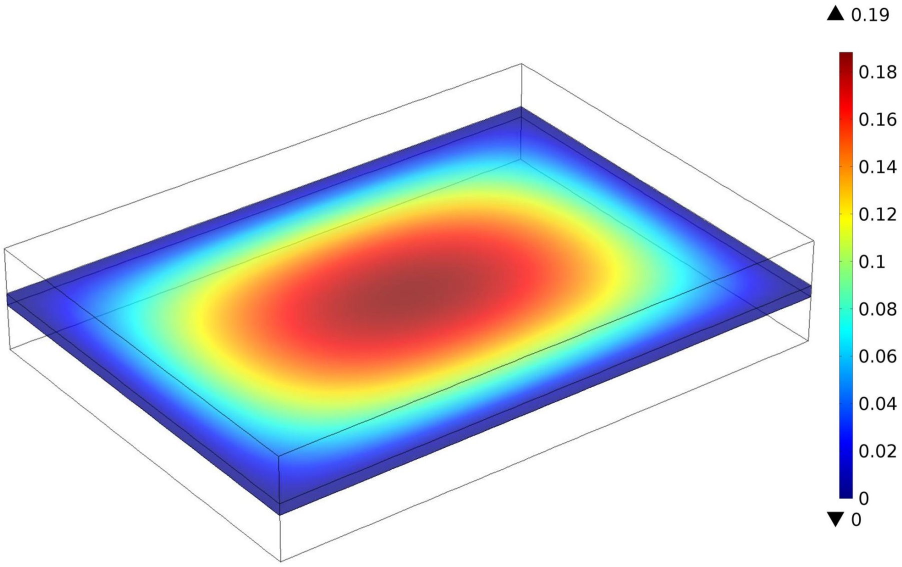

FIGURE 5.7: The acoustic pressure distribution of slit (Pa) at 60Hz

In the JCA model, the result output usually is the total acoustic pressure p_t in the air gap. The force from the air acting on the plate, F_{gap} is the surface integral of p_t, which is:

$$F_{gap} = \int_A p_t dA \tag{5.7}$$

As this force is complex in value, the real part of this force normally indicates the added mass and stiffness effect to the upper plate, whereas the imaginary part of this force indicates the energy dissipation from this air in the gap. Since this force is also proportional to the upper plate displacement, the normalised force (F_{gap}/h) therefore was plotted and compared in this chapter.

The results for 0.1 mm gap thickness are shown in Figure 5.8, and for the other gap, thicknesses are shown in Figure 5.9. Same to the results from the low reduced frequency model, it can be observed that the real part of the sound pressure for the 0.1 mm air gap is negative, whereas for the other air gaps it is positive.

This is caused by the domination of the viscous effect when the air gap thickness is completely smaller than the acoustic boundary layer thickness. This change can be also observed from the results for the low reduced frequency model (Figure 3.3 and 3.4).

The imaginary part relates to the energy dissipation of the air gap. From the results, with the same trends from the analytical model and the experiment, it can be clearly observed that the thinner the gap the higher the energy dissipation efficiency in it.

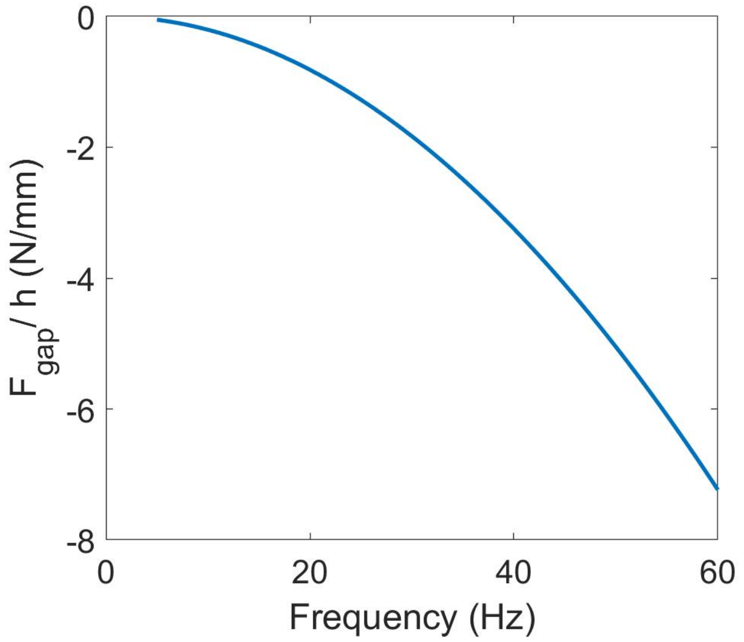

(A) Real Part

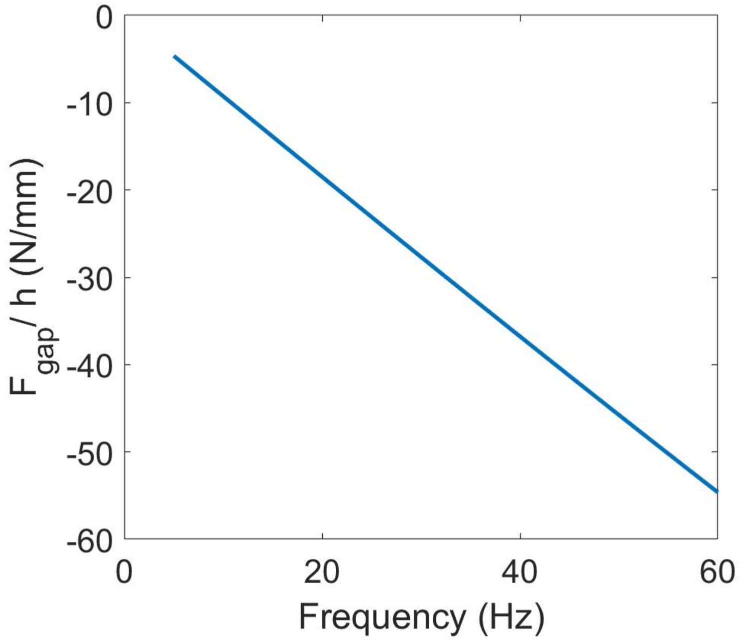

(B) Imaginary Part

FIGURE 5.8: The real (A) and imaginary (B) parts of results (F_{gap}/h) for $2h_0 = 0.1$ mm

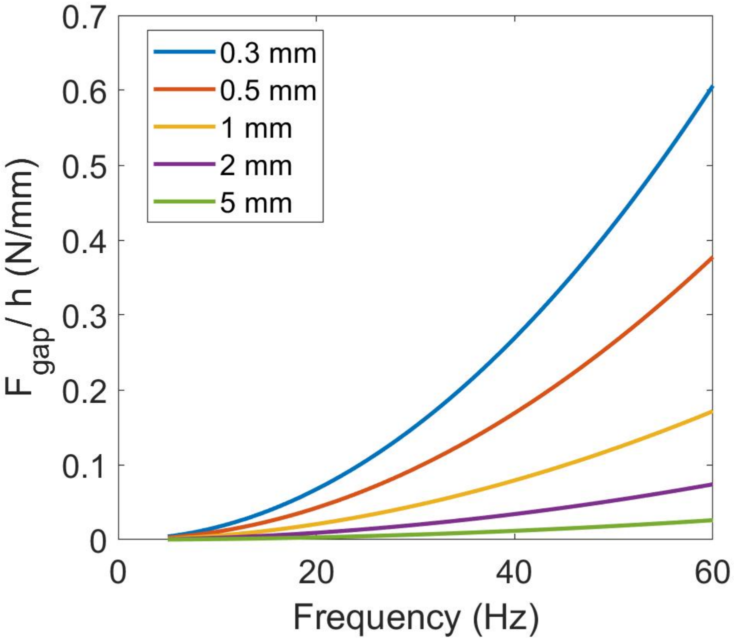

(A) Real Part

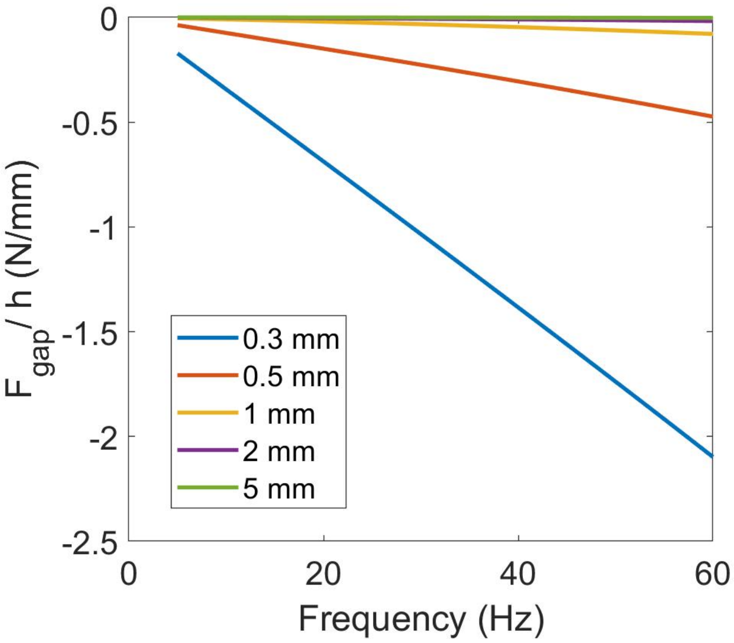

(B) Imaginary Part

FIGURE 5.9: The real (A) and imaginary (B) parts of results (F_{gap}/h) for $2h_0$ = 0.3, 0.5, 1, 2 and 5 mm

By using the equation 4.5 and applying the physical parameters from the experiment, which m = 0.32 kg , and κ = 4260 N/m the mobility FRF response of the upper plate can be obtained. Figure 5.10 shows the mobility response of the F_{gap} applied in experiment model. The results show the same tendency compared with results from both the experiment and the numerical model. For those which gap thicknesses are smaller than $1mm$, the pumping resonance are not visible due to the high damping effect of the air gap. Table 5.2 shows the damping ratio and resonant frequency for $1mm$, $2mm$, $5mm$, $8mm$ and $10mm$ gap thickness. These were calculated by the Nyquist plot and the fitting are shown in Appendix A.

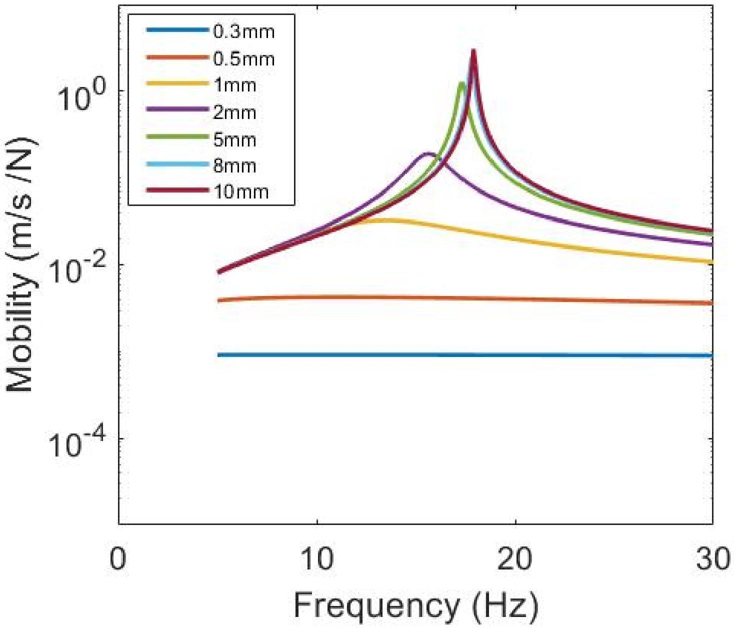

(A) FRF mobility

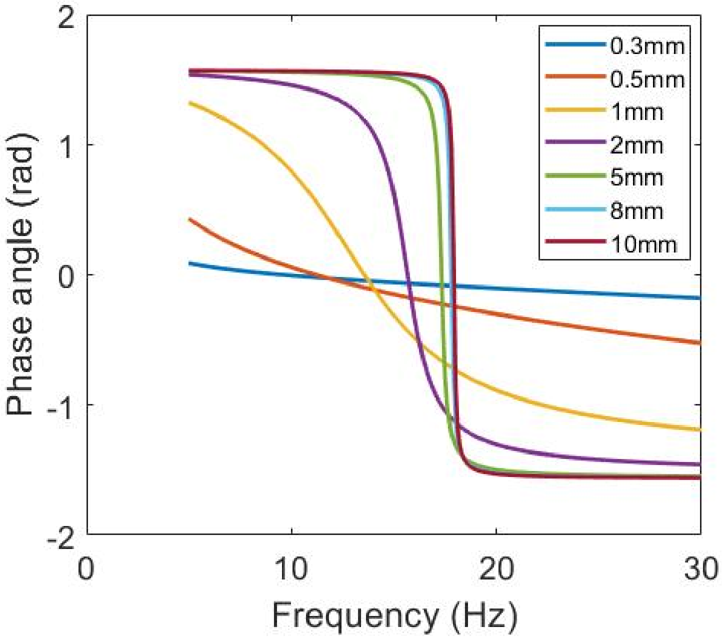

(B) phase

FIGURE 5.10: Mobility FRF for various gap thickness from the FE model

Thickness	Resonant Frequency (Hz)			Damping Ratio		
	FE	Analytical	Exp	FE	Analytical	Exp
1mm	13.47	13.51	13.24 *	0.307	0.410	-
	-	-0.3%	1.7%	-	-33.6%	-
2mm	15.64	15.43	13.52 *	0.062	0.062	0.046 *
	-	1.3%	0.8%	-	0%	15%
5mm	17.32	17.10	-	0.010	0.008	-
	-	1.3%	-	-	20%	-
8mm	17.80	17.57	15.85	0.005	0.003	0.007
	-	1.3%	11.0%	-	40%	-40%
10mm	17.91	17.72	16.33	0.004	0.002	0.007
	-	1.1%	3.2 %	-	50%	-75%

Note: * - approx value.

TABLE 5.2: The Resonant frequency and damping ratio under normal pressures from FE model, the low reduced frequency model and the experiment

This table shows that the pumping mode resonant frequency from the FEM is excellently fit with the results from the low reduced frequency model. The difference between these two methods under 1.5%. However, in term of the damping ratio, the errors were quite large. This may due to not taking into account the air-gap-piston-effect from the low reduced frequency model.

Figure 5.11 and 5.12 show the comparison for the resonant frequency and damping ratio, respectively, from the experiment and mathematical model in previous chapters and the FE model in this chapter. The theoretical and numerical predictions show a similar trend. An excellent agreement showing for FEM and the mathematical model in term of the pumping mode resonant frequency. The agreement between the two models becomes better for larger air gaps, i.e. when the thickness of the air gap becomes much greater than the boundary layer thickness. For 15 Hz excitation, the thickness of the viscous boundary layer is approximately 0.4 mm so that this condition is well satisfied for the air gap with $h_0 > 4$ mm. Although there are only four gap thicknesses that were observed resonance in the experiment, they are showing the same trends with the others. Therefore, this FE model is indeed useful to optimise the design for more complex air gap geometries.

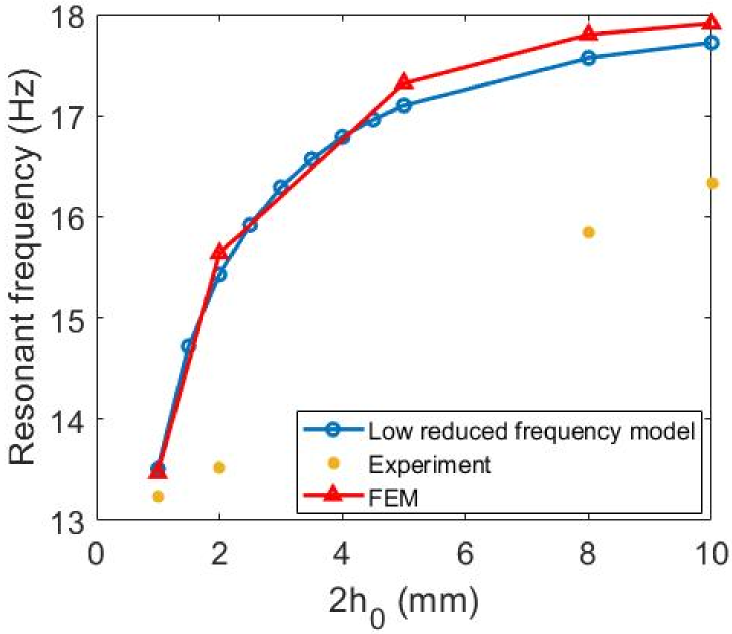

FIGURE 5.11: Resonant frequency against gap thickness from 3 methods

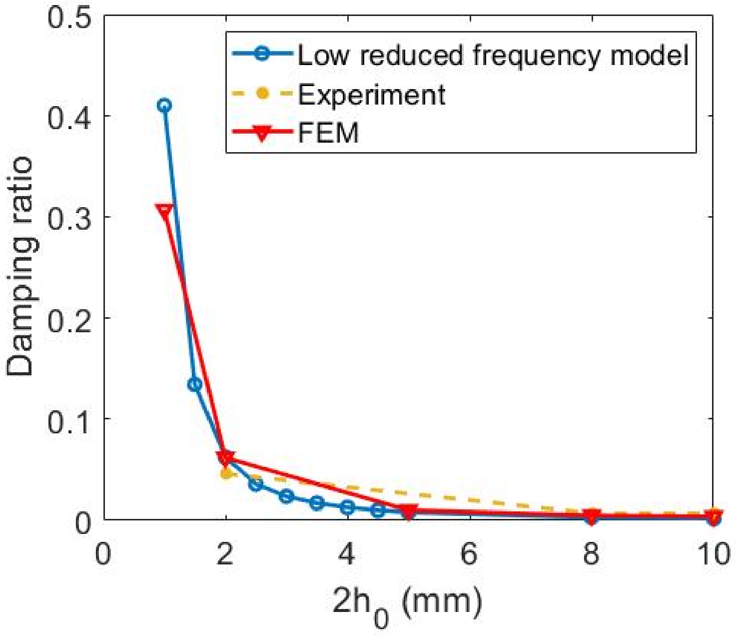

FIGURE 5.12: Damping ratio against gap thickness from 3 methods

5.5 Investigations into the effect of different parameter

There are some further researches to explore how viscosity and mass can affect the air film damper with 0.1 mm, 1 mm and 5 mm thick.

5.5.1 Viscosity

In this section, in order to enhance the viscous effect, the viscosity of air for the JCA model was set to 10 times as its original value. The results are shown in the figures below.

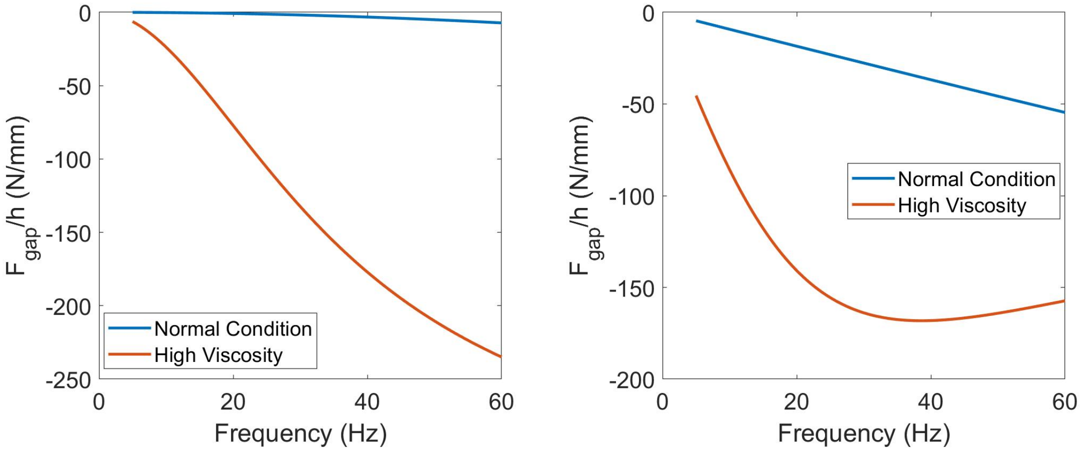

(A) Real Part (B) Imaginary Part

FIGURE 5.13: The effect of ten times higher fluid viscosity on the real (A) and imaginary (B) parts of the force acting on the upper plate in 0.1 mm gap thickness

Figure 5.13 shows the effect of viscosity on the normalised force in the 0.1 mm thick air gap. It can be observed that the viscosity has a huge effect on both the real and imaginary part. The magnitude of normalised force was greatly increased with an increase in the viscosity. However, the maximum value in the imaginary part of the force occurs at about 30 Hz (see Figure 5.13(B)). That is because the air tends to be compressed, which is also called as piston-like behaviour of air, instead of pumping air in and out from the gap.

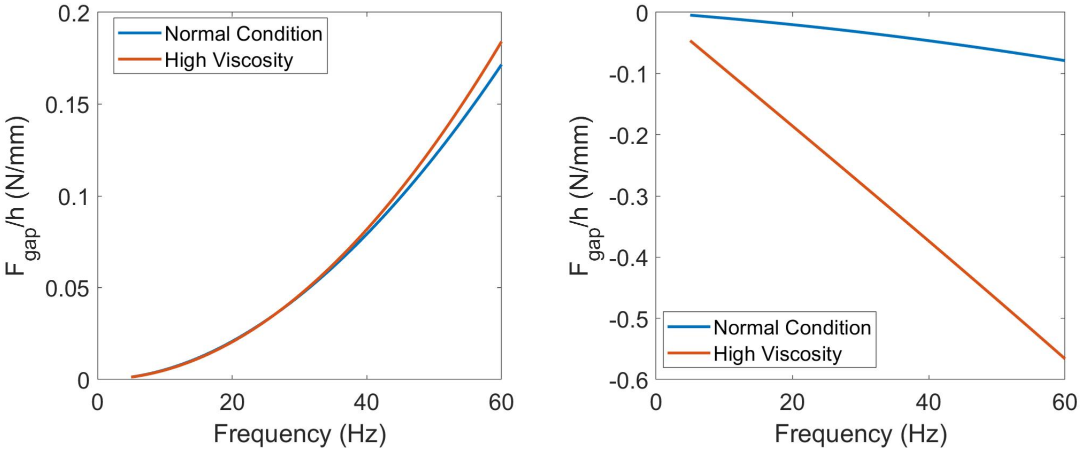

(A) Real Part (B) Imaginary Part

FIGURE 5.14: The effect of ten times higher fluid viscosity on the real (A) and imaginary (B) parts of the force acting on the upper plate in 1 mm gap thickness

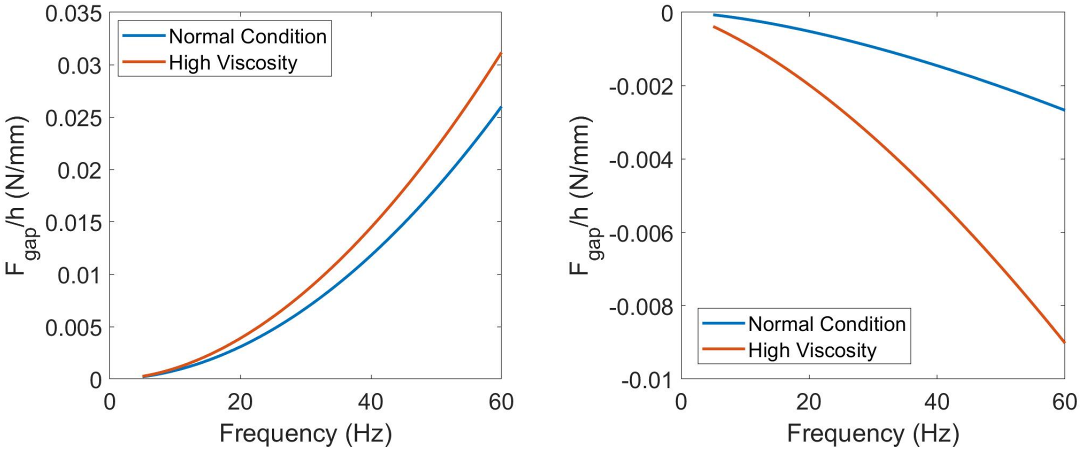

(A) Real Part (B) Imaginary Part

FIGURE 5.15: The effect of ten times higher fluid viscosity on the real (A) and imaginary (B) parts of the force acting on the upper plate in 5 mm gap thickness

Figures 5.14 and 5.15 show the effect of high viscosity on the force acting on the upper plate, in the 1 mm and 5 mm air gaps, respectively. Opposite to the result observed for the 0.1 mm thick air gap, the viscosity seems not to influence the real part much. Because the mass loading effect dominated the real part of the force in these relatively large gap thickness. Whereas, the real part of the forces are indeed increased when the viscosity of fluid increases.

5.5.2 Mass

In this section, in order to enhance the mass effect of the fluid, the density of air for the JCA model was set to 10 times its original value, in order to prove how the mass effect can influence the damping of the upper plate. The results are shown in the figures below.

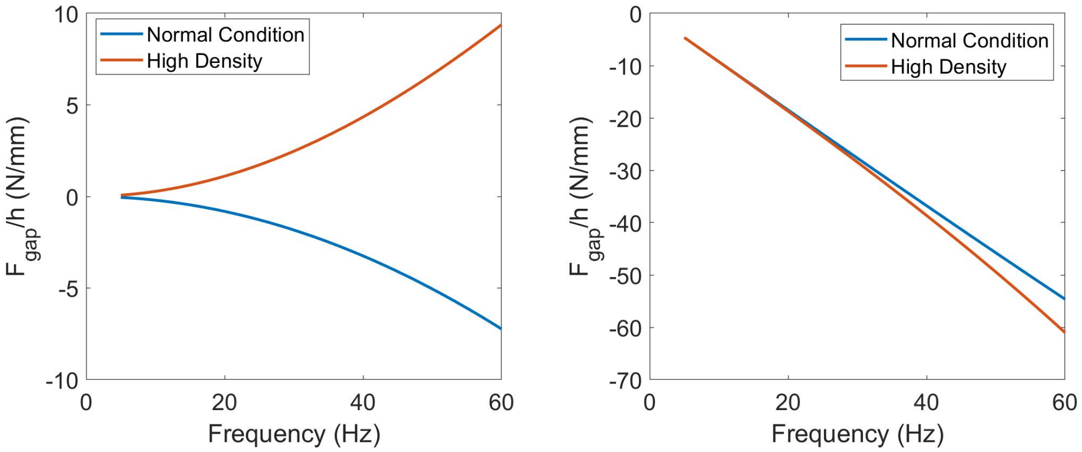

(A) Real Part (B) Imaginary Part

FIGURE 5.16: The effect of ten times higher air density on the real (A) and imaginary (B) parts of the force acting on the upper plate in 0.1 mm gap thickness

Figure 5.16 shows the normalised force acting on the plate with 0.1mm gap thickness filled with fluid with 10 times normal density of air. Since the mass of air was increased 10 times, the mass effect dominates the real part rather than the viscous effect. These can fully explain the prediction at section 5.4 that both the air viscosity and air bulk modulus are acting on the real part of the normalised force but they eliminated each other. However, as shown in Figure 5.16 even the mass of air increased, the imaginary part only has tiny increment.

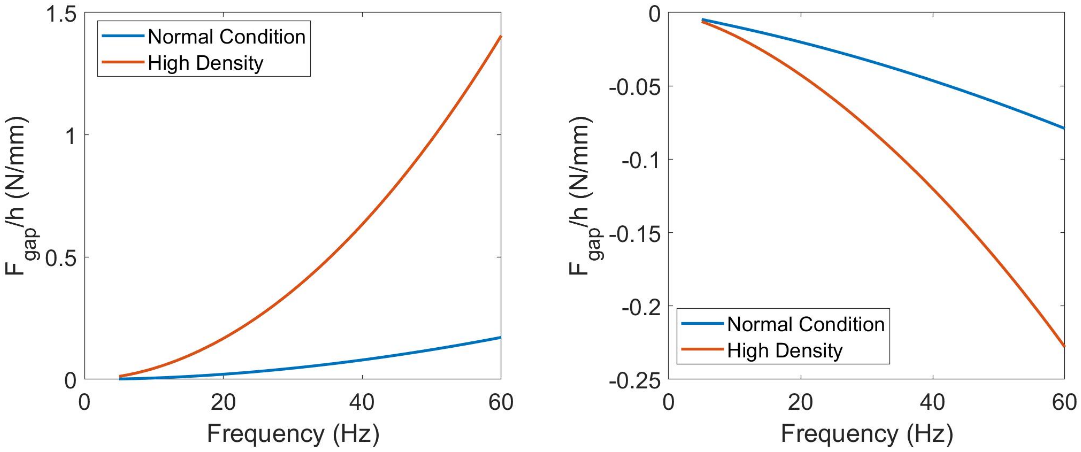

(A) Real Part (B) Imaginary Part

FIGURE 5.17: The effect of ten times higher air density on the real (A) and imaginary (B) parts of the force acting on the upper plate in 1 mm gap thickness

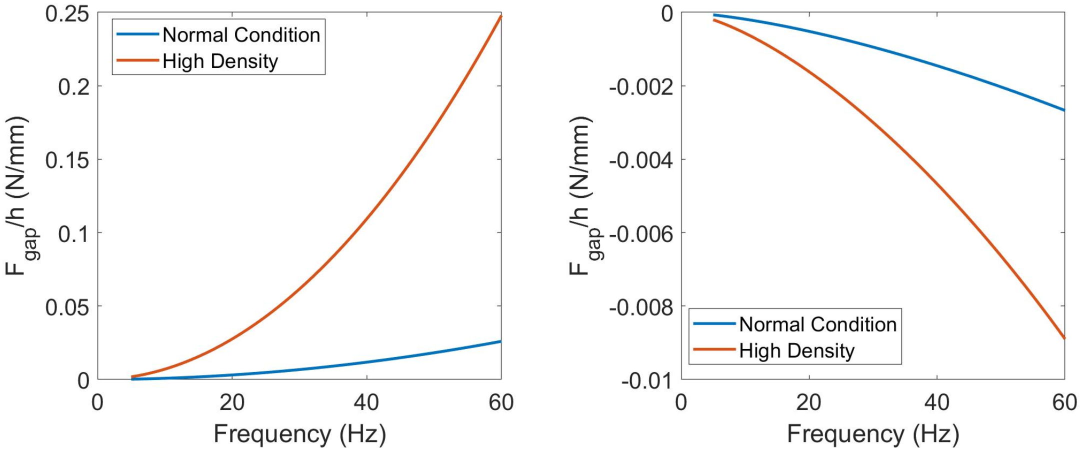

(A) Real Part (B) Imaginary Part

FIGURE 5.18: The effect of ten times higher air density on the real (A) and imaginary (B) parts of the force acting on the upper plate in 5 mm gap thickness

As shown in Figure 5.17 and 5.18, the thicker the air gap, the greater is the increase in the amplitude of the normalised force in the case of the heavier air mass.

5.5.3 Pressure

To study the effect of the static air pressure, the P_A in the COMSOL was set as same pressure values as those used in the experiment: 0 bar, -0.4 bar, -0.6 bar, -0.8 bar and -0.95 bar. Figure 5.19 to 5.22 show the normalised forces acting on the upper plate, with the gap thickness of 0.1 mm, 0.3 mm, 1 mm and 2 mm. For the 0.1 mm gap decrease of pressure, the absolute value of the real part of the force increased. Because 0.1 mm gap thickness is far smaller than the air boundary layer thickness which is 0.4 mm at 15 Hz, hence the viscosity of the air would increase the stiffness of the system slightly. There is an intersection for the pressure -0.8 bar and -0.95 bar in the real part of the force. It can be predicted that in an air gap with a lower pressure, the piston-like behaviour can easily occur at a lower frequency. The absolute value of the imaginary part decreased with pressure drop, as the density of air decreased by lower pressure, and convergence also can be seen from -0.95 bar at about 30 Hz.

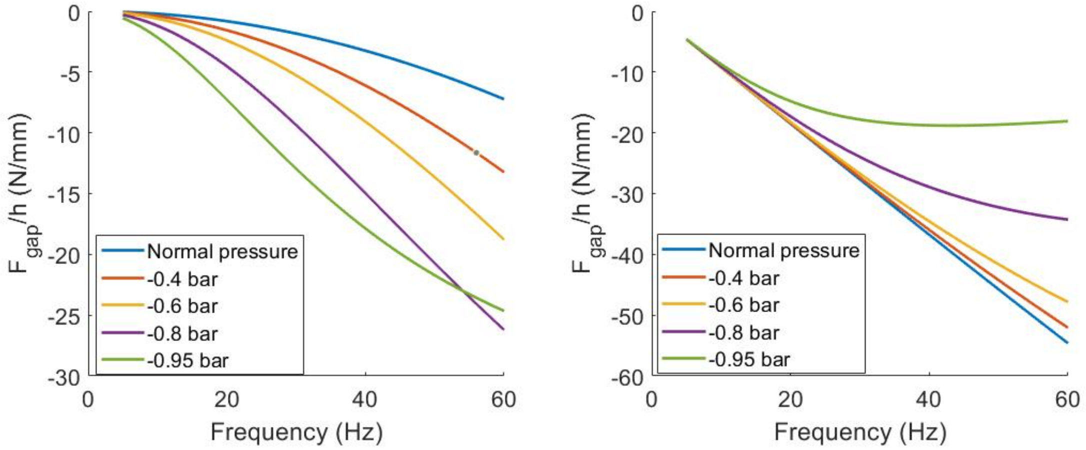

(A) Real Part (B) Imaginary Part

FIGURE 5.19: The pressure effect on the real (A) and imaginary (B) parts of the force acting on the upper plate in 0.1 mm gap thickness

Figure 5.20 shows the results of 0.3*mm* thick air slit under various pressures. The real part of the normalised force tends towards the negative values as the air pressure drops. The imaginary part of the force basically remains the same for different pressures.

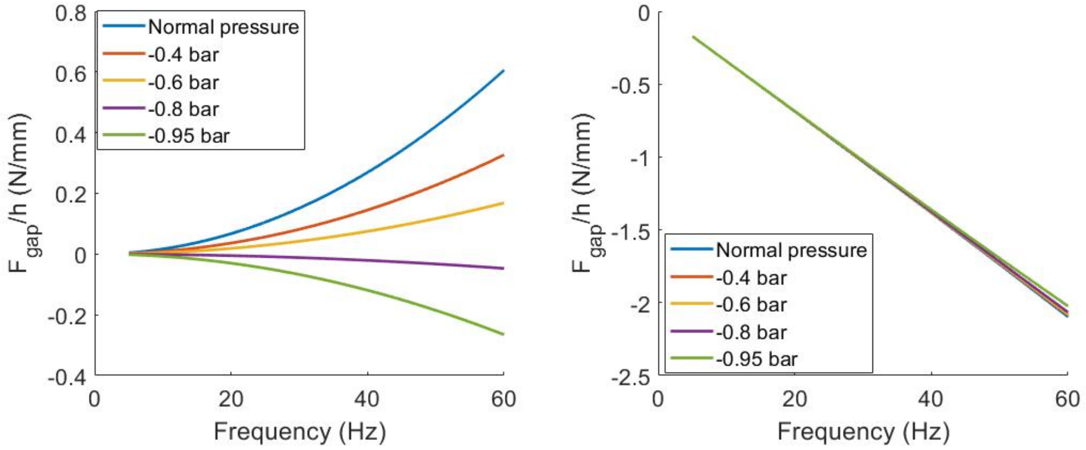

(A) Real Part (B) Imaginary Part

FIGURE 5.20: The pressure effect on the real (A) and imaginary (B) parts of the force acting on the upper plate in 0.3 mm gap thickness

The results for larger air gaps shown in Figures 5.21 and 5.22 have same tendency as the air pressure decreases. The real part of the force tends to zero in vacuum and the absolute value of imaginary part of the force decreases a little at a very low pressure.

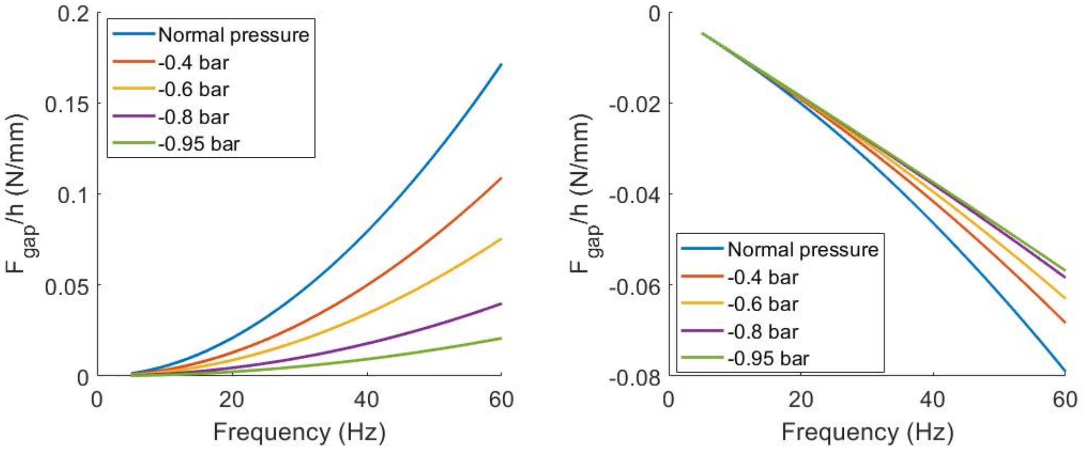

(A) Real Part (B) Imaginary Part

FIGURE 5.21: The pressure effect on the real (A) and imaginary (B) parts of the force acting on the upper plate in 1 mm gap thickness

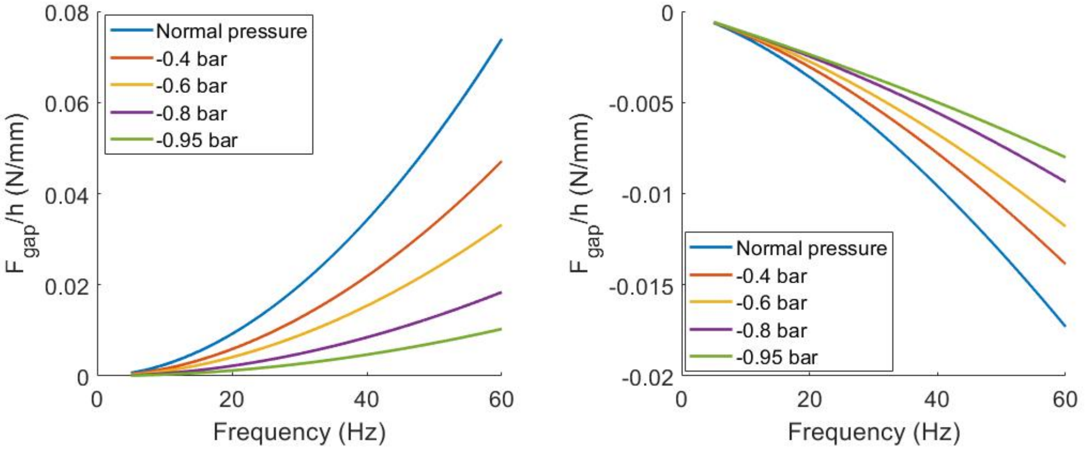

(A) Real Part (B) Imaginary Part

FIGURE 5.22: The pressure effect on the real (A) and imaginary (B) parts of the force acting on the upper plate in 2 mm gap thickness

In order to study the viscosity effect on the plate damping at variable pressure, the viscosity of the air was increased by a factor of 10 times. As observed in Fig 5.23, the behaviour of the real and imaginary parts of the force converges at the lower frequencies. This is because the flow resistivity of the air gap increases proportionally to the air viscosity reducing the propensity of air to move under the plate excitation.

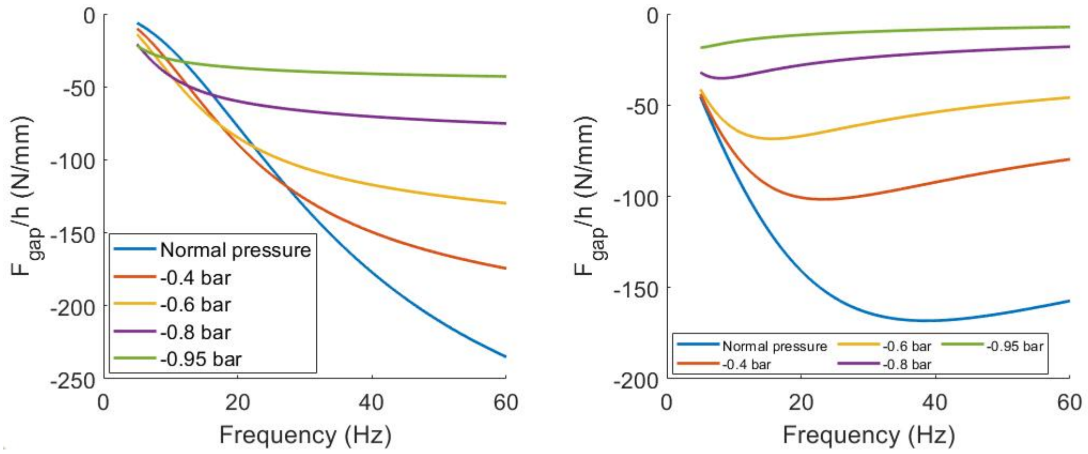

(A) Real Part (B) Imaginary Part

FIGURE 5.23: The effect of ten times higher viscosity on the real (A) and imaginary (B) parts of the force acting on the upper plate for 0.1 mm gap thickness at various pressure

Figure 5.24 shows exactly same trends as Figure 5.19. However, as the thickness of the air gap continues to increase and becomes comparable to that of the viscous boundary layer, the imaginary part of the force acting on the plate becomes relatively independent of the air pressure.

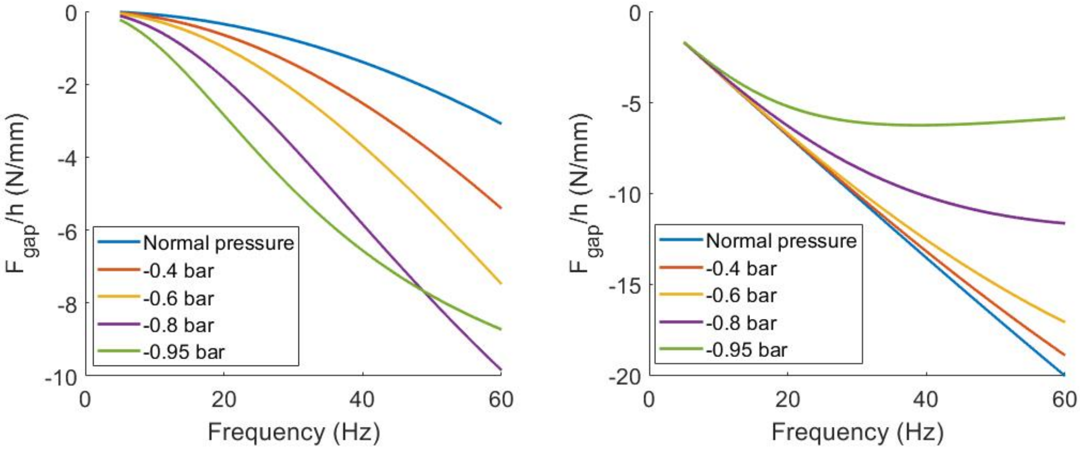

(A) Real Part (B) Imaginary Part

FIGURE 5.24: The effect of ten times higher viscosity on the real (A) and imaginary (B) parts of the force acting on the upper plate for 0.3 mm gap thickness at various pressure

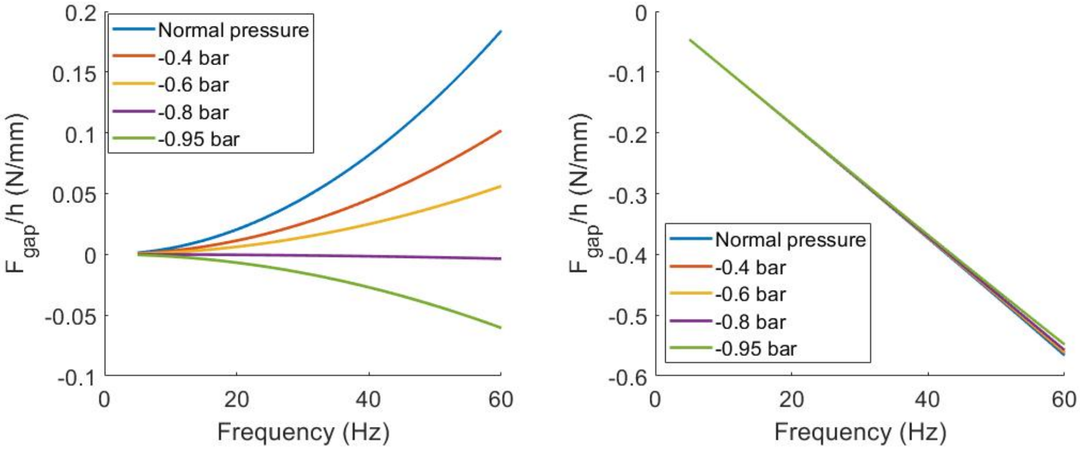

(A) Real Part (B) Imaginary Part

FIGURE 5.25: The effect of ten times higher viscosity on the real (A) and imaginary (B) parts of the force acting on the upper plate for 1 mm gap thickness at various pressure

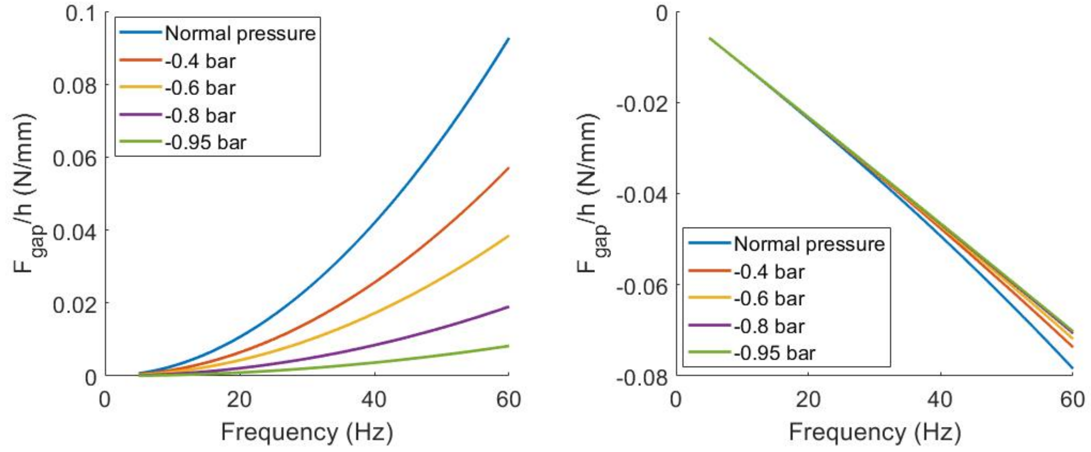

(A) Real Part (B) Imaginary Part

FIGURE 5.26: The effect of ten times higher viscosity on the real (A) and imaginary (B) parts of the force acting on the upper plate for 0.2 mm gap thickness at various pressure

5.6 Summary

In this chapter, numerical modelling with COMSOL finite element software was used with the Johnson-Champoux-Allard model to predict the effect of the air film. This model was simplified as two plates with an air layer in the middle. The forces from the air gap acting on the upper plate from various gap thickness and ambient pressure were simulated by this model. The resonant frequency and the damping ratio were obtained by fitting with the experimental model. By comparing the results with the data from the other two methods, they both show a similar trend as changing the different parameters, e.g. air gap thickness, pressure, mass and viscosity. In terms of the resonant frequency of the pumping mode, the results from both FE modelling and the low reduced frequency model shows an excellent agreement.

Generally, the air film dampers have higher energy dissipation efficiency with thinner gap thickness. For thin air gap, as defined by Fox and Whitton [21], which the thickness is greatly smaller than other dimension and smaller than air boundary layer thickness, the real part of the force is dominated by the viscous effect, under some critical conditions, for instance, high viscosity and high-frequency range, the airflow will be restricted by the high viscous effect and it tends to be compressed rather than pumped. This explains why the peaks observe on the force-frequency curves, for example, Fig 5.23. However, as discussed in the previous chapter, the low reduced frequency model cannot show relevant results for such behaviour, as shown in Fig 3.8. Therefore, as this aspect, the JCA FE model is more close to the real behaviour of the air gap.

The piston-like behaviour of air can reduce the performance of air film damper. Besides the high viscosity and the thin air gap thickness, this behaviour is also more easily occurs in low frequency at low pressure or high viscosity conditions. Because lower pressure can make the air to be compressed instead of being pumped in and out. Therefore, although the pressure has been examined that not directly affect the damping efficiency of the system much, when design an air film damper, the ambient pressure will be also considered.

To optimise the air film damper, the geometry of the air gap, the combination of pressure, density and viscosity are important. The next chapter will be focused on optimising of air film damper by developing some particular shapes of the air gap.

Chapter 6

Air Film Damper Optimization

6.1 Introduction

It was illustrated in the previous chapter, that the Johnson-Champoux-Allard Model in COMSOL is capable of predicting the acoustic pressure in a rectangular, slit-like air gap between the plate and solid base. Clearly, the shape of the air gap is an important character that can influence the damping of the air film trapped between the two plates. The main objective of this chapter is to study the damping efficiency of the air gap which has some particular geometry. Three categories of novel geometries will be discussed in this chapter, which are step-thickness, air gap with baffles, and snail baffles in an air gap.

In this chapter, as the damping for the optimised geometries are usually too high that cannot observe resonance of the pumping mode on their mobility FRF curves. Therefore, the force acting on the top plate from the air gap are directly compared, as the magnitude of imagery part of such force can indicate the damping that the air layer can actually contribute.

This chapter also presents results obtained research for an elastic plate which is a more practical situation than with the plates assumed as being rigid.

6.2 Geometrical optimization

In this section, several different types of air gap geometries were studied and analysed. Let us assume that we deal with the same plate setup as considered in Chapter 5. The displacement applied on the top plate is fixed to 1% of the gap thickness. Therefore the acoustic force (F_{gap}) was therefore directly plotted and compared on the following sections. The other setting is exactly same as in Chapter 5, however, in order to make the plate more like a ’panel’, the two long edges are now set as "Sound Hard Boundary" instead of "Sound Soft Boundary". In this case, the air cannot go through these edges.

6.2.1 Benchmark

The benchmark of the acoustic force was then set up, in order to quantify the damping efficiency from other air gap geometries. In this benchmark, the air gap thickness was 1mm, with 1% upper plate displacement. Since, in this chapter, the air gap thickness and the displacement of the upper plate are fixed to 1mm and 1%, respectively, the acoustic force in Newton are directly compared, instead of normalised force in previous chapters. Although, according to the results, a smaller gap thickness ca1n provide more damping to the system, however, on the other hand, it more easily get the air piston-like behaviour in lower frequency. Therefore, an intermediate thickness, 1mm was chosen to compare the energy dissipation effect for the optimised geometries. The results of benchmark acoustic force are shown in Figure **??**.

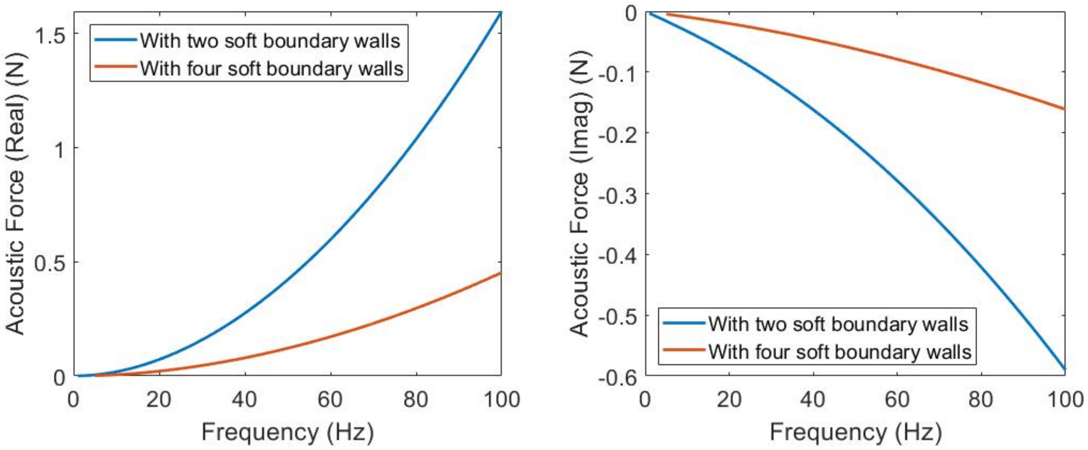

(A) Real Part

(B) Imaginary Part

FIGURE 6.1: The real (A) and imaginary (B) parts of the acoustic force benchmark with 1 mm gap thickness

6.2.2 Step thickness of air gap

The various thickness of the air gap geometry has been simulated with COMSOL to study energy dissipation for the geometry that has a large volume with a smaller area of sound soft boundary. In this study, the step was used to simulate the effect of air gap geometry with two different thickness. The geometry is shown in figures **??** and **??**. The thickness of the air gap on both ends is $1mm$, as the thickness in the middle is $1.5mm$.

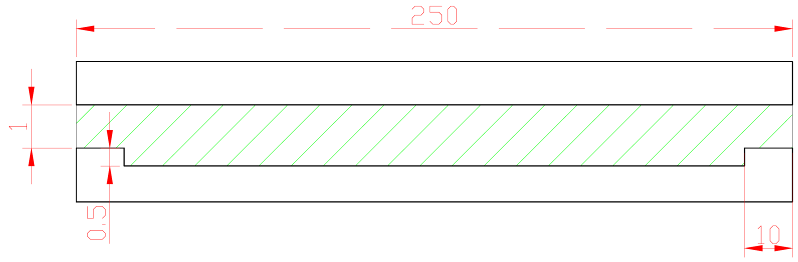

FIGURE 6.2: Cross-section of the air gap step thickness

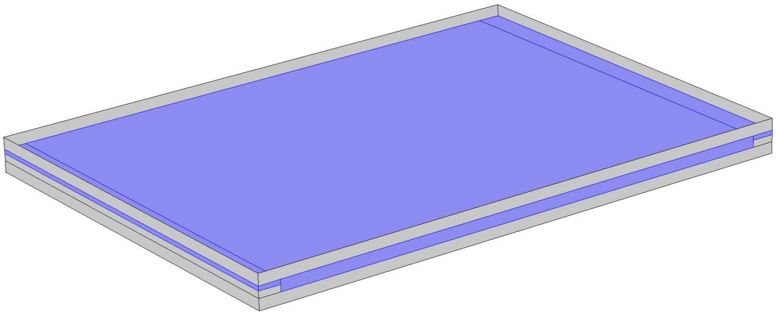

FIGURE 6.3: Step thickness air gap geometry modelled in COMSOL

The results in Figure **??**, shows that the force from the air decreased compared with the benchmark. The reason for this result is that the air gap thickness in the middle was 1.5 mm which was larger than the thickness of the benchmark. When applying body displacement on the top plate with the same amplitude, the viscous effect had to be reduced. If the thickness of the opening edges were further reduced the acoustic force would be further decreased, as in this case the air in the gap trend more to be compressed. Therefore, this type of geometry is not recommended.

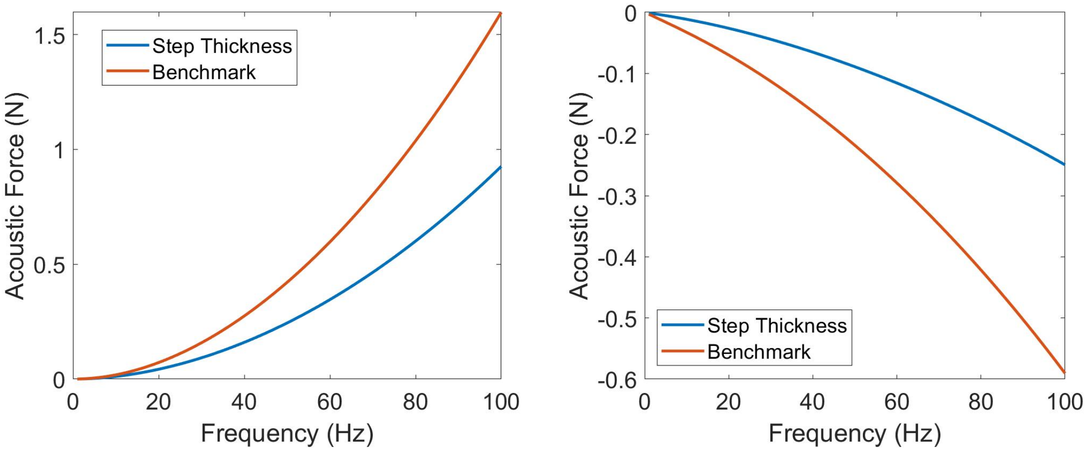

(A) Real Part (B) Imaginary Part

FIGURE 6.4: The real (A) and imaginary (B) parts of acoustic force of step thickness and benchmarks with 1 mm thickness

6.2.3 Baffles inside of the air gap

In order to increase the moving distance of the air in the air gap excited by the vibrating plate, baffles were introduced to extend the effective channel length. The geometry shown in Figure **??** has 6 baffles with 1 mm width and 160mm length, which run along the cross-section and equally distributed along the 250mm edge. The baffles were set as ’surface’ in COMSOL, which means the baffle does not have any physical property except airflow restriction.

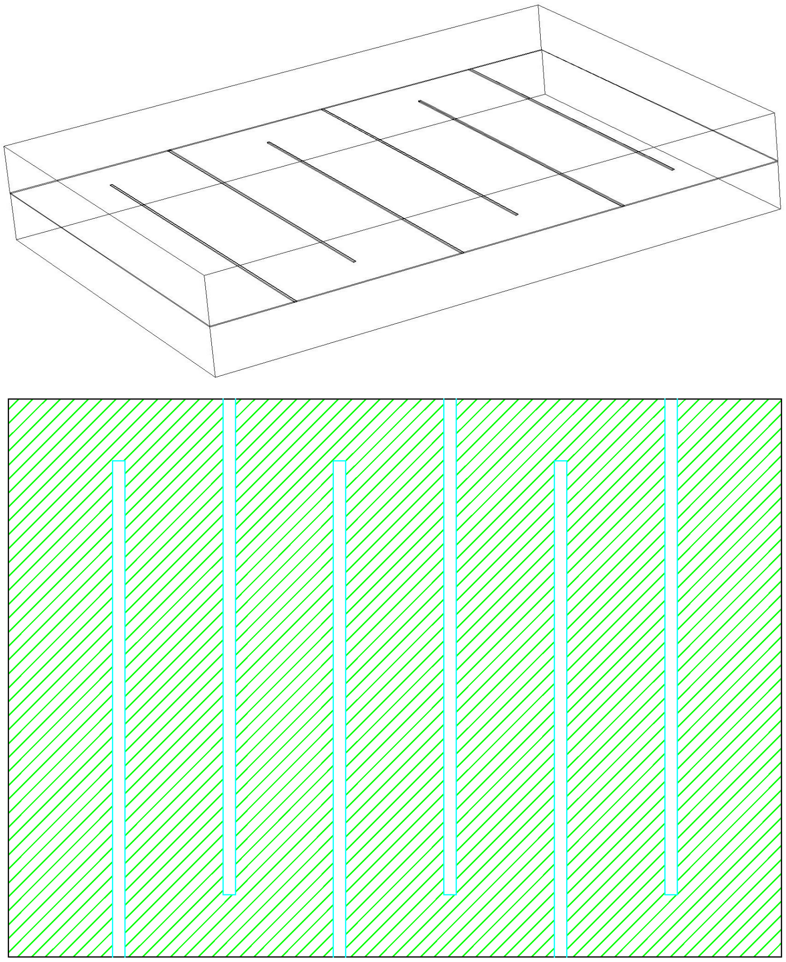

FIGURE 6.5: Geometry of 6 baffles air gap

As shown in Figure **??**, compared with the acoustic force from the benchmark (Figure **??**) the acoustic force in this geometry was dramatically increased by the baffles. The increment of the imaginary part of the acoustic force indicates a much more damping and energy dissipation effect of the air in the gap, compared with the geometry for the benchmark. The pressure distribution of the 6 baffles geometry is shown in Figure **??**.

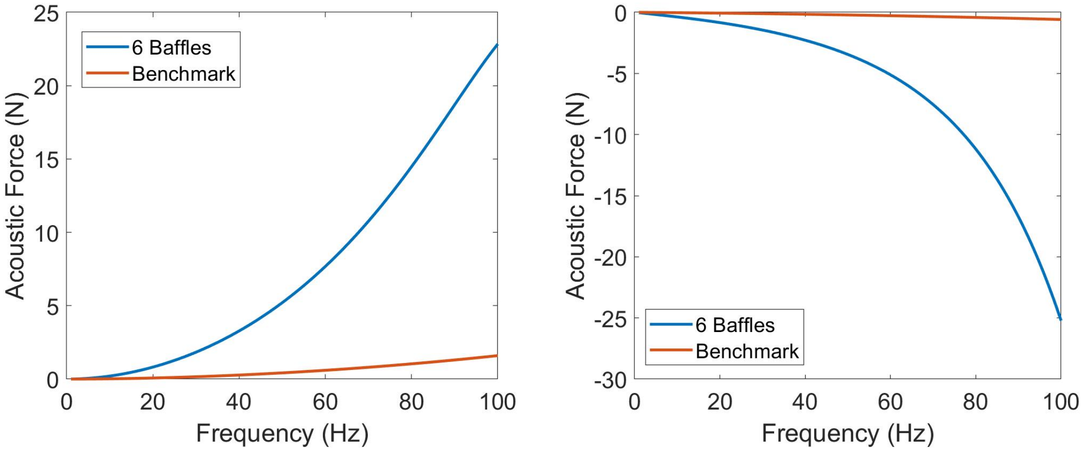

(A) Real Part

(B) Imaginary Part

FIGURE 6.6: The real (A) and imaginary (B) parts of acoustic force of geometry with 6 baffles

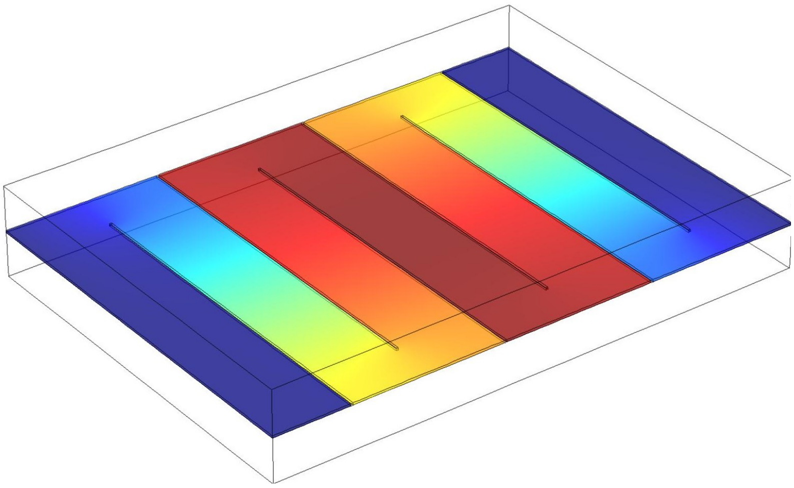

FIGURE 6.7: Pressure distribution in the air gap with 6 baffles geometry

Change the number of baffles

In order to understand how the number of baffles can influence the damping effect, additional predictions were done for 4 and 9 baffles in the air gap and the acoustic force from these geometries were compared with the benchmark respectively.

Figures **??** and **??** show the pressure distribution and the acoustic force from 4 baffle geometry compared with the benchmark results in 1 mm gap thickness. It can be seen that the imaginary part of the acoustic force remains considerably large compared with the benchmark. However, since the effective channel length was reduced in 4 baffles geometry, the acoustic force reduced about 50% when compared with the 6 baffles.

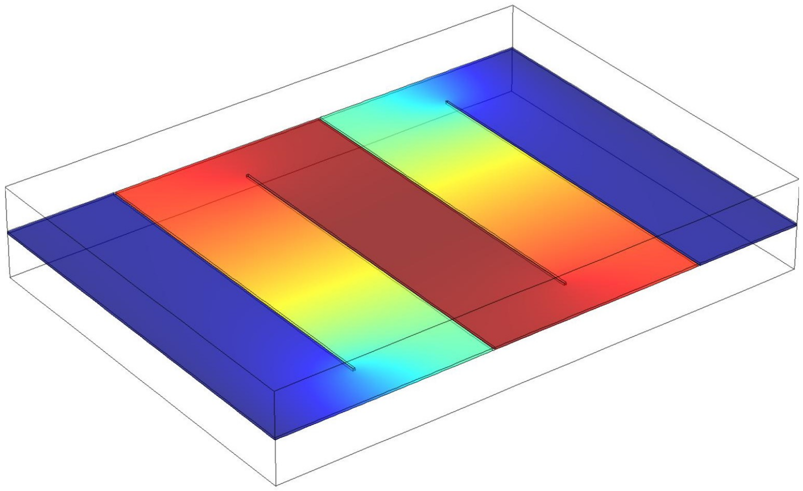

FIGURE 6.8: Pressure distribution in the air gap with 4 baffles geometry

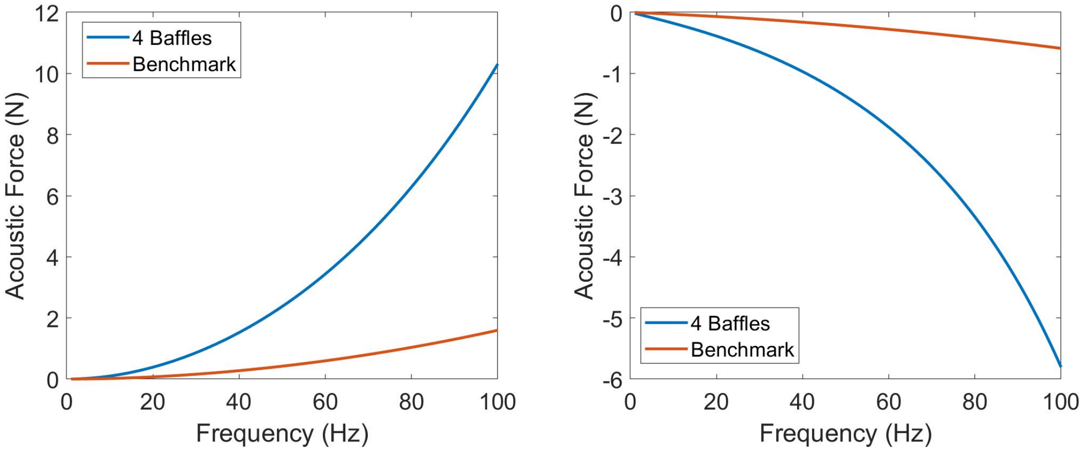

(A) Real Part (B) Imaginary Part

FIGURE 6.9: Result of Geometry with 4 Baffles

Figures **??** and **??** show the pressure distribution and the acoustic force from 9 baffle geometry compared with the benchmark results in 1 mm gap thickness. A peak can be observed in both real and imaginary part of the acoustic force from the 9 baffles. In the maximum value of the imaginary part of the acoustic force can be reached to 70 N at 90 Hz, which is huge compared with the previous geometries so far. The imaginary acoustic force would drop with larger frequency after the peak because the air in the gap would tend to be compressed in high frequency. Therefore, for this geometry of the air gap, the damping reaches the maximum at 90 Hz.

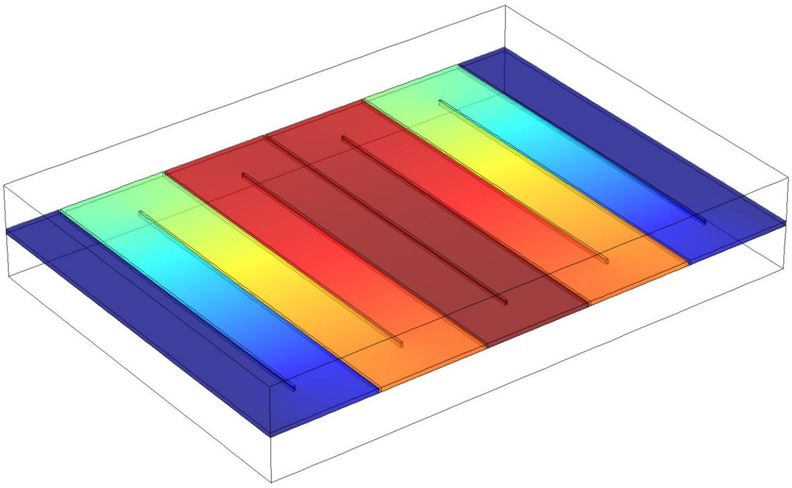

FIGURE 6.10: Pressure distribution in the air gap with 9 baffles geometry

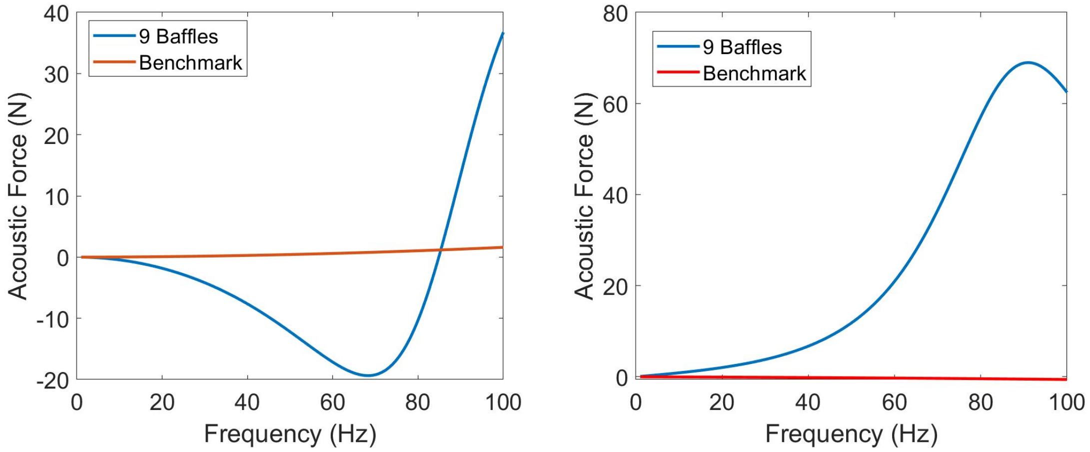

(A) Real Part

(B) Imaginary Part

FIGURE 6.11: Result of geometry with 9 baffles

Equivalent length of baffles geometries

To quantify how the acoustic force changes with the changing number of baffles it makes sense to introduce a notion of effective length. A baffle in the air gap changes the direction and extends the length of the airflow. In this way, the baffle geometry can be equivalent a slender geometry.

Taking the 9 baffles geometry for example, as shown in Figure **??**, the red line represents the length of the air in the gap moves. The equivalent slender geometry should has the same length with that. The width of the equivalent geometry then equals to the distance between two baffles. Therefore, the width (W_e) and length (L_e) of the equivalent slender geometry are:

$$W_e = 2l_x/(N_b+1) \quad and \quad L_e = (N_b-1)L_b + (2l_x - 2W_e) \tag{6.1}$$

where N_b is number of baffles and L_b is the length of the baffle.

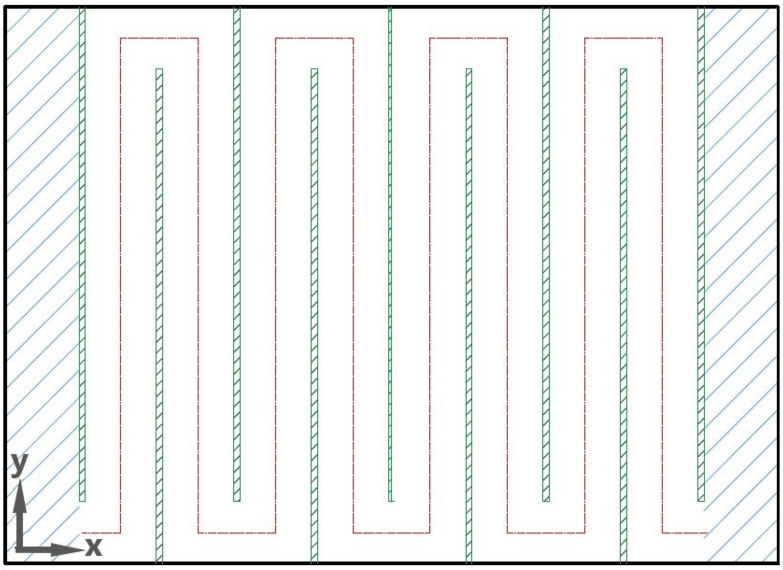

FIGURE 6.12: Equivalent length of baffles geometry

The effective the slender geometry for 9 baffles air gap was calculated by the equation **??** and is shown in Figure **??**.

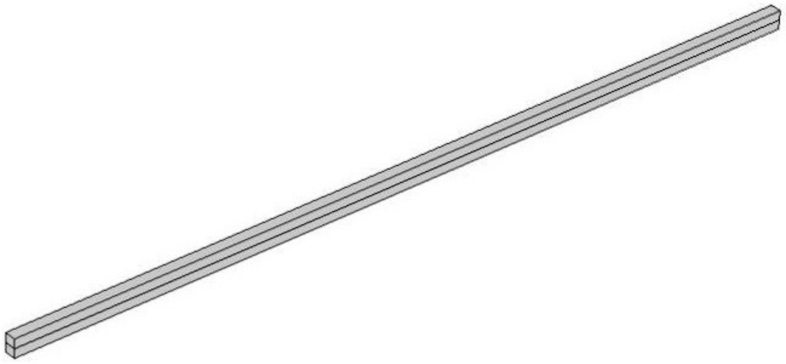

FIGURE 6.13: Geometry of effective slender

Figure **??** shows the comparison of the acoustic force for the 9 baffles geometry and its equivalent geometry. The acoustic forces from the two geometries are nearly identical below 80 Hz. However, a small difference occurs on the peak which is about 90 Hz. This because in the 9 baffles geometry the air moving direction was periodically changed by the baffles, which would cause extra energy dissipation, whereas the air in the gap of slender equivalent geometry moved in a constant direction.

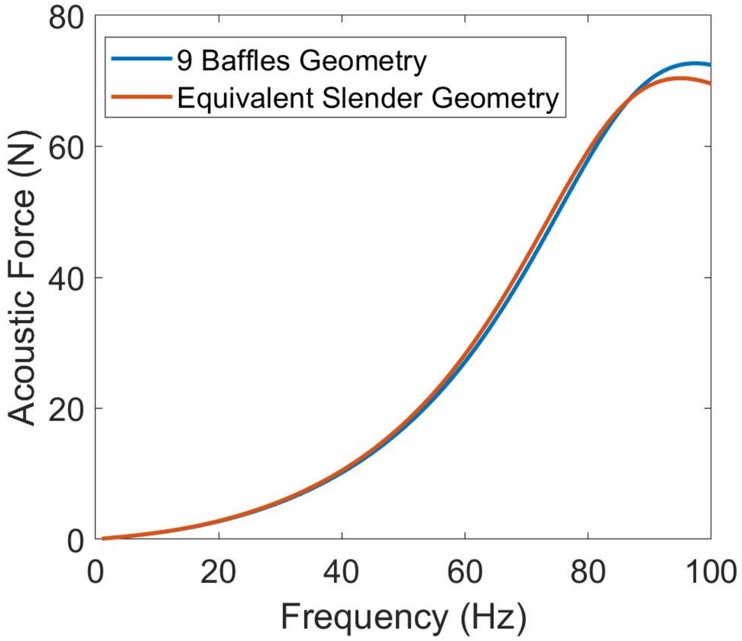

FIGURE 6.14: Comparison of acoustic force for 9 baffles geometry and its equivalent slender geometry

6.2.4 Snail baffles

Another kind of geometry that can efficiently extend the length of the air channel is the baffle with snail-liked shape. There are two types of snail geometries were developed, as shown in Figure **??**. In the type 1 air can only be pumped through one side, whereas in the type 2 air can being pumped both sides of the gap. As the red dash lines are shown on Figure **??**, it can be observed that both two types of geometry have 5 loops and the effective length of the air channel at type 2 is longer than at type 1.

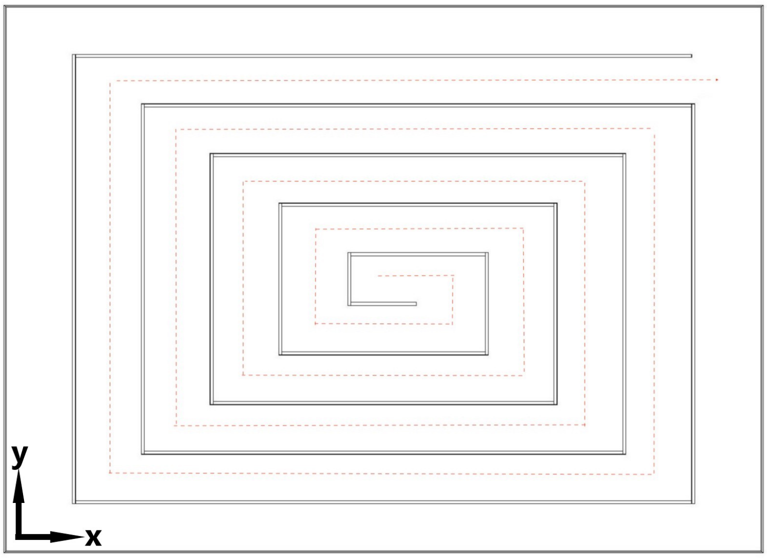

(A) Type 1

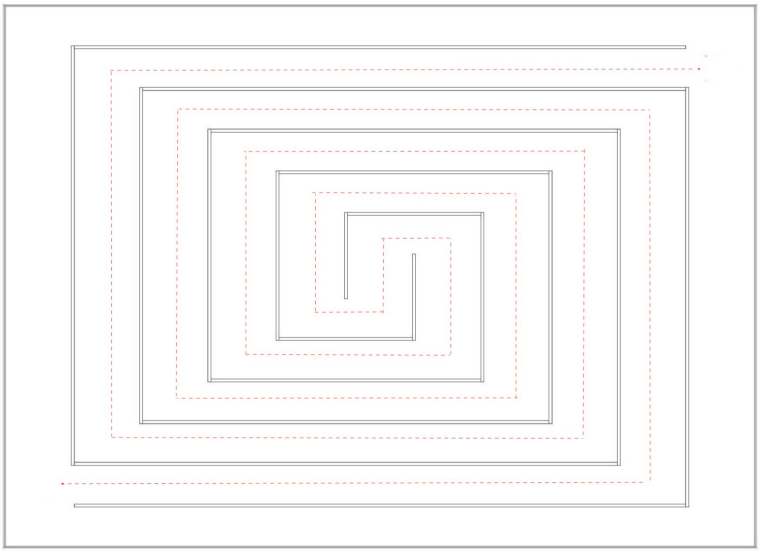

(B) Type 2

FIGURE 6.15: Geometries of snail baffles

The acoustic force for the type 1 and type 2 geometries are shown in figures **??** and **??**, respectively. The peak of the imaginary part for the acoustic force in type 1 geometry occurred at 38 Hz with 36 N maximum value, whereas in the type 2 geometry, the peak occurred at 62 Hz with 50 N maximum value. Due to the geometrical difference of two types snail geometries, the air was more likely to be compressed in the first type of geometry. Because in this type of the gap, the air can contact with ambience only through one side, as Figure **??** shows. Therefore, it is obvious that the type 2 geometry has more damping efficiency for 1 mm gap thickness.

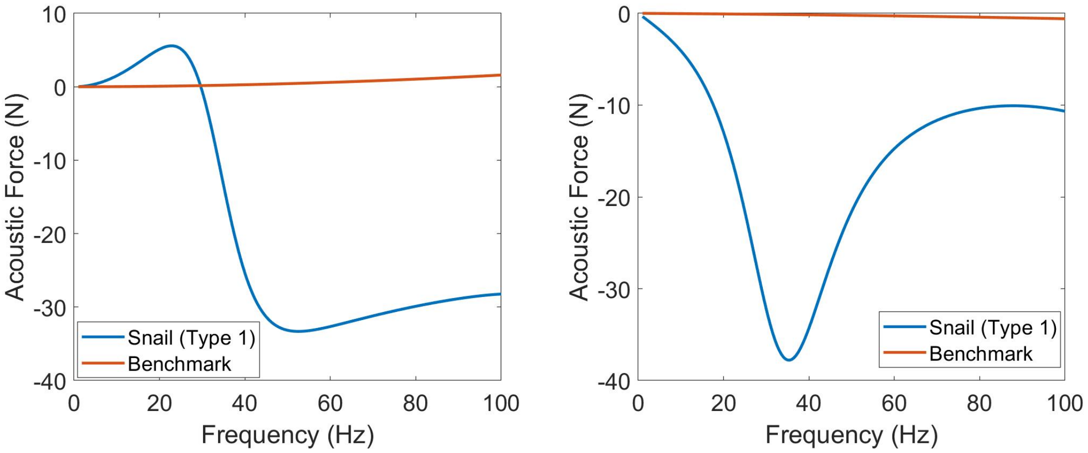

(A) Real Part (B) Imaginary Part

FIGURE 6.16: Acoustic force in the air gap of snail (Type 1) geometry

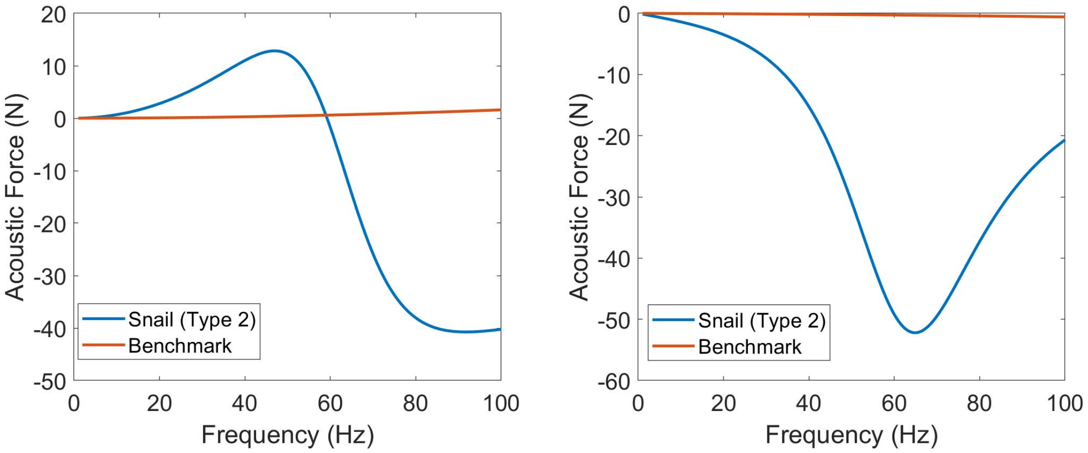

(A) Real Part (B) Imaginary Part

FIGURE 6.17: Acoustic force of snail (type 2) geometry

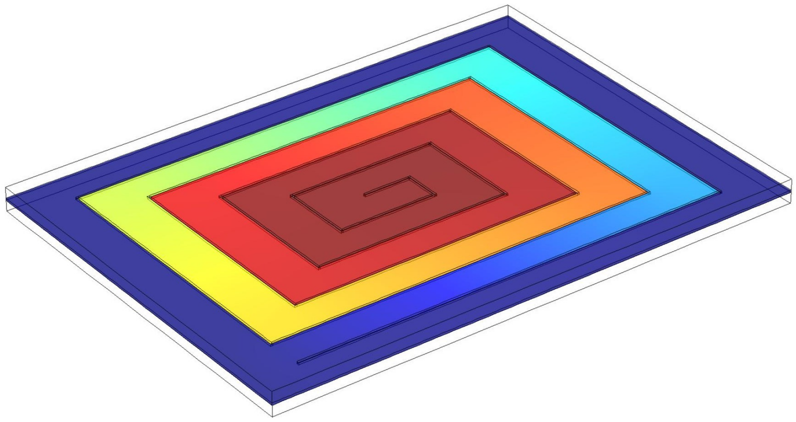

(A) Type 1

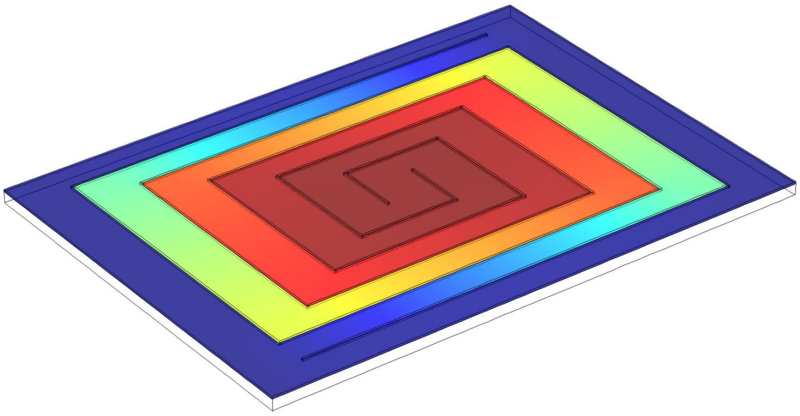

(B) Type 2

FIGURE 6.18: pressure distribution for the air in the gap of snail type 1 (A) and type 2 (B) Geometry

6.3 Flexible plate

In all previous simulations, the top plates were assumed rigid. However, in practise, the plate cannot be perfectly rigid. Therefore it is of practical interest to find out how the air film could effect on damping of an elastic plate.

The new model in COMSOL were set the both plates as structural steel, but the Young's Modulus was reduced to $2 \times 10^9 Pa$ to make the plate properly elastic so that it could have structural modes at frequencies below 100 Hz. Both plates have same size as previous, which was 250 mm × 180 mm. The thickness of the top plates was set to 2 mm. Additionally, a point prescribed displacement ($U_{oz} = t_{gap}/100$) was acting on the centre of the top plate instead of displacement for whole body.

6.3.1 Thickness effect

Since thickness is the main and most obvious factor that could effectively change the damping of the air film, a simulation was carried out to determine the thickness effect on the acoustic force in the air gap. Four different thickness of the air gap: 0.3 mm, 0.5 mm, 1 mm and 2 mm, have been applied in this section.

The receptance FRF has been figured out by using the displacement of top plate corner point, as shown on figure **??**, divided by the reaction force from excitation.

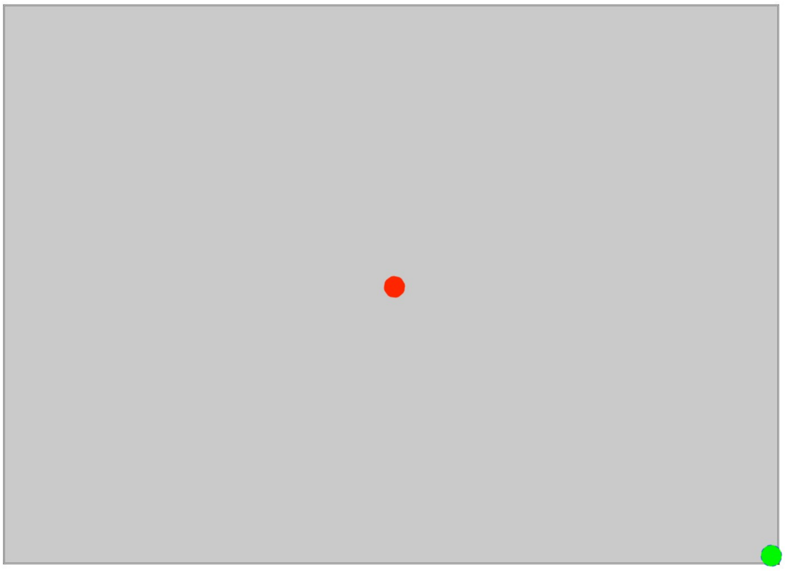

FIGURE 6.19: Measuring (green) and excitation (red) points

Without the effect of the air gap, the top plate had two bending modes (at 33 and 68 Hz) below 100 Hz vibration frequency. The mode shapes were included in Figure **??**. Figure **??** shows the receptance FRF data for various gap thickness. The resonant frequency was shifted, because of the mass effect of the air gap. The amplitude of the structural resonance was also significantly reduce with the decreased thickness of the air gap. Table **??** summarises the resonant frequency and damping ratio for the two modes. It can be seen from this table that the damping ratios were dramatically increased by reduce the thickness of air gap. Therefore, the air film damper can efficiently reduce plate vibration at the frequency of a structural resonance.

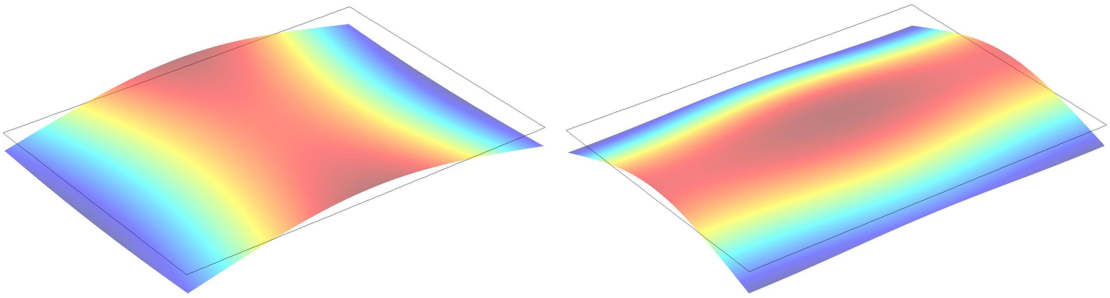

(A) Mode 1 (B) Mode 2

FIGURE 6.20: Mode shapes for flexible plate

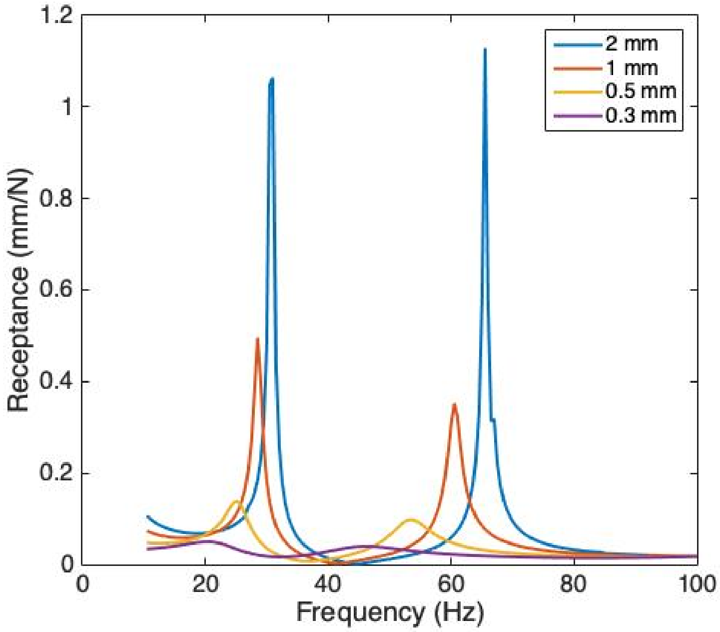

FIGURE 6.21: Receptance FRF of the flexible top plate with various gap thickness

	Mode 1		Mode 2	
Gap Thickness	ω_n	ζ	ω_n	ζ
0.3 mm	21.29 Hz	0.25	46.12 Hz	0.17
0.5 mm	25.36 Hz	0.076	53.36 Hz	0.061
1 mm	28.59 Hz	0.022	60.52 Hz	0.017
2 mm	30.76 Hz	0.007	65.51 Hz	0.005

TABLE 6.1: Resonant frequency and damping ratio for two modes of the flexible top plate for various gap thickness

6.3.2 Particular Geometries

The results shown in the previous section illustrated that the air gap can effectively reduce vibration of plate bending modes. The objection of this section is to further assess the effectiveness of the novelty geometries introduced in this chapter. Hence, in this section, two types of geometries (6 baffles and type 1 snail baffle) were used for further study. The gap thickness was constantly 1 mm and the force applied on the top plate was exactly the same with Section **??**. The data of acoustic force for 1 mm flexible top plate in Section **??** was, therefore, being compared in this section as the benchmark value.

It can be seen from the results shown in Figure **??** that in the 6 baffle geometry, the first bending mode was effectively reduced. However, the second bending mode has even higher receptance than the benchmark result. This because the reason that the baffles in the air film were distributed to parallelise the y-axle. For the first mode, as shown in Figure **??**a, the air was easily being pumped, whereas in the second mode, as shown in Figure **??**b, the air was more likely being trapped between the baffles.

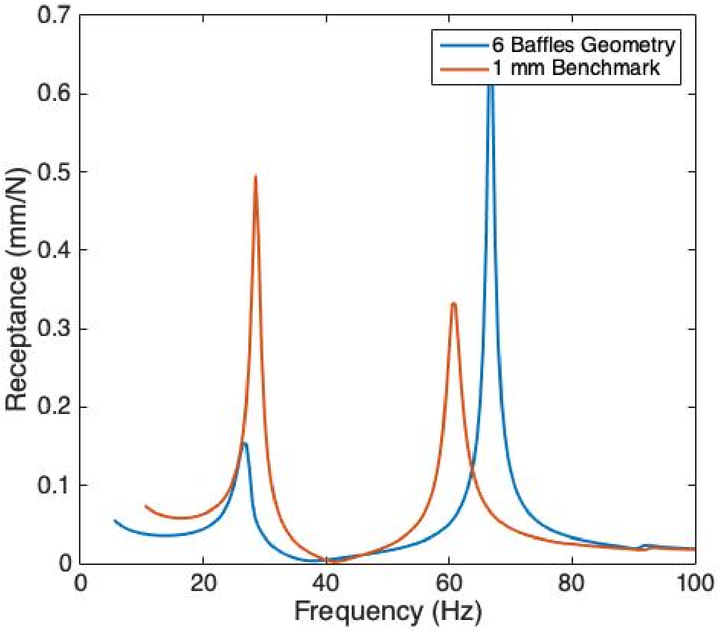

FIGURE 6.22: Result for 6 baffles geometry with flexible plate

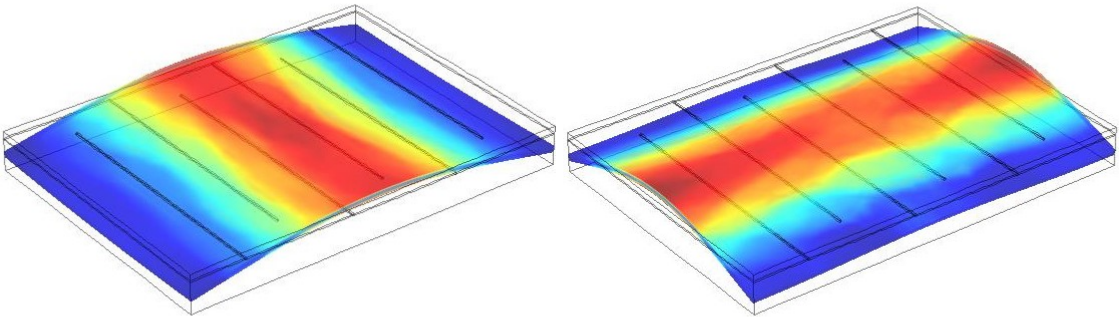

(A) Mode 1

(B) Mode 2

FIGURE 6.23: Mode shapes for 6 baffles geometry with flexible plate

The receptance FRF of the type 1 snail geometry compared with the benchmark is shown in Figure **??**. Three modes can be observed from the receptance FRF, and the mode shape is shown in Figure **??**. The first bending mode can be clearly observed at about 20 Hz with amplitude dramatically reduced. Whereas the second mode, which appears at 52 Hz, was nearly eliminated by the large damping effect of the air gap.

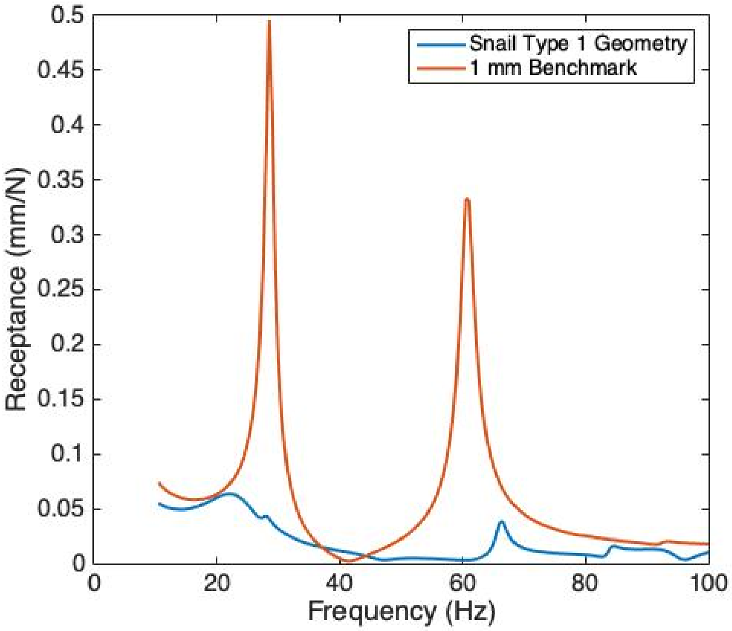

FIGURE 6.24: Result for snail (Type 1) geometry with flexible plate

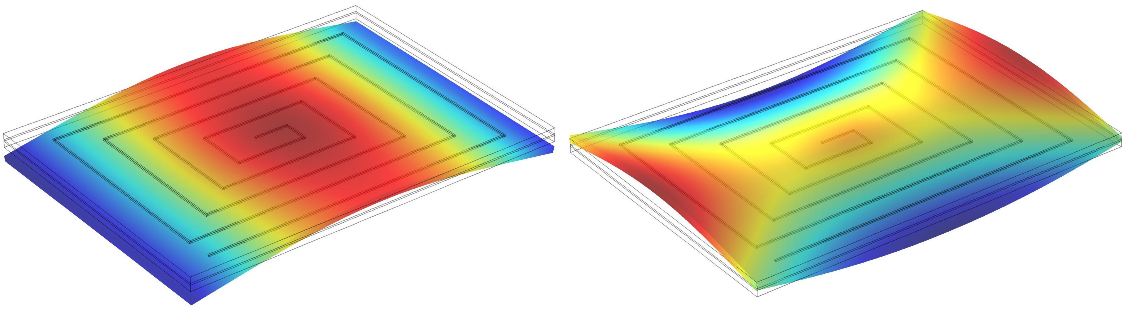

(A) Mode 1

(B) Mode 2

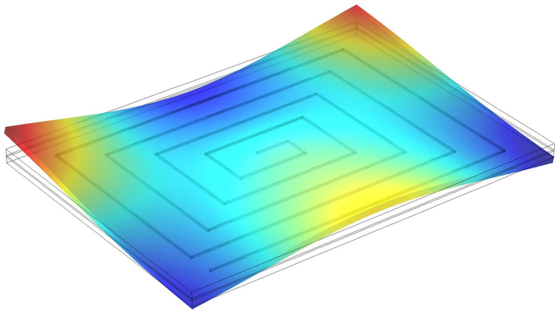

(C) Mode 3

FIGURE 6.25: Mode shapes for snail (Type 1) geometry with flexible plate

6.4 Incompressible fluid in the slit

In previous work, the air in the gap performs excellently in term of energy dissipation effect, but for some complex geometries, since air is a compressible fluid, the air tends to be compressed. Then, as a consequence, the damping and energy dissipation efficiency of the air gap was reduced dramatically. Therefore, this section presents the simulation of what is happening in the air gap which is filled with an incompressible fluid, for example, water. Thus, in this section, water was applied to replace the air in the silt. The setup in this section was the same as what was done in Section 6.2.1, but replaced the fluid in the gap to water. Three different gap thickness: 2 mm, 1 mm and 0.5 mm, were analysed to identify how the thickness can affect the acoustic force.

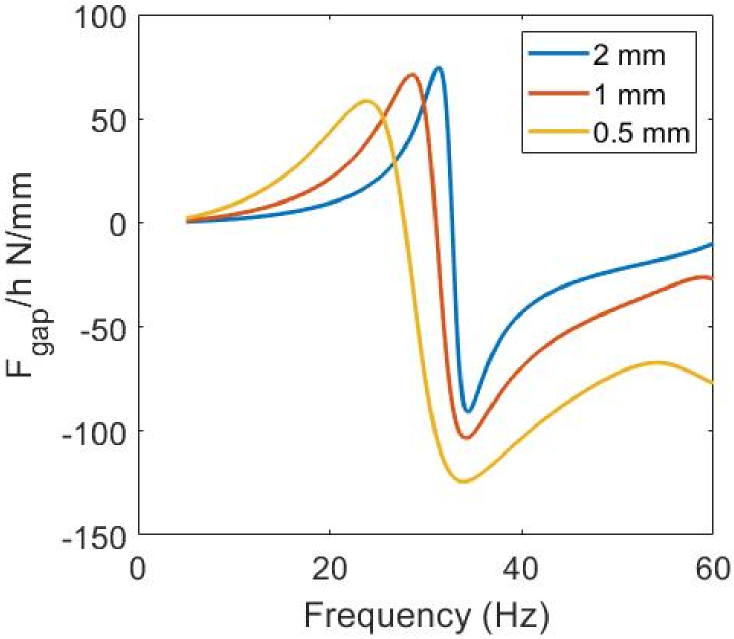

(A) Real Part

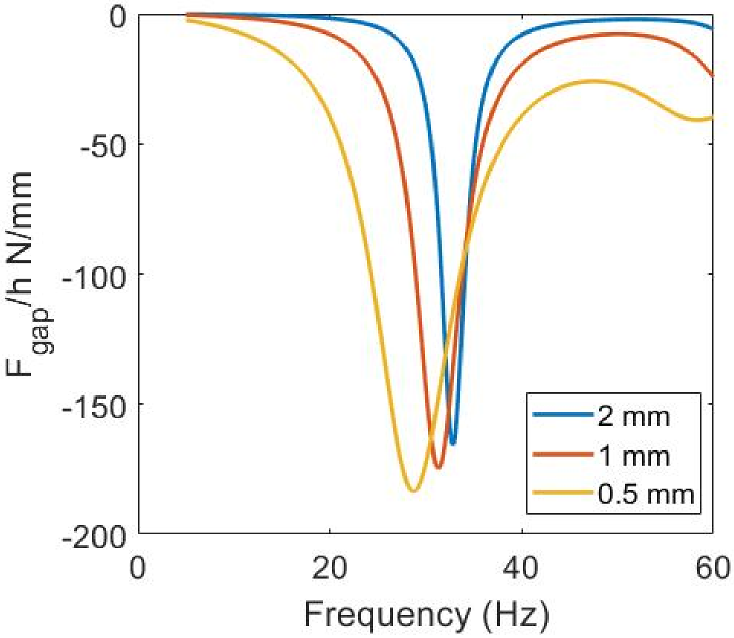

(B) Imaginary Part

FIGURE 6.26: Real part (A) and imaginary part (B) of normalised acoustic force for water gap with various gap thickness

Since the displacement of the top plate was $h = 2h_0/100$, the normalised acoustic force was compared in Figure **??**. Resonance can be found at around 30 Hz and the amplitudes of the normalised force for different gap thickness are nearly identical. Therefore the thickness would not be the main factor on the energy dissipation effect of the fluid gap.

6.5 Summary

In this chapter, several special geometries with baffles in the slit were studied. With same gap thickness, a large increment of the imaginary part of the acoustic force can be observed. This represents the damping from the air in the gap are greatly increased. It has also been found that the amount of acoustic force depends on the length of air, within the slit, can move. However, for some geometries, for example, type 1 of snail geometry, as there is a dead-end in the centre, the air is more likely trapped by the barriers, therefore the piston-like behaviour occurred in the lower frequency, and as the results, damping ratio would be dramatically reduced.

The flexible plate was also simulated to show how the structure interacts with the air. It can be found that the damping effect depends on both the assignment of baffles and the modes of the plate. For example, the 6 baffles geometry, because of its assigned direction of baffles, the air was trapped at second mode and the damping at this resonance was dramatically decreased.

Additionally, the incompressible fluid was analysed. The result shows the acoustic force is only proportional to the displacement of the top plate.

Chapter 7

Conclusion and Future Work

7.1 Conclusion

In this thesis, three methods for studying the energy dissipation performance of air film dampers have been presented and discussed. These involve experimental, analytical and finite element simulation techniques for representing the behaviour of an air gap with a vibrating wall.

It was found that the JCA model is capable to simulate the energy dissipation of the air in the double panel or more complex of geometries. The acoustic pressure distribution along the surface of the plate can be simulated using COMSOL with the JCA model, and the damping ratio and the resonant frequency can be estimated by adding relevant mass and stiffness to the system. It was also found that the low reduced frequency model developed by Beltman and Tijdeman can estimate the damping ratio and resonant frequency only within low-frequency range where the air is dominated by pumping-like behaviour. For higher frequencies, where the air piston-like behaviour occurs, this model usually gets higher damping than the actual result.

The analytical low reduced frequency model was introduced in Chapter 3. When dealing with an air gap which has high viscosity a limitation of this model was found in which the acoustic force of the fluid only shows an almost linear relationship with the frequency. The model does not adequately represent the tendency of the fluid to compress and expand. This is a limitation for the model's use in practical design optimizations as the critical frequency defining the onset of compressible behaviour is an important design parameter.

In Chapter 4, an experiment was carried out in order to validate both the analytical model and the JCA model and study the relationships of air gap damping efficiency with ambient pressure and gap thickness. The gap thickness was found as the most significant factor affecting the damping of the system. When the air gap thickness was smaller than the air boundary layer thickness (this was around 0.4 mm at 15 Hz for the systems studied), as the damping from the air layer was high enough, the system pumping resonance was hardly observed from the FRF. On the other hand, the pressure was found to have a slight effect on the damping and the resonant frequency.

The Johnson-Champoux-Allard model was used to simulate the air gap behaviour using COMSOL software. Results from this model were compared with the analytical model and experiment. The resonant frequency excellently agreed with the analytical results with at most 1.3% difference. Results from these three methods show the same trends when changing a particular parameter, e.g. gap thickness, pressure, mass and viscosity. The relationship between the air gap energy dissipation and the air viscous effect was investigated by increasing the viscosity of air. The acoustic force of the air was found dramatically increased by higher viscosity. However, the air was more likely to be compressed in that situation.

The FE model was then used in design studies. Several types of air gap geometry were studied. It was found that more energy is dissipated in longer air channels. However, in some cases, where the geometry of the air gap is too complex, the air becomes trapped. Under these conditions, critical frequency of the air at which piston-like compression takes place, occurs at lower frequencies. Therefore, in conclusion, for general air gap optimisation the important factors and considerations are:

- the effective length of the channel,
- the viscosity of air,
- frequency range of interest,
- the average thickness and the width of the gap,
- ambient pressure of the air gap.

7.2 Suggestions for future work

- Coupling of structural vibration modes with the air gap.

  In most of this study, the walls enclosing the air gap were assumed rigid. Walls formed using flexible plates are more realistic for panel damper applications. These might involve even and odd modes as indicated in Figure 7.1. Analysis of such systems is possible using the numerical approach introduced in this work.

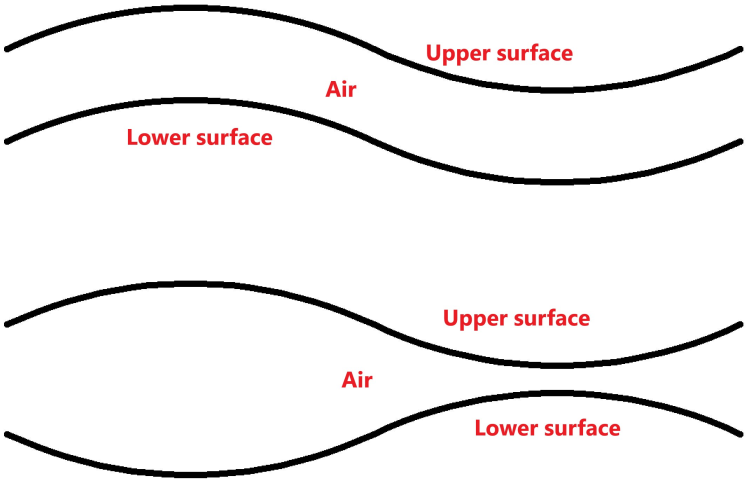

FIGURE 7.1: Two surfaces deform in same direct (upper) and two surfaces deform in opposite direction (bottom)

- More complex geometries can be modelled.

  In this thesis, the geometries of the air gap were restricted uniform-thickness slits. Alterations to the air gap shape, such as curved geometries, may provide additional design options. However, it is interesting to note that the optimisation study showed that step changes in thickness were not particularly useful.

- Visualisation of the airflow in complex air gap geometries is an important activity that is worth investigating once prototype optimised air gaps have been made. It can be achieved by using smoke or any other kind of coloured air. Whether the air in the gap is being trapped or being compressed will be observed for further optimisation.

- Efforts should also focus on ways to manufacture effective air gap dampers. The winding channels considered in this work should be easier to manufacture than large, constant-area slits. One option might be to develop dampers independently of the host structure and attach them in appropriate places. 3D printing is one suggested manufacture method to make the air gap with complex details inside. Since it enables to make very complex geometries with satisfying precision that hard to be achieved by conventional methods. However, it is quite expensive and time-consuming. Another suggested method is bonding slender soft material strips on the air panel surface. However, precision would be a potential problem.

- The size of the air gap in this thesis is about A4 paper size, hence it can only be applied in small machinery with tiny vibration displacement. Therefore, the study for an enlarged air gap is suggested for future work. Since it can potentially be applied for civil engineering.

Bibliography

[1] C. W. De Silva. *Vibration damping, control, and design*. CRC Press, 2007.

[2] S. H. Crandall. "The role of damping in vibration theory". In: *Journal of sound and vibration* 11.1 (1970), 3–IN1.

[3] A. D. Nashif, D. I. Jones, J. P. Henderson, et al. *Vibration damping*. John Wiley & Sons, 1985.

[4] G. Takács and B. Rohal'-Ilkiv. *Model predictive vibration control: efficient constrained MPC vibration control for lightly damped mechanical structures*. Springer Science & Business Media, 2012.

[5] I. L. Paul and E. K. Bender. *Active vibration isolation and active vehicle suspension*. Tech. rep. 1966.

[6] J. D. Leatherwood. "Active vibration isolation for flexible payloads". PhD thesis. Virginia Polytechnic Institute, 1968.

[7] D. Karnopp, M. J. Crosby, and R. Harwood. "Vibration control using semi-active force generators". In: *Journal of engineering for industry* 96.2 (1974), pp. 619–626.

[8] S. Elliott and P. Nelson. "The active control of sound". In: *Electronics & communication engineering journal* 2.4 (1990), pp. 127–136.

[9] T. T. Soong and M. C. Costantinou. *Passive and active structural vibration control in civil engineering*. Vol. 345. Springer, 2014.

[10] E. M. Kerwin Jr. “Damping of flexural waves by a constrained viscoelastic layer”. In: *The Journal of the Acoustical society of America* 31.7 (1959), pp. 952–962.

[11] D. Jones. “Viscoelastic materials for damping applications”. In: *NASA STI/Recon Technical Report A* 81 (1980), pp. 27–51.

[12] P. J. Torvik. *The analysis and design of constrained layer damping treatments*. Tech. rep. AIR FORCE INST OF TECH WRIGHT-PATTERSON AFB OH, 1980.

[13] C. Tsai and H. Lee. “Applications of viscoelastic dampers to high-rise buildings”. In: *Journal of structural engineering* 119.4 (1993), pp. 1222–1233.

[14] S. Park. “Analytical modeling of viscoelastic dampers for structural and vibration control”. In: *International Journal of Solids and Structures* 38.44-45 (2001), pp. 8065–8092.

[15] S. Zghal et al. “Model reduction methods for viscoelastic sandwich structures in frequency and time domains”. In: *Finite Elements in Analysis and Design* 93 (2015), pp. 12–29.

[16] K. Shen and T. Soong. “Modeling of viscoelastic dampers for structural applications”. In: *Journal of Engineering Mechanics* 121.6 (1995), pp. 694–701.

[17] D. Lee and D. P. Taylor. “Viscous damper development and future trends”. In: *The Structural Design of Tall Buildings* 10.5 (2001), pp. 311–320.

[18] E. E. Ungar. *Energy dissipation at structural joints; mechanisms and magnitudes*. Tech. rep. BOLT BERANEK and NEWMAN INC CAMBRIDGE MA, 1964.

[19] J. Carbonell and E. Ungar. “On panel vibration damping due to structural joints.” In: *AIAA Journal* 4.8 (1966), pp. 1385–1390.

[20] G. Maidanik. “Energy Dissipation Associated with Gas-Pumping in Structural Joints”. In: *The Journal of the Acoustical Society of America* 40.5 (1966), pp. 1064–1072.

[21] M. Fox and P. Whitton. “The damping of structural vibration by thin gas films”. In: *Journal of Sound and Vibration* 73.2 (1980), pp. 279–295.

[22] W. Beltman. “Viscothermal wave propagation including acousto-elastic interaction, part I: theory”. In: *Journal of Sound and Vibration* 227.3 (1999), pp. 555–586.

[23] W. Beltman. “Viscothermal wave propagation including acousto-elastic interaction, part ii: Applications”. In: *Journal of Sound and Vibration* 227.3 (1999), pp. 587–609.

[24] W. Beltman et al. “Implementation and experimental validation of a new viscothermal acoustic finite element for acousto-elastic problems”. In: *Journal of sound and vibration* 216.1 (1998), pp. 159–185.

[25] W. Beltman et al. “Air loads on a rigid plate oscillating normal to a fixed surface”. In: *Journal of Sound and Vibration* 206.2 (1997), pp. 217–242.

[26] W. M. Beltman. “Viscothermal wave propagation including acousto-elastic interaction”. 1998.

[27] V Ramamurthy and U. Rao. “The steady streaming generated by a vibrating plate parallel to a fixed plate in a dusty fluid”. In: *Fluid dynamics research* 2.1 (1987), p. 47.

[28] C. Wang and B Drachman. “The steady streaming generated by a vibrating plate parallel to a fixed plate”. In: *Applied Scientific Research* 39.1 (1982), pp. 55–68.

[29] P Merkli and H Thomann. “Transition to turbulence in oscillating pipe flow”. In: *Journal of Fluid Mechanics* 68.3 (1975), pp. 567–576.

[30] W. Griffin, H. H. Richardson, and S Yamanami. “A study of fluid squeeze-film damping”. In: *Journal of Basic Engineering* 88.2 (1966), pp. 451–456.

[31] S. Hashemi and B. Roylance. “Analysis of an oscillatory oil squeeze film including effects of fluid inertia”. In: *Tribology Transactions* 32.4 (1989), pp. 461–468.

[32] J Prakash and H Christensen. “Squeeze films between two rough rectangular plates”. In: *Journal of Mechanical Engineering Science* 20.4 (1978), pp. 183–188.

[33] R. Terrill. “The flow between two parallel circular disks, one of which is subject to a normal sinusoidal oscillation”. In: *Journal of Lubrication Technology* 91.1 (1969), pp. 126–131.

[34] G. Stokes. “On the Communication of Vibration from a Vibrating Body to a Surrounding Gas”. In: *Philosophical Transactions of the Royal Society of London Series I* 158 (1868), pp. 447–463.

[35] G Kirchhoff. “On the influence of heat conduction in a gas on sound propagation”. In: *Ann. Phys. Chem* 134 (1868), pp. 177–193.

[36] J. Rayleigh and R. Lindsay. *The theory of Sound,(1945)*. 1945.

[37] C. Zwikker and C. W. Kosten. *Sound absorbing materials*. Elsevier, 1949.

[38] R. F. Lambert. “A study of the factors influencing the damping of an acoustical cavity resonator”. In: *The Journal of the Acoustical Society of America* 25.6 (1953), pp. 1068–1083.

[39] E. E. Ungar. “Loss factors of viscoelastically damped beam structures”. In: *The Journal of the Acoustical Society of America* 34.8 (1962), pp. 1082–1089.

[40] J Stefan. “Versuche uber die scheinbare Adhesion”. In: *Math-Naturwissenschaftliche Klasse* 69 (1868), p. 713.

[41] O. Reynolds. “IV. On the theory of lubrication and its application to Mr. Beauchamp tower’s experiments, including an experimental determination of the viscosity of olive oil”. In: *Philosophical Transactions of the Royal Society of London* 177 (1886), pp. 157–234.

[42] T Önsay. “Effects of layer thickness on the vibration response of a plate-fluid layer system”. In: *Journal of Sound and Vibration* 163.2 (1993), pp. 231–259.

[43] T Önsay. “Dynamic interactions between the bending vibrations of a plate and a fluid layer attenuator”. In: *Journal of Sound and Vibration* 178.3 (1994), pp. 289–313.

[44] A Trochidis and A Kalaroutis. “Sound transmission through double partitions with cavity absorption”. In: *Journal of Sound and Vibration* 107.2 (1986), pp. 321–327.

[45] M Moser. “DAMPING OF STRUCTURE-BORNE SOUND BY THE VISCOSITY OF A LAYER BETWEEN 2 PLATES”. In: *Acustica* 46.2 (1980), pp. 210–217.

[46] L. Chow and R. Pinnington. “Practical industrial method of increasing structural damping in machinery, I: Squeeze-film damping with air”. In: *Journal of sound and vibration* 118.1 (1987), pp. 123–139.

[47] L. Chow and R. Pinnington. "Practical industrial method of increasing structural damping in machinery, II: Squeeze-film damping with liquids". In: *Journal of sound and vibration* 128.2 (1989), pp. 333–347.

[48] D. Jones, T Lewis, and C Michael. "Partial coverage air film damping of cantilever plates". In: *Journal of Sound Vibration* 208 (1997), pp. 869–875.

[49] E. Dowell and H. Schwartz. "Forced response of a cantilever beam with a dry friction damper attached, part I: theory". In: *Journal of Sound and Vibration* 91.2 (1983), pp. 255–267.

[50] R. Mathison et al. "Measurement of air film damping effectiveness". In: *Journal of turbomachinery* 127.3 (2005), pp. 557–563.

[51] H Tijdeman. "On the propagation of sound waves in cylindrical tubes". In: *Journal of Sound and Vibration* 39.1 (1975), pp. 1–33.

[52] W. Beltman et al. "Air loads on solar panels during launch". In: *Spacecraft Structures, Materials and Mechanical Engineering*. Vol. 386. 1996, p. 219.

[53] T. Basten et al. "On the acousto-elastic behaviour of double-wall panels with a viscothermal air layer". In: *Journal of sound and vibration* 243.4 (2001), pp. 699–719.

[54] T. G. H. Basten. *Noise reduction by viscothermal acousto-elastic interaction in double wall panels*. Universiteit Twente, Enschede, The Netherlands, 2001.

[55] M. Altuğ Bıçak and M. D. Rao. "Coupled squeeze film analysis by Reissner–Mindlin plate elements". In: *Journal of Vibration and Control* 18.5 (2012), pp. 632–640.

[56] A. Akrout et al. “Vibro-acoustic behaviour of laminated double glazing enclosing a viscothermal fluid cavity”. In: *Applied Acoustics* 70.1 (2009), pp. 82–96.

[57] M. Bao and H. Yang. “Squeeze film air damping in MEMS”. In: *Sensors and Actuators A: Physical* 136.1 (2007), pp. 3–27.

[58] N Tipei. “Equatiile lubrificatiei cu gaze”. In: *Communicarile Acad. RP Romine* 4 (1954), p. 699.

[59] J. B. Starr. “Squeeze-film damping in solid-state accelerometers”. In: *IEEE 4th Technical Digest on Solid-State Sensor and Actuator Workshop*. IEEE. 1990, pp. 44–47.

[60] M Andrews, I Harris, and G Turner. “A comparison of squeeze-film theory with measurements on a microstructure”. In: *Sensors and Actuators A: Physical* 36.1 (1993), pp. 79–87.

[61] M. H. Sadd and A. K. Stiffler. “Squeeze film dampers: Amplitude effects at low squeeze numbers”. In: *Journal of engineering for industry* 97.4 (1975), pp. 1366–1370.

[62] G. Schrag and G. Wachutka. “Accurate system-level damping model for highly perforated micromechanical devices”. In: *Sensors and Actuators A: Physical* 111.2-3 (2004), pp. 222–228.

[63] G. Schrag and G. Wachutka. “Physically based modeling of squeeze film damping by mixed-level system simulation”. In: *Sensors and Actuators A: Physical* 97 (2002), pp. 193–200.

[64] J Mehner et al. "Simulation of gas damping in microstructures with nontrivial geometries". In: *Proceedings MEMS 98. IEEE. Eleventh Annual International Workshop on Micro Electro Mechanical Systems. An Investigation of Micro Structures, Sensors, Actuators, Machines and Systems (Cat. No. 98CH36176*. IEEE. 1998, pp. 172–177.

[65] Y. Lai and A. Przekwas. "A finite-volume method for fluid flow simulations with moving boundaries". In: *International Journal of Computational Fluid Dynamics* 2.1 (1994), pp. 19–40.

[66] W. Beltman, T. Basten, and H Tijdeman. "Viscothermal damping in thin gas or fluid layers". In: *1999 ASME International Mechanical Engineering Congress and Exposition*. Vol. 1500. 1999, pp. 387–395.

[67] R Shelquist. *An Introduction to Air Density and Density Altitude Calculations*.

[68] Y. Champoux and J.-F. Allard. "Dynamic tortuosity and bulk modulus in air-saturated porous media". In: *Journal of applied physics* 70.4 (1991), pp. 1975–1979.

[69] D. L. Johnson, J. Koplik, and R. Dashen. "Theory of dynamic permeability and tortuosity in fluid-saturated porous media". In: *Journal of fluid mechanics* 176 (1987), pp. 379–402.

[70] L. L. Beranek. "Acoustic impedance of porous materials". In: *The Journal of the Acoustical Society of America* 13.3 (1942), pp. 248–260.

[71] Y. Champoux, M. R. Stinson, and G. A. Daigle. "Air-based system for the measurement of porosity". In: *The Journal of the Acoustical Society of America* 89.2 (1991), pp. 910–916.

[72] M. R. Stinson and Y. Champoux. “Propagation of sound and the assignment of shape factors in model porous materials having simple pore geometries”. In: *The Journal of the Acoustical Society of America* 91.2 (1992), pp. 685–695.

[73] C. Boutin and C. Geindreau. “Estimates and bounds of dynamic permeability of granular media”. In: *The Journal of the Acoustical Society of America* 124.6 (2008), pp. 3576–3593.

Appendix A

Nyquist Plot for FRFs

In order to show the readers the accuracy of the Nyquist circle fits, in the Appendix A, the Nyquist plots are included for all corresponding FRFs in Chapter 4 and 5. In each figure below, there are three sub-figures. The bottom left sub-figure shows how the Nyquist circle fits, the top right sub-figure shows how the estimated FRF mobility fit with the real one, and the bottom right sub-figure shows how the phase angle fits.

Chapter 4 experiment results

0.5mm gap thickness:

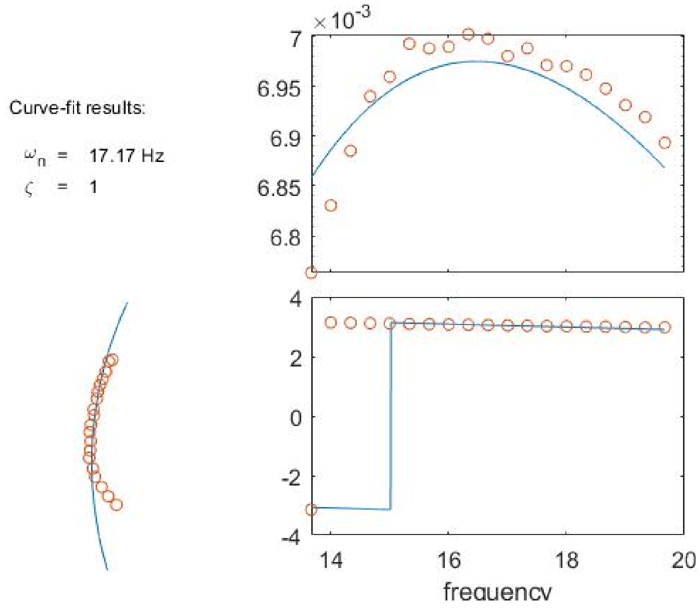

FIGURE A.1: 0.5mm thickness at normal pressure

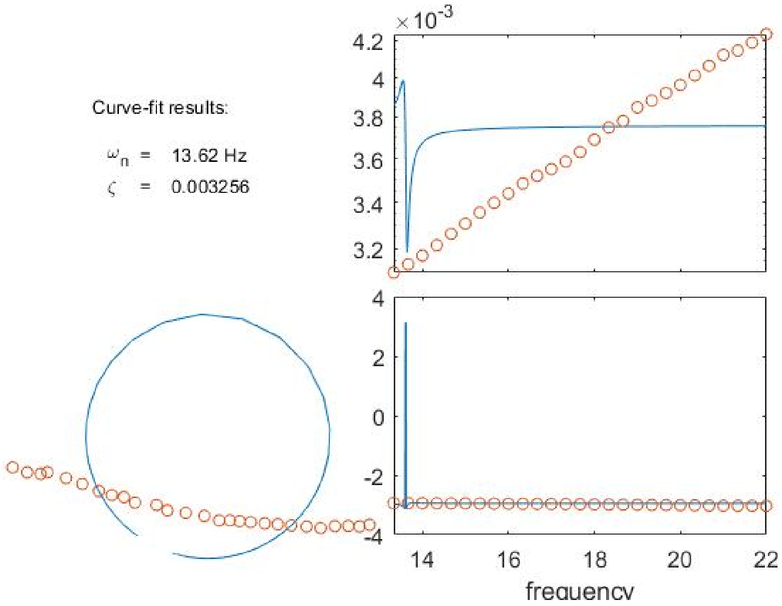

FIGURE A.2: 0.5mm thickness at -0.4 bar

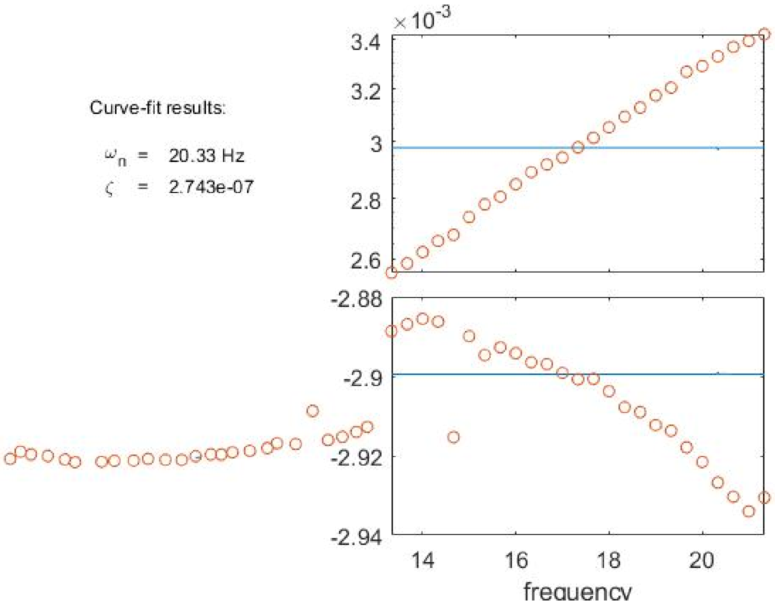

FIGURE A.3: 0.5mm thickness at -0.6 bar

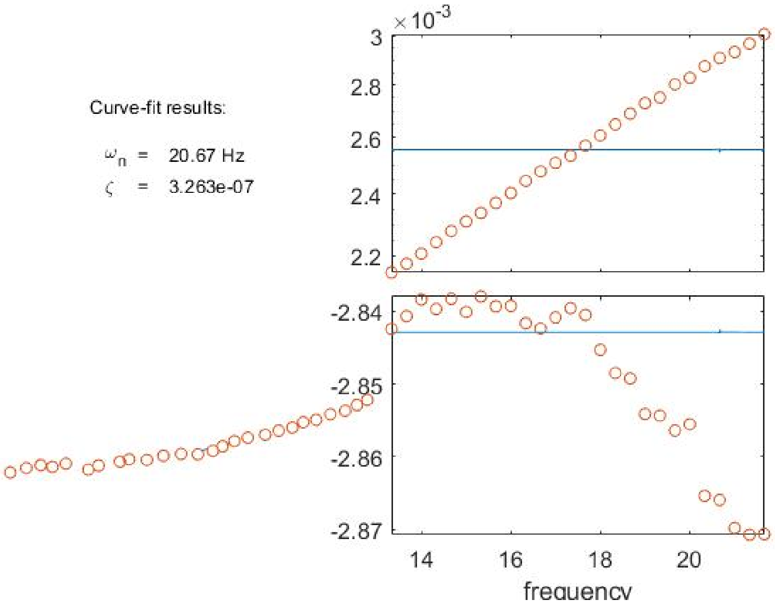

FIGURE A.4: 0.5mm thickness at -0.8 bar

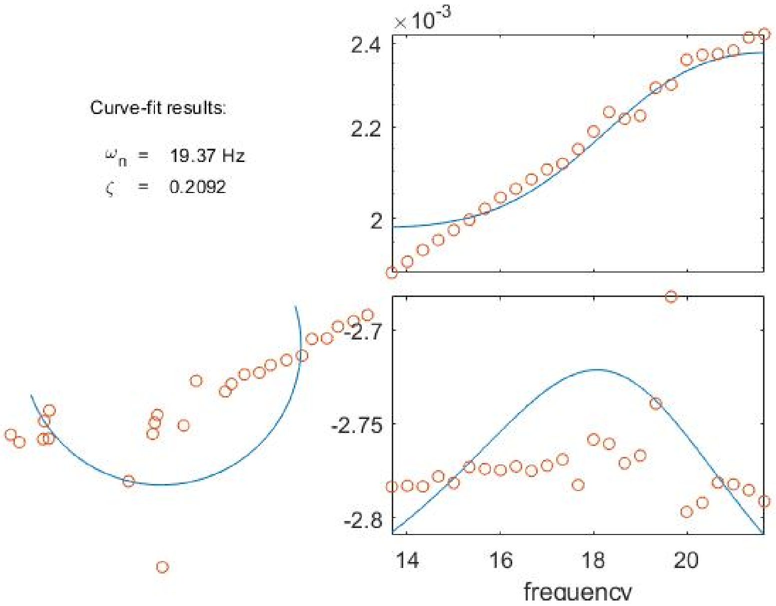

FIGURE A.5: 0.5mm thickness at vacuum pressure

1mm gap thickness:

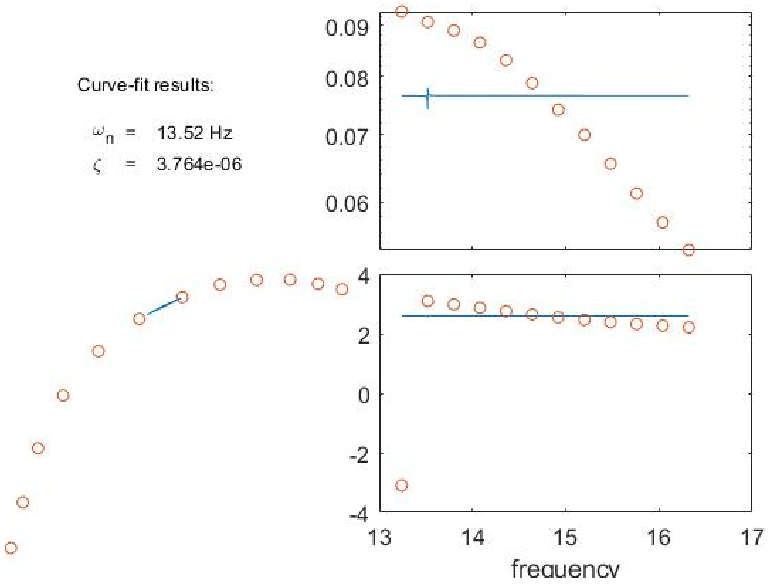

FIGURE A.6: 1mm thickness at normal pressure

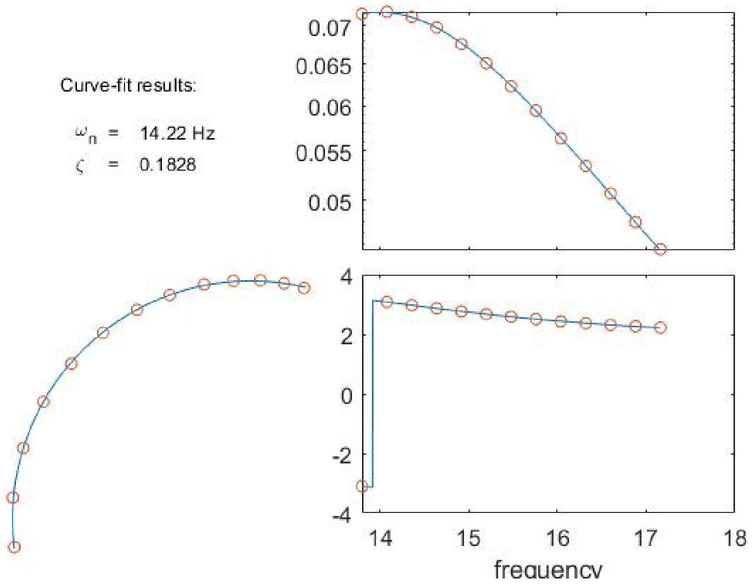

FIGURE A.7: 1mm thickness at -0.4 bar

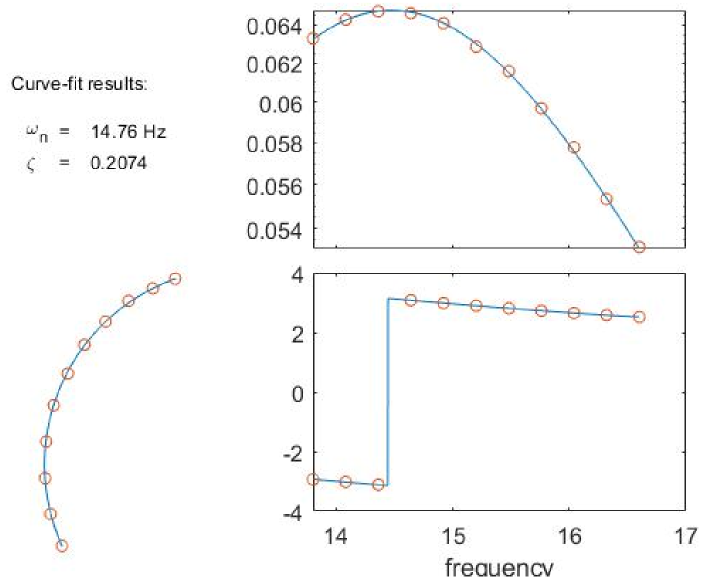

FIGURE A.8: 1mm thickness at -0.6 bar

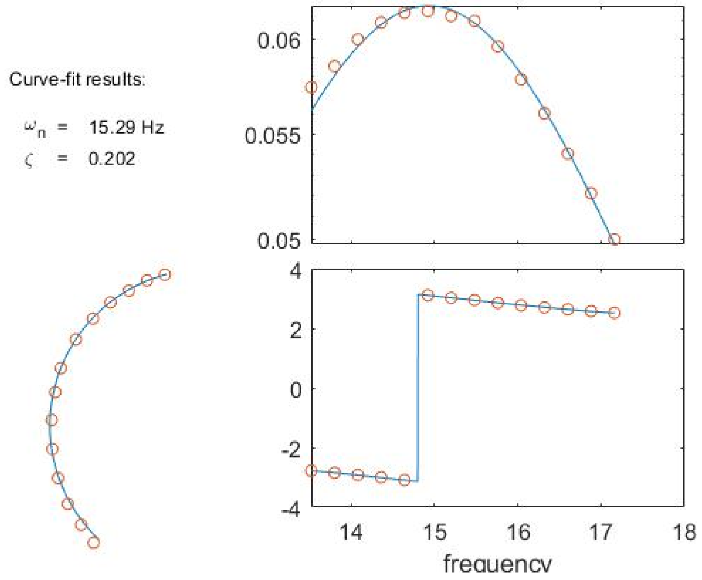

FIGURE A.9: 1mm thickness at -0.8 bar

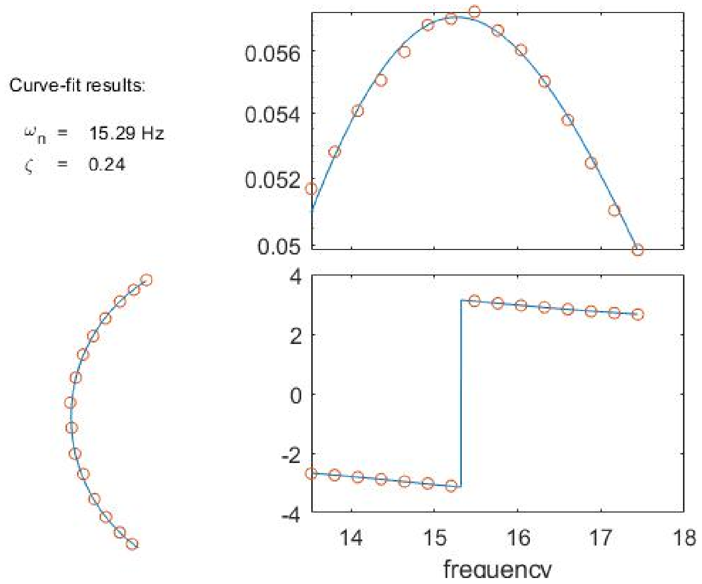

FIGURE A.10: 1mm thickness at vacuum pressure

2mm gap thickness:

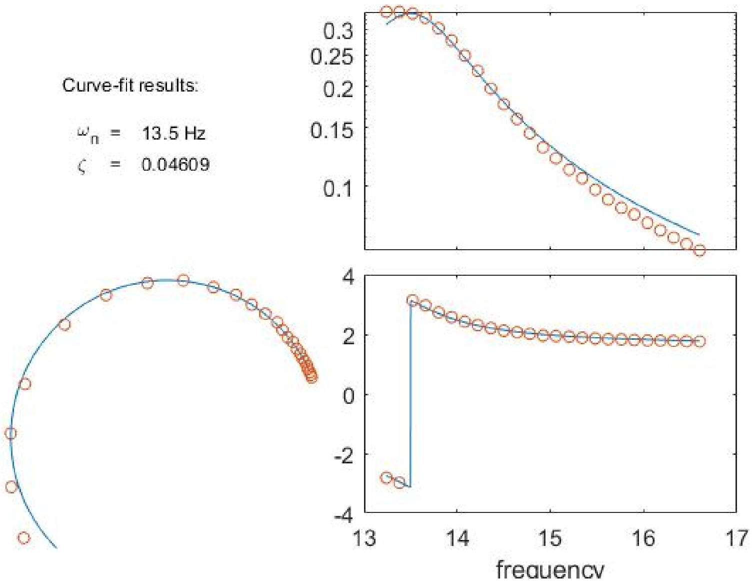

FIGURE A.11: 2mm thickness at normal pressure

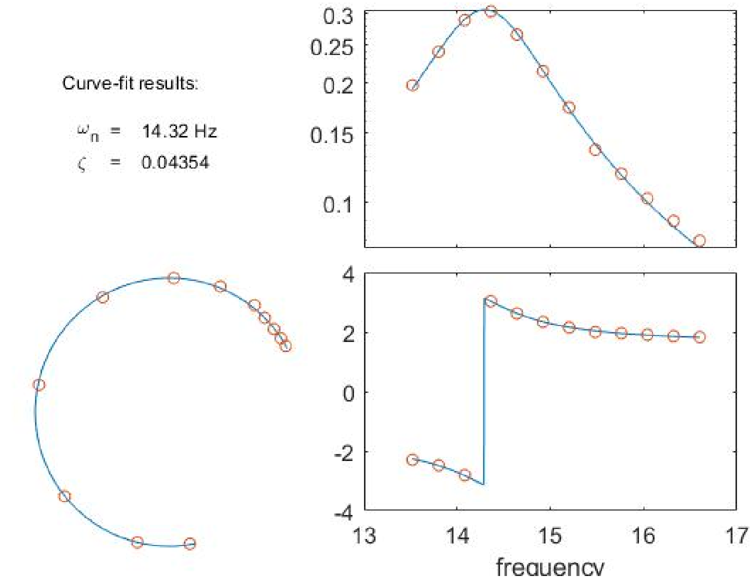

FIGURE A.12: 2mm thickness at -0.4 bar

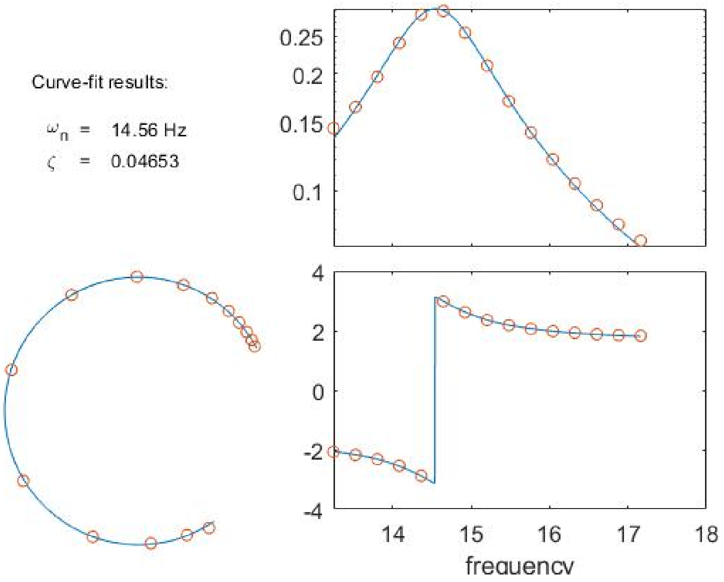

FIGURE A.13: 2mm thickness at -0.6 bar

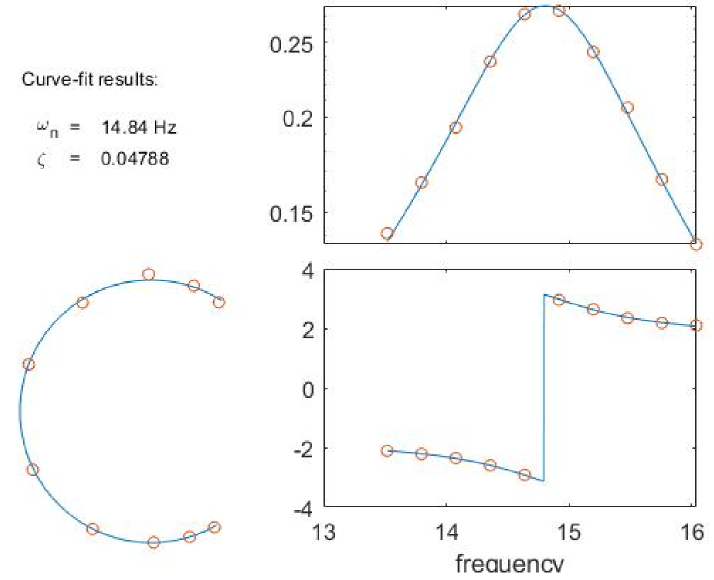

FIGURE A.14: 2mm thickness at -0.8 bar

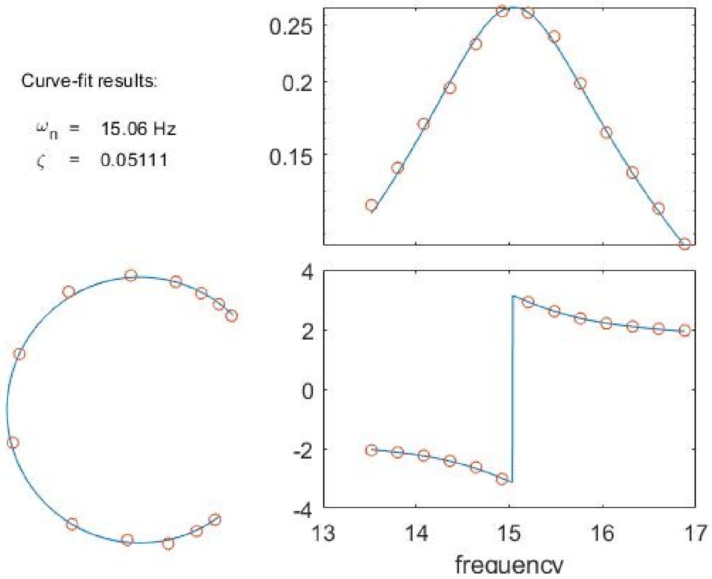

FIGURE A.15: 2mm thickness at vacuum pressure

8mm gap thickness:

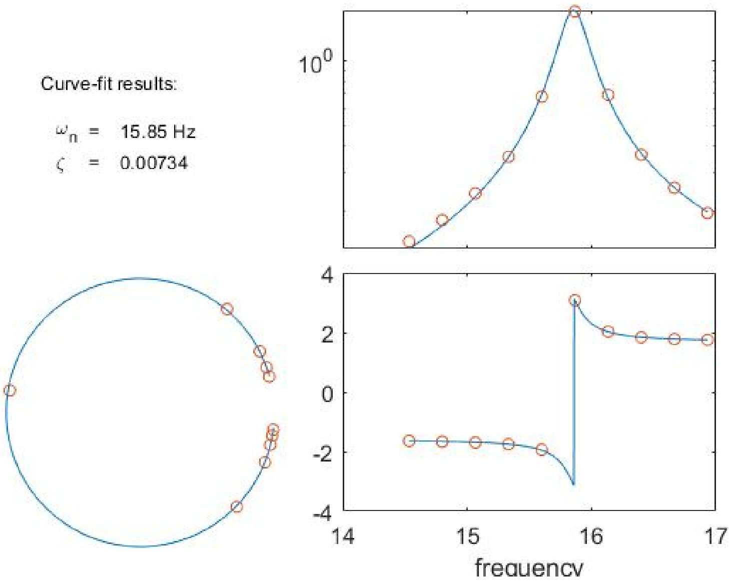

FIGURE A.16: 8mm thickness at normal pressure

10mm gap thickness:

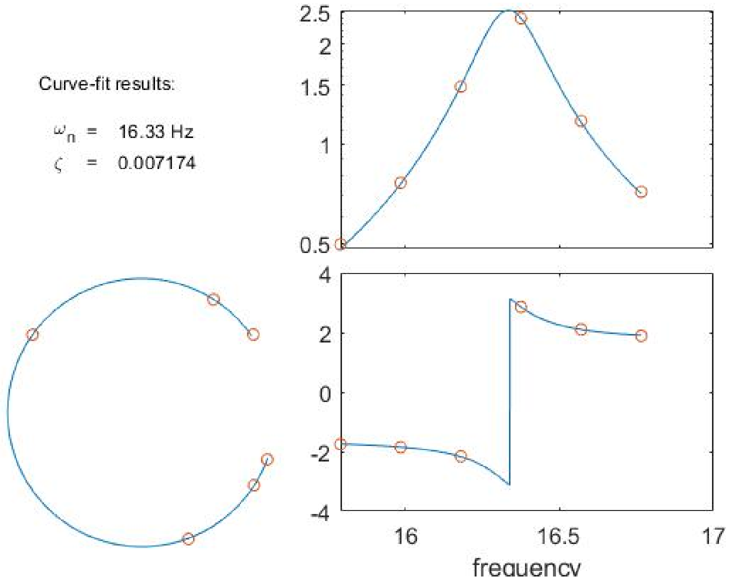

FIGURE A.17: 10mm thickness at normal pressure

Chapter 4 low reduced frequency model results

1mm gap thickness:

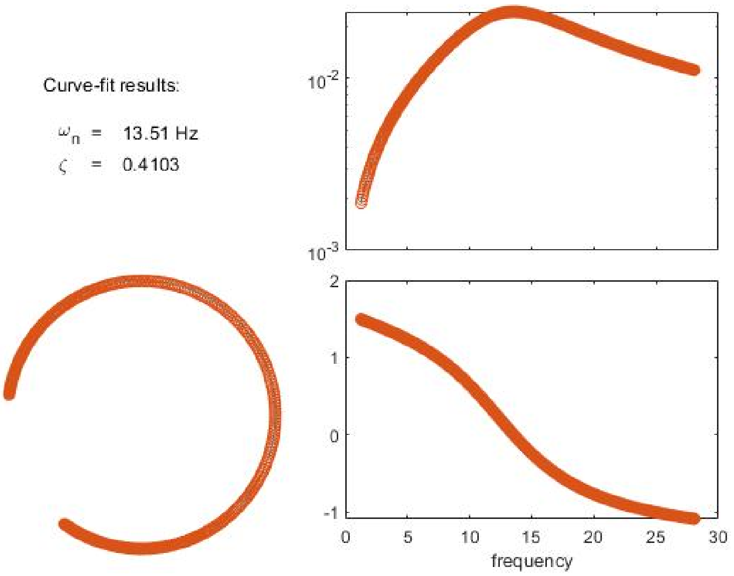

FIGURE A.18: 1mm thickness at normal pressure

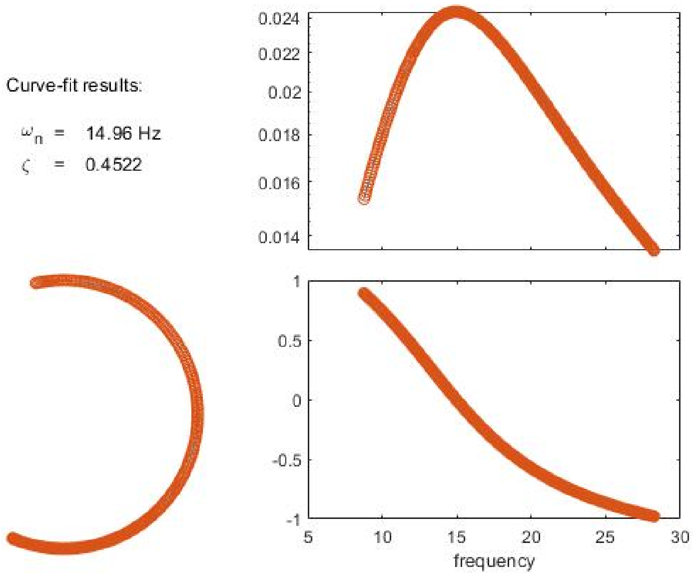

FIGURE A.19: 1mm thickness at -0.4 bar

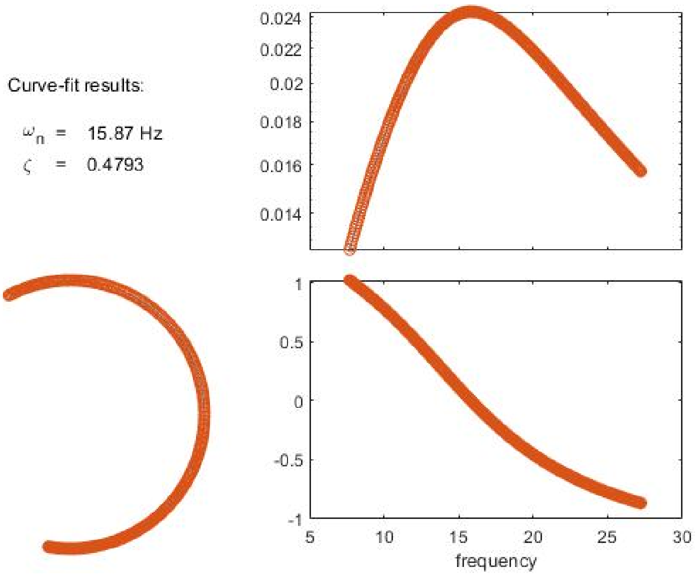

FIGURE A.20: 1mm thickness at -0.6 bar

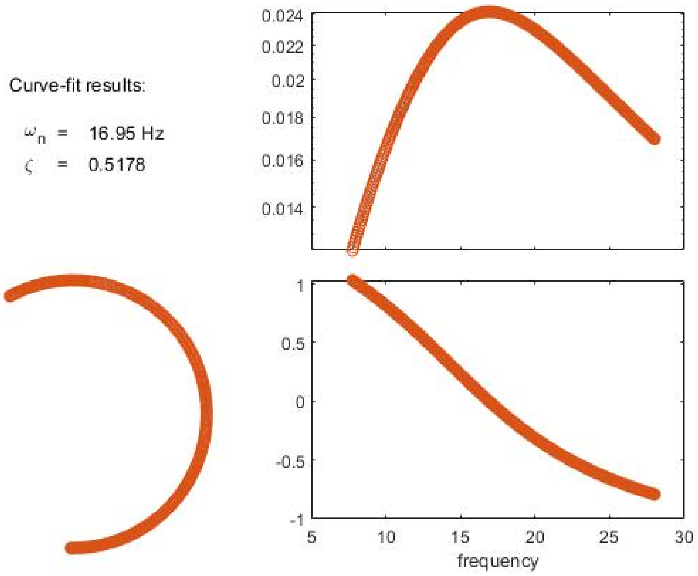

FIGURE A.21: 1mm thickness at -0.8 bar

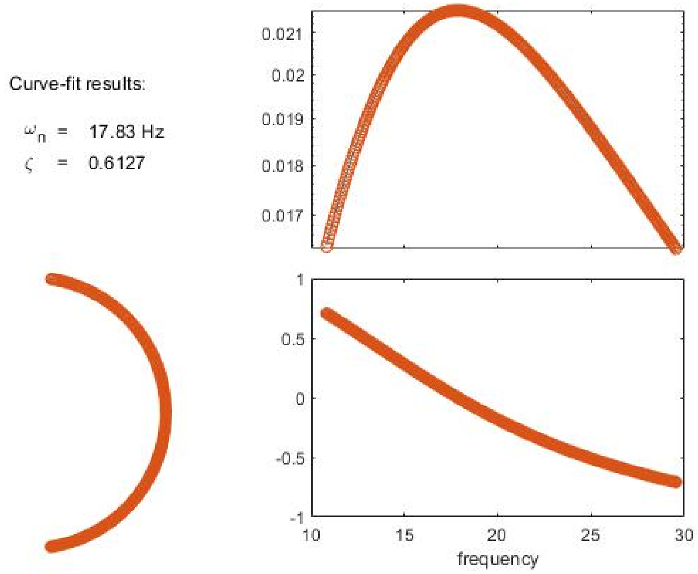

FIGURE A.22: 1mm thickness at vacuum pressure

2mm gap thickness:

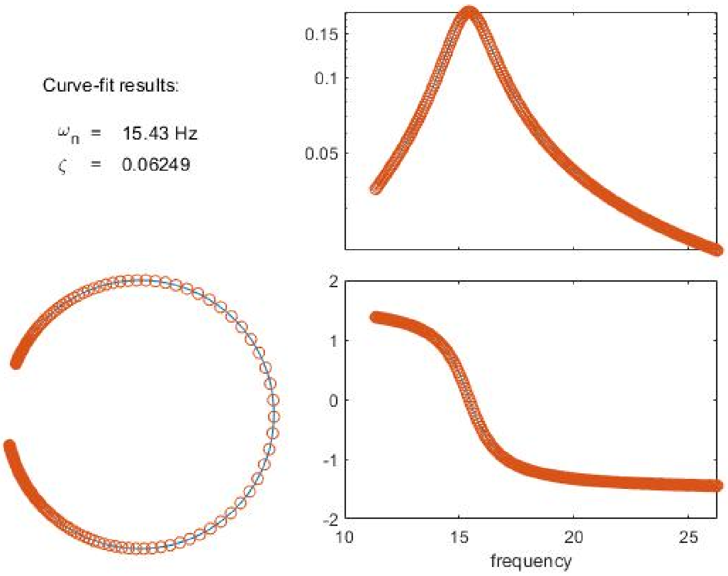

FIGURE A.23: 2mm thickness at normal pressure

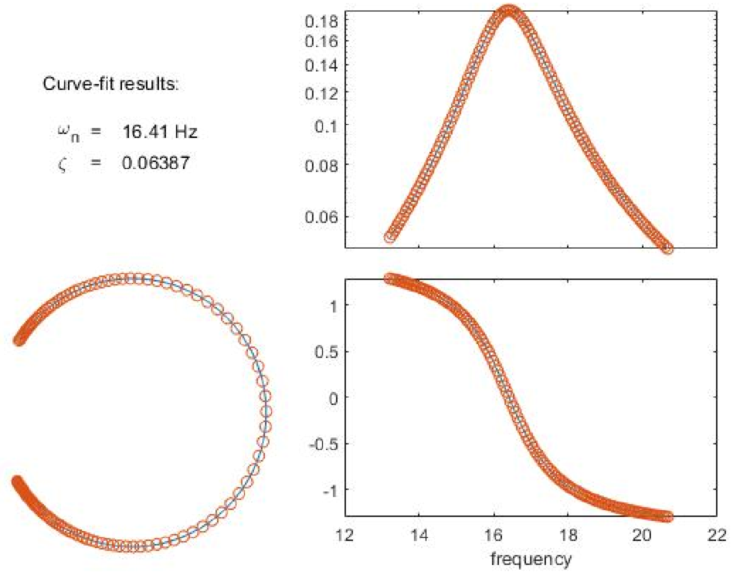

FIGURE A.24: 2mm thickness at -0.4 bar

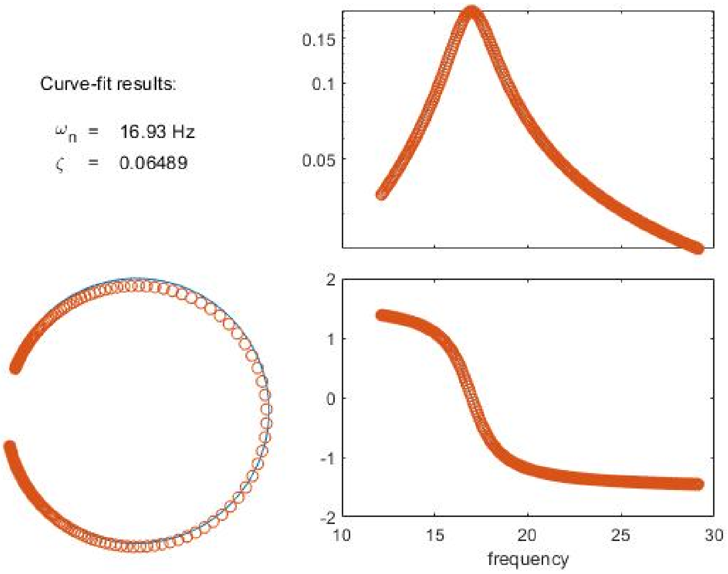

FIGURE A.25: 2mm thickness at -0.6 bar

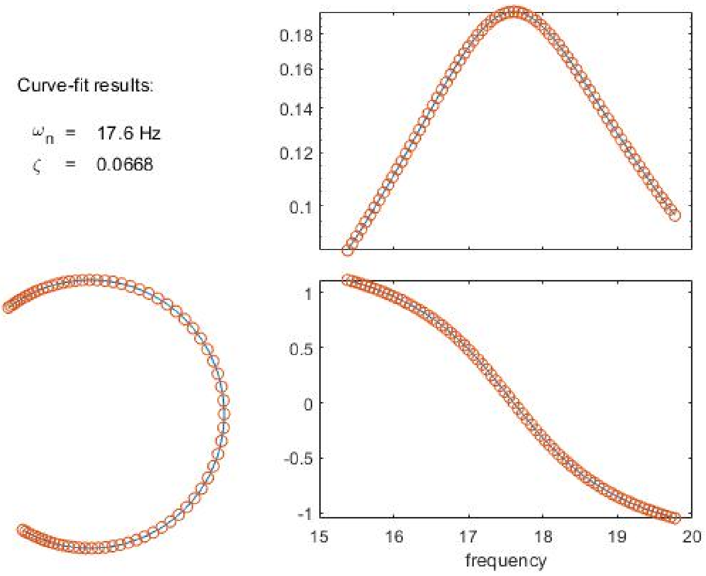

FIGURE A.26: 2mm thickness at -0.8 bar

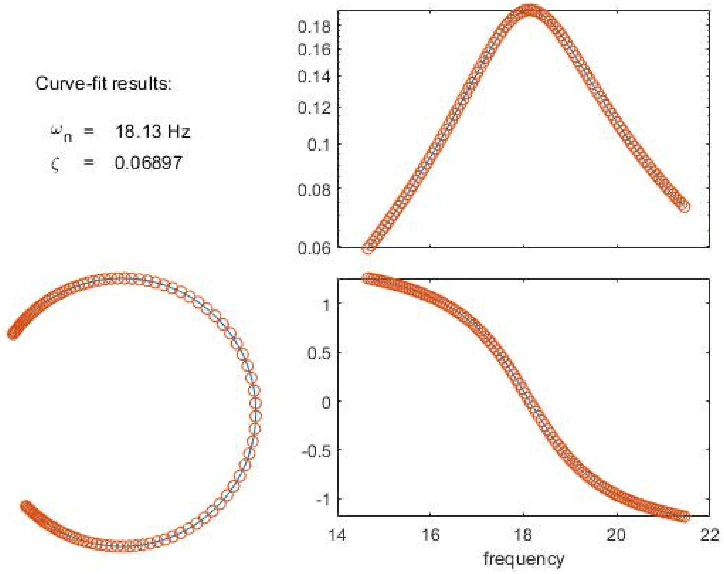

FIGURE A.27: 2mm thickness at vacuum pressure

Other gap thickness:

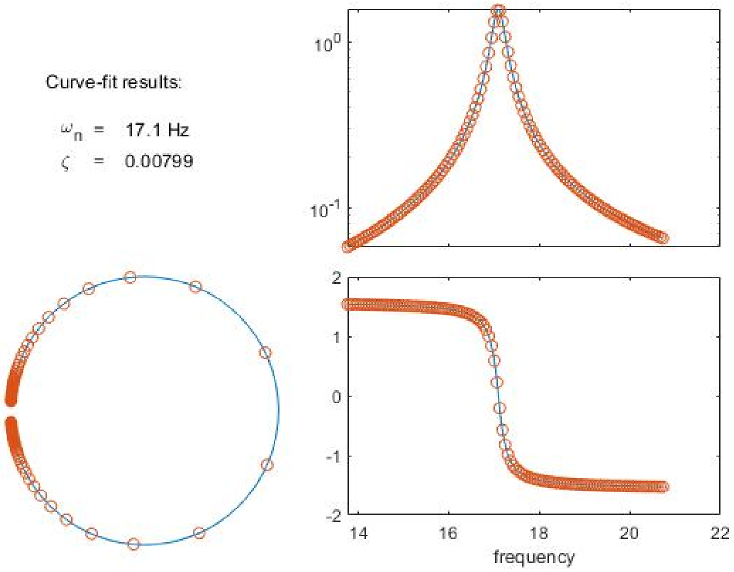

FIGURE A.28: 5mm thickness at normal pressure

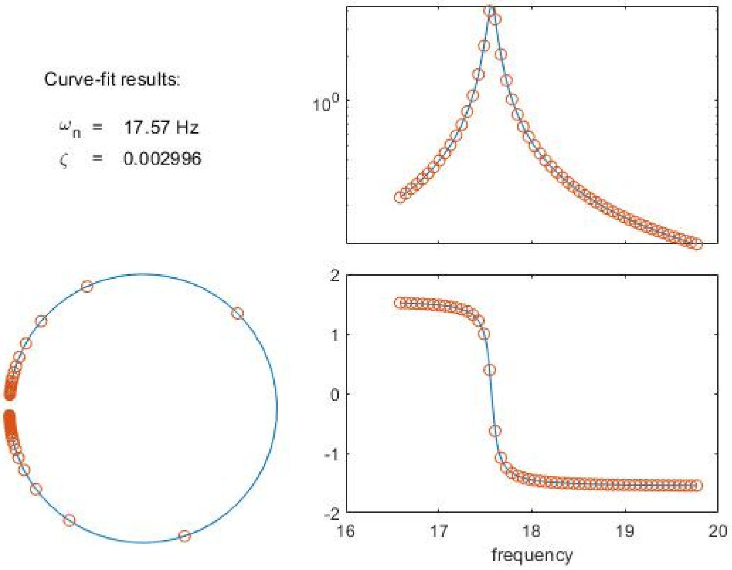

FIGURE A.29: 8mm thickness at normal pressure

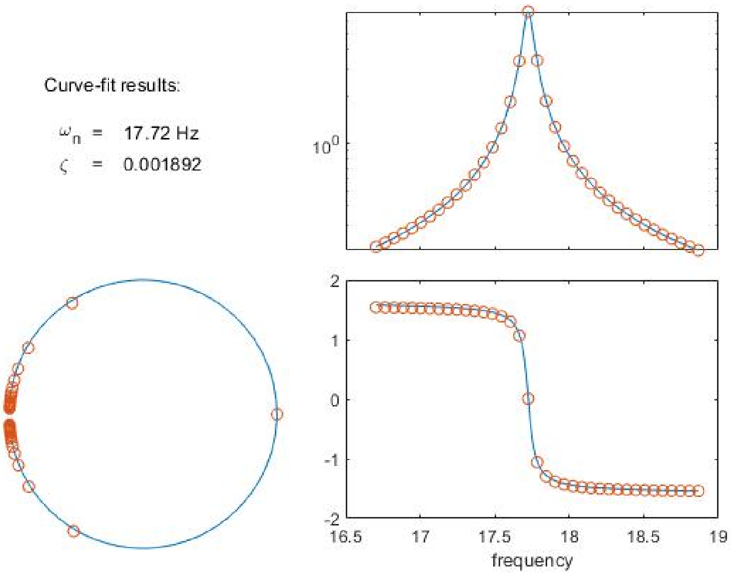

FIGURE A.30: 10mm thickness at normal pressure

Chapter 5 FE model

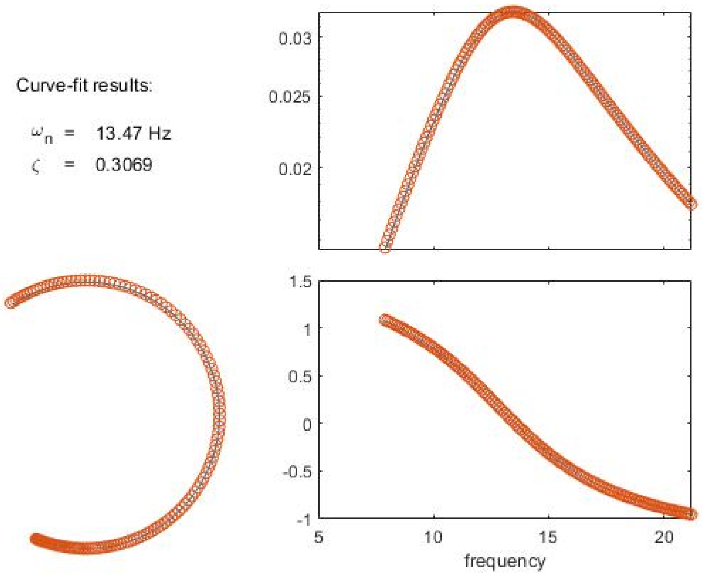

FIGURE A.31: 1mm thickness at normal pressure

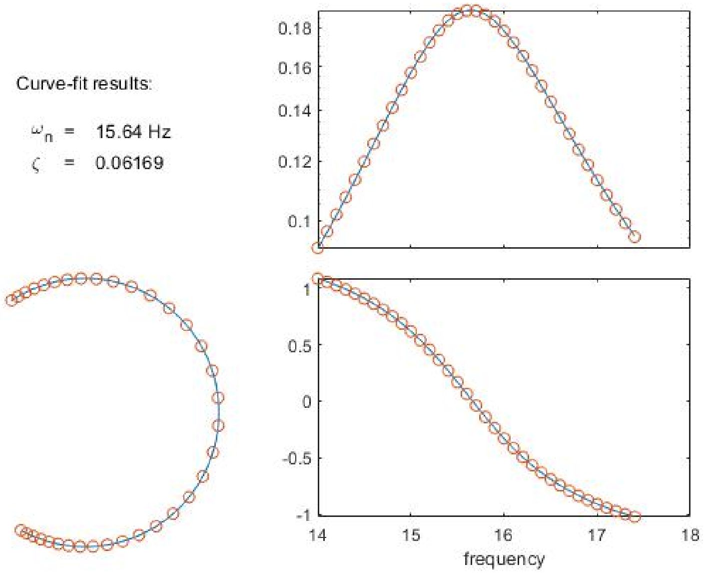

FIGURE A.32: 2mm thickness at normal pressure

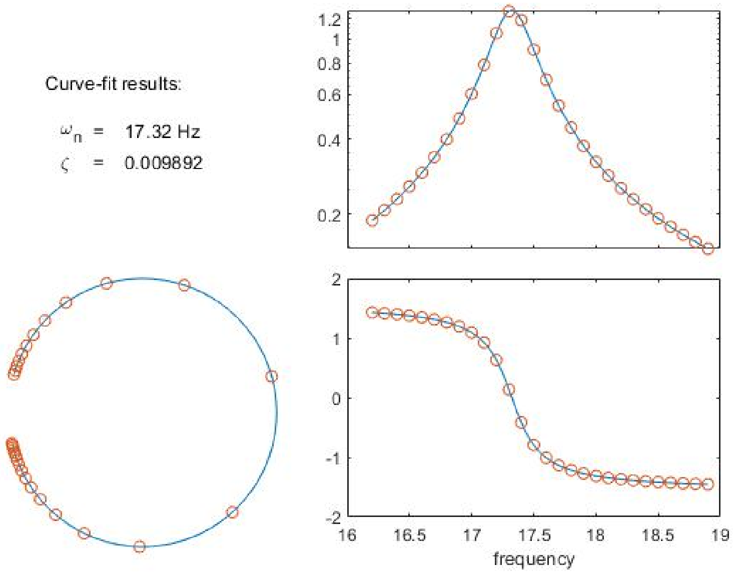

FIGURE A.33: 5mm thickness at normal pressure

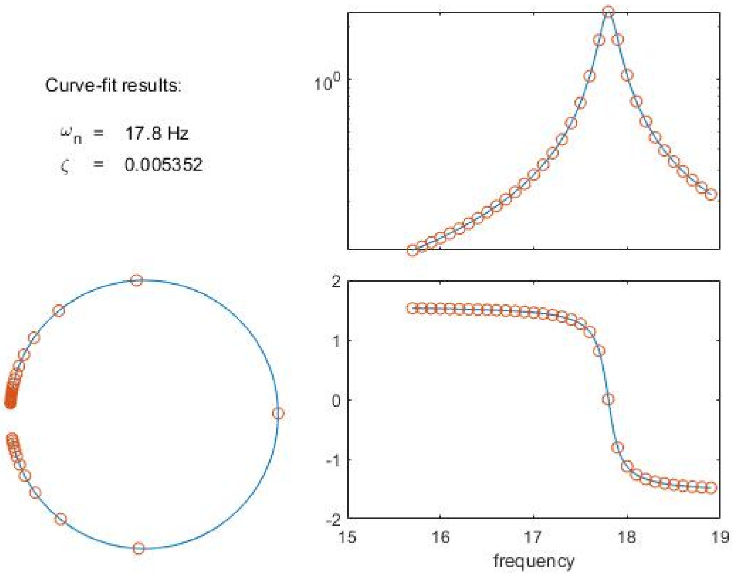

FIGURE A.34: 8mm thickness at normal pressure

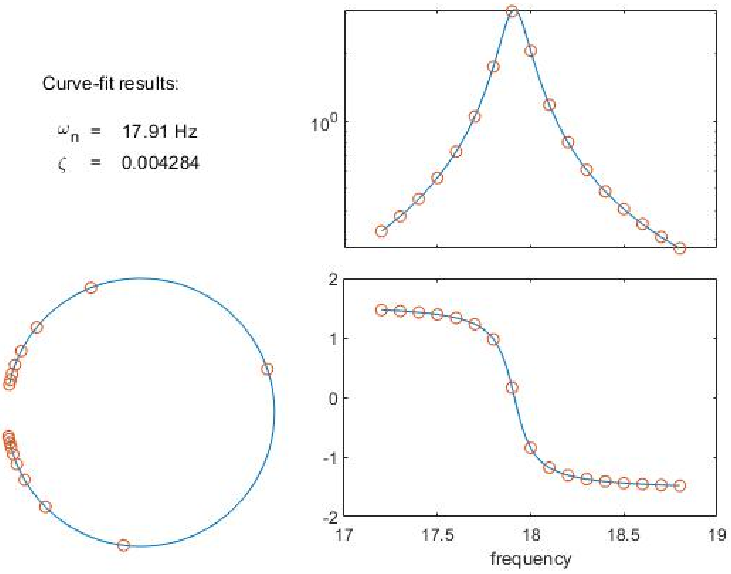

FIGURE A.35: 10mm thickness at normal pressure